Numerical Renormalization Group Study on Multiorbital Impurity Anderson Model

SHINYA NISHIYAMA

MARCH 2013

SHINYA NISHIYAMA Numerical Renormalization Group Study on Multiorbital Impurity Anderson Model MARCH

Numerical Renormalization Group Study on Multiorbital Impurity Anderson Model

A dissertation submitted to
THE GRADUATE SCHOOL OF ENGINEERING SCIENCE
OSAKA UNIVERSITY
in partial fulfillment of the requirements for the degree of
DOCTOR OF PHILOSOPHY IN SCIENCE

BY

SHINYA NISHIYAMA

MARCH 2013

Abstract

In recent decades, one of the essential issues in condensed matter physics has been the elucidation of the origins of anomalous behaviors observed in strongly correlated electron systems. In particular, some heavy fermion systems show anomalous properties such as an unconventional superconductivity, non-Fermi liquid behaviors in various physical quantities and so on. These anomalous properties are caused by competition between the Kondo effect and other effect such as the crystalline-electric-field effect, an inter-site magnetic correlation between f-electrons caused by the RKKY interaction. In this thesis, we investigate the properties given by some of these competition effects in impurity systems in order to give clues to understand the anomalous phenomena observed in lattice heavy fermion systems on the basis of the numerical renormalization group method.

In chapter 2, we discuss the enhanced Hall coefficient inside an antiferromagnetic phase where the Néel temperature $T_{\rm N}$ coincides with the Kondo temperature $T_{\rm K}$. $CeRu_2(Si_{1-x}Ge_x)$ at $x \simeq 0.1$ is one of the candidates which shows such a behavior. First, we investigate the charge transfer susceptibility between f- and conduction electrons in the two-impurity Anderson model on the basis of the numerical renormalization group method. When the conduction bands hold the particle-hole symmetry, the charge transfer susceptibility diverges logarithmically at the unstable fixed point due to the competition between the Kondo-Yosida singlet state and an inter-site spin-singlet state. Even without the particle-hole symmetry of conduction bands, the charge transfer susceptibility is also enhanced at the point where the ground state crosses over between these two singlet states. Second, we obtain the correction terms of the diagonal conductivity and the off-diagonal (Hall) conductivity due to the charge transfer susceptibility, and show that the Hall coefficient increases at the unstable fixed point in the two-impurity Anderson model. This result gives a possible scenario for understanding the enhancement in the Hall coefficient observed in $CeRu_2(Si_{1-x}Ge_x)$ at $x \simeq 0.1$ where $T_{\rm N}$ coincides with $T_{\rm K}$.

In chapter 3, we discuss the magnetic field effect on f^2-crystalline-electric-

field (CEF) singlet systems with tetragonal symmetry. If the hybridization between f-electrons and conduction electrons is changed, the system passes through the quantum critical point (QCP) caused by the competition between the f^2-CEF singlet state and the Kondo-Yosida singlet state in this system. Around this QCP, the characteristic temperature $T_{\rm F}^*$ at which the entropy starts to decrease toward zero is suppressed by the effect of the competition, compared to both energy scales characterizing each singlet state, the lower Kondo temperature ($T_{\rm K2}$) and the CEF splitting (Δ) between the ground state and the first excited state. We show that $T_{\rm F}^*$ is not affected by the magnetic field up to H_z^* which is determined by the distance from the QCP or characteristic energy scales of each singlet state, and is far larger than $T_{\rm F}^*$ and less than $\min(T_{\rm K2}, \Delta)$. As a result, in the vicinity of the QCP, there are parameter regions where the non-Fermi Liquid behavior is robust against the magnetic field, at an observable temperature range $T > T_{\rm F}^*$, up to H_z^*. This result suggests that such an anomalous non-Fermi liquid behavior can also arise in systems with other CEF symmetries, which might provide us with a basis to understand the anomalous behaviors of UBe_{13}.

In chapter 4, we reveal the magnetic field effect on the criticality due to the competition between the f^2-CEF singlet state and the Kondo-Yosida singlet state in the tetragonal symmetry. Around the QCP due to this competition, the magnetic field H breaks the unstable fixed point due to this competition by two mechanisms: one causing the magnetic polarization of f-electrons and the other giving the "channel" anisotropy. These two mechanisms make a difference in the magnetic field dependence of the characteristic temperature $T_{\rm F}^*(H)$, the crossover temperature from non-Fermi liquid behavior to Fermi-liquid behavior. While the magnetic polarization of f-electrons gives $T_{\rm F}^*(H) \propto H^x$ ($x \simeq 2.0$), the "channel" anisotropy gives the H-independent $T_{\rm F}^*(H)$ as discussed in chapter 3. These two mechanisms cross over continuously at around the crossover magnetic field $H_{\rm cr}$, where an anomalous H-dependence of $T_{\rm F}^*(H)$ appears. Such $T_{\rm F}^*(H)$ well reproduces the H-dependence of $T_{\rm F}^*$ observed in $Th_{1-x}U_xRu_2Si_2$ with $x \simeq 0.03$. We also find that the H-dependence of the resistivity and the magnetic susceptibility are in good agreement with the experimental results of this material.

In chapter 5, we investigate the fixed point of the f^2-configuration system with the Γ_1 singlet ground state and the Γ_4 first excited triplet state in the cubic symmetry. There are two possible ground states: the singlet ground state and the triplet ground state because the Γ_4 first excited triplet state is stabilized due to the hybridization. The feature of the singlet state crosses over between the CEF singlet and the K-Y singlet states smoothly, although

it has been shown in chapters 3 and 4 that, in the tetragonal symmetry of the crystal, these two singlet state compete and give rises to an unstable fixed point. In the present model with the cubic symmetry, the unstable fixed point is caused by the competition between the singlet fixed point and triplet fixed point, giving rises to non-Fermi liquid behaviors in various physical quantities such as resistivity, the Sommerfeld coefficient, and the magnetic susceptibility. Moreover, when the system comes near by the unstable fixed point from the K-Y singlet ground state region and goes into the CEF singlet ground state region, the experimental result that the lattice constant of UBe_{13} gives the maximum Sommerfeld coefficient among the series of a system of solid solution $U_{1-x}T_xBe_{13}$ can be reproduced. This result possibly provides us with a basis to understand the anomalous behaviors of UBe_{13}.

Contents

Chapter 1

Introduction

In recent decades, one of the essential issues in condensed matter physics has been to understand the origins of the quantum critical phenomena which occur in strongly correlated electron systems. When we consider the properties of most materials, an approach based on the Fermi liquid theory introduced by Landau [1, 2] often gives a good description. In the Fermi liquid theory, low energy states are described by quasiparticles which have an enhanced effective mass through the renormalization effect due to the interactions among electrons, called the many body effect.

However, there exist some materials in heavy fermion compounds and high-T_c cuprates which cannot be fully described by the Fermi liquid theory. These systems are called non-Fermi liquid systems and appear in several materials located near the quantum critical point (QCP) around which quantum fluctuations in the spin, the orbital and the valence are highly developed. Around the QCP, anomalous temperature dependence (non-Fermi liquid behavior) occurs in various physical quantities, the unconventional superconductivities induced by such quantum fluctuations .

In particular, heavy fermion systems are mine of these anomalous physical phenomena, such as the multiple superconducting phases in UPt_3, the "Hidden order" state in URu_2Si_2, and the valence fluctuation mediated superconductor observed in $CeCu_2(Si_{1-x}Ge_x)_2$, etc. These heavy fermion systems usually include f-electrons which have both itinerant and localized characters in contrast to essentially itinerant conduction electrons corresponding to s-, p-, and d- electrons. These f-electrons are considered to be the origin of the anomalous physical phenomena noted above. Considerable theoretical research has been carried out by including interactions among f-electrons and hybridization between the f-electron and conduction electrons in order to un-

derstand these anomalous physical phenomena around the QCP. Moreover, through investigations of heavy fermion systems, new concepts in solids and new theoretical approaches have been created, often offering important concepts to discuss other strongly correlated electron systems. Thus, clarifying origins of the QCP in heavy fermion systems is one of the most fascinating issues in strongly correlated electron systems.

1.1 Kondo Effect

One of the most fundamental origins of the anomalous phenomena in heavy fermion systems is the Kondo effect, which is caused by an interplay of strong correlations among f-electrons and the hybridization between conduction electrons and f-electrons giving rise to the exchange interaction among them. In high temperature regions, the f-electron behaves as almost like a localized magnetic moment, causing a resonant scattering of conduction electrons, i.e., the Kondo effect. As temperature decreases, the exchange interaction between the f-electron and conduction electrons grows logarithmically. Below a certain temperature, the f-electron starts to make a resonant state with the conduction electrons, i.e., the Kondo-Yosida singlet state. This Kondo effect is a key concept in the discussion of properties of heavy fermion systems. The temperature at which a crossover between the high temperature region and the low temperature region occurs is called the Kondo temperature (T_{K}). At $T \ll T_{\mathrm{K}}$, the system can be described by the local Fermi liquid theory, i.e., the low energy excitations of the systems are described by the "quasiparticles", which are complexes of the localized f-electron and conduction electrons.

The Kondo effect originated at the resistance minimum phenomenon observed in dilute magnetic alloy in 1930s. In 1964, J. Kondo studied the s-d model in which the conduction electrons are subject to the exchange interaction with the localized magnetic moment, and proved by means of the second order Born approximation that the resistivity shows logarithmic divergence as temperature decreases [3]. Owing to the first theoretical work by J. Kondo, it is clarified that the origin of the resistance minimum phenomenon is the antiferromagnetic exchange interaction between the localized magnetic moment and conduction electrons, although there remained the problem that the resistivity diverges at zero temperature. (Recently, the s-d model is sometimes called the Kondo model.)

In order to answer this question, H. Suhl discussed this issue on the basis of scattering theory and obtained the result for the temperature dependence

of the resistivity in the whole temperature region: i.e., $\rho(T) \propto -\log T$ in the high temperature region and $\rho(T = 0)$ =constant of the unitarity limit [4]. The same result was obtained simultaneously by Y. Nagaoka by the decoupled equations of motion for double-time Green's functions, and introduce the characteristic temperature "T_c" that was called the Kondo temperature T_K later [5]. However, these two theories turned out not to describe behaviors correctly in the low temperature region at $0 < T < T_K$.

On the other hand, A. A. Abrikosov focused on the contributions from higher order perturbative corrections. He summed the most dominant term (the most divergent term) from each order perturbation expansion, and obtained the result that the resistivity diverges at T_K [6]. In the same way, the magnetic susceptibility was also shown to exhibit negative divergence at $T < T_K$. Thus, the perturbation theory cannot correctly describe the low temperature region $T < T_K$ in the Kondo model.

It was K. Yosida who gave a clue to understanding what happens in a low temperature region, $T < T_K$. He discussed the nature of the ground state in the Kondo model and concluded that the ground state is the spin singlet state composed of the localized moment screened by the induced spin polarization due to the change of spin density of state of conduction electrons, i.e., the Kondo-Yosida singlet state [7]. After the work by K. Yosida, the way in which the ground state property in interpolated to that in a high temperature region $T > T_K$ was discussed.

P. W. Anderson and his coworkers introduced the idea of scaling for this question [8, 9, 10, 11, 12]. They eliminated intermediate states near the band edge of conduction electrons appearing in the perturbation expansion for the T-matrix, and derived the change of coupling constants between the localized moment and conduction electrons due to this step by setp elimination. This is a fundamental idea of the method of the scaling theory, or the renormalization ground approach. With this scaling procedure, the original model is renormalized into an effective model through the renormalization of the coupling constants, and these coupling constants increase infinitely as the band width of conduction electrons is reduced, if the initial coupling constants locate in the "antiferromagnetic region". Although coupling constants show unphysical divergence at the renormalized band width $E_c = k_B T_K$ in the scaling procedure, this result indicates that the system goes to the strong coupling limit in the low energy limit, suggesting that the ground state is the spin singlet state due to the strong antiferromagnetic coupling between the localized moment and conduction electrons. This is consistent with the result obtained by K. Yosida. With this result, they succeeded in discussing the effect of the reduction of the

band width of conduction electrons in the Kondo model, which gives a clue to describe the Kondo model from high temperature region $T > T_{\mathrm{K}}$ to low temperature region $T < T_{\mathrm{K}}$.

The first calculation of the physical quantities that are valid at all temperatures in the Kondo model was carried out by K. G. Wilson. He created a powerful tool, the numerical renormalization group (NRG) method [13] by taking the renormalization group idea from the field theory in quantum electrodynamics and the idea of scaling from critical phenomena associated with the phase transition of the second order. The idea of scaling corresponds to deriving the effective Hamiltonian in a low energy region by the combination of the coarse graining of the degrees of freedom and the scale transformation. One of the most famous problems discussed by this method is the block spin renormalization group discussed by L. P. Kadanoff [14]. However, as it is non-perturbative about all parameters, the NRG method is different from most renormalization group methods. With this method, K. G. Wilson investigated the Kondo model and obtained thermodynamic quantities such as the susceptibility, the Sommerfeld coefficient, and the specific heat continuously from the high temperature region to the low temperature region. Moreover, it was shown that the low-energy excitations of the Kondo model in a low temperature region, $T < T_{\mathrm{K}}$, is represented by the effective Hamiltonian which has only two parameters and does not include the spin operator corresponding to the localized moment. This fact indicates that the localized moment is screened out by conduction electrons, i.e., the singlet state is constructed in the ground state. P. Nozière focused on this result and considered that the low energy states in the Kondo model could be described by the phase shift of conduction electrons on the basis of the local Fermi liquid theory [15]. In this way, he reproduced the relations obtained by Wilson and derived the temperature dependence of the resistivity at low temperature $T \ll T_{\mathrm{K}}$ [13].

Thus, the Kondo effect had been investigated on the basis of the *s-d* model at first. However, the *s-d* model can be derived from the Anderson model by treating the hybridization between the localized electron and conduction electrons with the second order perturbation theory. On the basis of the Fermi liquid theory, the ground state and the low energy spectrum in non-interacting systems adiabatically connect with that in interacting systems if there is no phase transition between the Anderson model with $U = 0$ and that with finite U. There should be no phase transition in the "impurity" Anderson model. Thus, owing to this adiabatic continuity, when we take U into account perturbatively, the character of the ground state of the Anderson model should be the same as that in the case of $U = 0$, i.e., the nonmagnetic state in which

the number of localized electrons with up spin is the same as that of localized electrons with down spin. From this viewpoint, K. Yamada and K. Yosida carried out the perturbative expansion of U for the Anderson model to the infinite order, and proved that the specific heat, the susceptibility and the resistivity are expressed as a function of two parameters [16, 17, 18, 19], which is consistent with the result by K. G. Wilson and P. Nozière in the limit $U \to \infty$.

Thus, owing to a lot of theoretical work, the Kondo effect proved to be the phenomenon in which the localized electron behaving as the magnetic moment in the high temperature region ($T > T_{\rm K}$) starts to be screened by the conduction electrons at $T \lesssim T_{\rm K}$, and crosses over to the non-magnetic ground state described by the local Fermi liquid system by forming the resonant state with conduction electrons in the low temperature region ($T < T_{\rm K}$). After the work by K. Yamada and K. Yosida, the exact solution of the Kondo model was obtained by N. Andrei [20, 21, 22] and P. B. Wiegmann [23, 24], and that of the Anderson model was obtained by N. Kawakami and A. Okiji [25, 26], and P. B. Wiegmann [27]. These results verified the physical picture of the Kondo effect attained up to that time.

1.2 Discussion of Heavy Fermion Systems by Numerical Renormalization Group Method

As noted above, the NRG method was developed by K. G. Wilson for the purpose of describing the Kondo model from high to low temperature regions [13]. Since this first application, the NRG method has been extended to a much wider range of the quantum impurity problems, such as the Anderson model which extends the Kondo model so as to include the charge degrees of the freedom of the localized state at the impurity site [28, 29], the two channel Kondo model in which the impurity spin couples to two conduction bands [30], and so on.

For quantum impurity problems, the NRG method is one of the most powerful method available because it allows us to calculate the temperature dependence of the thermodynamic quantities at a wide temperature range, in particular at low temperature with good accuracy. As noted in the previous section, one of the fundamental origins of the anomalous behaviors observed in heavy fermion systems is the Kondo effect. Therefore, in order to describe the properties of heavy fermion systems, we should examine a wide temperature range, at least from the high temperature region ($T > T_{\rm K}$) to the low

temperature region ($T < T_{\mathrm{K}}$). If there is competition such as the one between the Kondo effect and the RKKY interaction, the characteristic energy scale of the system can become smaller than T_{K}. Of course, it is difficult to investigate the properties of heavy fermion systems, i.e., the lattice problem, from the beginning. Therefore, as a first step, we discuss the properties in heavy fermion systems in the range of the impurity model which has one or two f-electrons hybridizing with the conduction electrons. In such a situation, the NRG method works most effectively in discussing the physical behaviors as it can describe a wide temperature range continuously, in particular at low temperature $T \ll T_{\mathrm{K}}$. Moreover, we can definitely determine the ground state of the system and establish an effective model for the low energy spectrum of the impurity system by the NRG method. Thus, the NRG method is one of the most suitable methods for the discussion of the impurity system, which often gives helpful remarks to elucidate the properties in heavy fermion systems. In terms of such a viewpoint, the NRG method is extended as follows.

The two-impurity Anderson model, in which two localized electrons interact with each other and each localized electron hybridizes with conduction electrons, is the first example to discuss the competition effects between the Kondo effect and the other correlation effects on the basis of the NRG method. If the interaction between localized electrons is antiferromagnetic, there exist two stable fixed points in this model [30, 31, 32, 33, 34]. One is the Kondo-Yosida singlet fixed point where two localized electrons are screened out independently and form the Kondo-Yosida singlet states. The other is an inter-site spin singlet fixed point where the singlet state of two localized electrons is formed and the correlation between conduction electrons and localized electrons is lost. At the boundary of these two stable fixed points, there exists an unstable fixed point where the non-Fermi liquid behavior arises in various physical quantities such as the $\log T$-dependence in the Sommerfeld coefficient, the spin susceptibility, and so on.

This model simulates some anomalous aspects of Ce-based heavy fermion compounds in which trivalent Ce-ion with $4f^1$-configuration has the Kramers doublet ground state of a crystalline-electric-field (CEF) effect in the low temperature region, and the f-electrons at adjacent sites interact with each other through the RKKY interaction. The RKKY interaction stabilizes the antiferromagnetic long-range order, while the Kondo effect causes the screening of the magnetic moment due to the f-electron and suppresses the magnetic long-range orders. Because of these two conflicting effects, some Ce-based compounds exhibits various anomalous phenomena. The investigation of the two-impurity Anderson model on the basis of the NRG method gives a reason-

able explanation for these anomalous properties observed in Ce-based heavy fermion compounds.

The NRG method is also applied to the two-orbital impurity Anderson model that describes the properties of heavy fermion systems with f^2-configuration. This model has two orbitals interacting with each other at the impurity site and each orbital hybridizes with conduction electrons which have the same symmetry as the localized orbital: i.e., this model has the orbital degrees of the freedom at the impurity site and two conduction bands. With this model, we could discuss not only the Kondo effect of each localized electron but also the effects of the inter-orbital interactions such as the Hund's rule coupling and the CEF effect. In the tetragonal symmetry, we can reproduce the energy level scheme of the f^2-CEF effect by introducing the antiferromagnetic Hund's rule coupling [29]. As shown explicitly in the case of the tetragonal symmetry, this model also has two stable fixed points: one is the Kondo-Yosida singlet fixed point, and the other is an inter-orbital spin singlet fixed point where two localized electrons form the singlet state due to the CEF effect. The non-Fermi liquid behaviors arise at the boundary of these two stable fixed points, and the competition between these two singlet states gives rise to a variety of anomalous properties in various physical quantities.

This model offers us the first step to consider the f^2-configuration based heavy fermion systems which correspond to the U-based compounds with a tetravalent U-ion state or the Pr-based compounds with a trivalent Pr-ion state. Most of these materials have the singlet ground state due to the CEF effect. In particular, U-based compounds often have f-electrons with a relatively well extended wave-function strongly hybridizing with conduction electrons. In other words, it is expected that the U-based compounds exhibit the QCP due to the competition between these two singlet states. Actually, $R_{1-x}U_xRu_2Si_2$ (R=Th, Y, and La, x$\leq$ 0.07) is one of the candidates which shows the QCP due to the competition between the Kondo-Yosida singlet and the f^2-CEF singlet states [35, 36].

As noted above, the NRG method expands its field from the standard Kondo effect to the competition between Kondo effect and other correlation effect. In particular, such competitions are often observed in heavy fermion systems at low temperature. The NRG method works most effectively in discussing the low temperature physics, and is one of the most suitable methods for the discussion of the properties in heavy fermion systems.

1.3 Purpose of the Thesis

The purpose of this thesis is to elucidate the properties of the impurity systems which show competition effects between the Kondo effect and other correlation effects in order to give a clue to understanding the anomalous phenomena observed in heavy fermion systems. For this purpose, we investigate three types of extended Anderson models on the basis of the Wilson NRG method. Organization of this thesis is as follows.

First, in chapter 2, we investigate the charge transfer susceptibility χ_{fc} between the f-electron and conduction electrons in the two-impurity Anderson model. Although it has been already shown that the f-site charge (valence) susceptibility χ_v is enhanced at the unstable fixed point due to the competition between the Kondo-Yosida singlet and the inter-site spin-singlet states, we show that χ_{fc} is larger than χ_v by about 10^2 times and diverges logarithmically at the same point if the conduction bands hold the particle-hole symmetry. Such an enhanced χ_{fc} contributes to the Hall conductivity, giving a possible scenario for an enhancement in the Hall coefficient observed in $CeRu_2(Si_{1-x}Ge_x)$ at $x \simeq 0.1$, which is located inside an antiferromagnetic state where T_N coincides with T_K.

Second, in chapter 3, we investigate the two-orbital Anderson model with an antiferromagnetic Hund's rule coupling which reproduces the f^2-CEF effect in tetragonal symmetry. In this model, there exists the QCP due to the competition between the CEF singlet state and the Kondo-Yosida singlet state. Around this QCP, the characteristic temperature T_F^* at which the entropy starts to decrease toward zero is suppressed by the effect of the competition, compared to both energy scales characterizing each singlet state, the lower Kondo temperature (T_{K2}), and the CEF splitting (Δ) between the ground state and the first excited state. We show that in the case of tetragonal symmetry, T_F^* is not affected by the magnetic field up to H_z^*, which is determined by the distance from the QCP or characteristic energy scales of each singlet state, and is far larger than T_F^* and less than $\min(T_{K2}, \Delta)$. As a result, in the vicinity of QCP, there are parameter regions where the non-Fermi liquid is robust against the magnetic field, at an observable temperature range $T > T_F^*$, up to H_z^*. Our result suggests that such an anomalous non-Fermi liquid behavior can also arise in systems with other CEF symmetries, which might provide us with a basis to understand the anomalous behaviors of UBe_{13}.

Third, in chapter 4, we study the competition between the Kondo effect and the f^2-CEF effect in tetragonal symmetry, and show that the magnetic field breaks the unstable fixed point due to this competition by two mech-

anisms: one causing the magnetic polarization of f-electrons and the other giving the "channel" anisotropy. These two mechanisms make a difference in the magnetic field (H) dependence of the characteristic temperature $T_{\rm F}^*(H)$, the crossover temperature from the non-Fermi liquid to Fermi-liquid behavior. While the magnetic polarization of f-electrons gives $T_{\rm F}^*(H) \propto H^x$ ($x \simeq 2.0$), the "channel" anisotropy gives the H-independent $T_{\rm F}^*(H)$. These two mechanisms cross over continuously at around the crossover magnetic field $H_{\rm cr}$, where an anomalous H-dependence of $T_{\rm F}^*(H)$ appears. Such $T_{\rm F}^*(H)$ well reproduces the H-dependence of $T_{\rm F}^*$ observed in $Th_{1-x}U_xRu_2Si_2$. We also find that the H-dependence of the resistivity and the magnetic susceptibility are in good agreement with the experimental results of this material. These results suggest that the non-Fermi liquid behaviors observed in $Th_{1-x}U_xRu_2Si_2$ can be understood if this material is located in the f^2-CEF singlet region near the critical phase boundary between the two singlet states.

Finally, in chapter 5, we investigate the fixed point of the f^2-configuration system with the Γ_1 singlet ground state and the Γ_4 first excited triplet state in the cubic symmetry. There are two possible ground states: the singlet ground state and the triplet ground state because the Γ_4 first excited triplet state is stabilized due to the hybridization. The feature of the singlet state crosses over between the CEF singlet and the K-Y singlet states smoothly, although it has been shown in chapters 3 and 4 that, in the tetragonal symmetry of the crystal, these two singlet state compete and give rises to an unstable fixed point. In the present model with the cubic symmetry, the unstable fixed point is caused by the competition between the singlet fixed point and triplet fixed point, giving rises to non-Fermi liquid behaviors in various physical quantities such as resistivity, the Sommerfeld coefficient, and the magnetic susceptibility. Moreover, when the system comes near by the unstable fixed point from the K-Y singlet ground state region and goes into the CEF singlet ground state region, the experimental result that the lattice constant of UBe_{13} gives the maximum Sommerfeld coefficient among the series of a system of solid solution $U_{1-x}T_xBe_{13}$ can be reproduced. This result possibly provides us with a basis to understand the anomalous behaviors of UBe_{13}.

Bibliography of Chapter 1

[1] L. D. Landau: Sov. Phys. JETP **3** (1956) 920.

[2] L. D. Landau: Sov. Phys. JETP **5** (1957) 101.

[3] J. Kondo: Prog. Theor. Phys. **32** (1964) 37.

[4] H. Suhl: Phys. Rev. **138** (1965) A515; Physics 2 (1965) 39; Phys. Rev. **141** (1966) 483.

[5] Y. Nagaoka: Phys. Rev. **139** (1965) A1112.

[6] A. A. Abrikosov: Physics **2** (1965) 5.

[7] K. Yosida: Phys. Rev. **147** (1966) 223.

[8] P. W. Anderson: Phys. Rev. **164** (1967) 352.

[9] P. W. Anderson and G. Yuval: Phys. Rev. Lett. **23** (1969) 89.

[10] P. W. Anderson, G. Yuval and D. R. Hamann: Phys. Rev. B **1** (1970) 4464.

[11] G. Yuval and P. W. Anderson: Phys. Rev. B **1** (1970) 1522.

[12] P. W. Anderson: J. Phys. C **3** (1970) 2439.

[13] K. G. Wilson: Rev. Mod. Phys. **47** (1975) 773.

[14] L.P. Kadanoff: Physics **2** (1966) 263.

[15] Ph. Nozières: J. Low. Temp. Phys. **17** (1974) 31.

[16] K. Yosida and K. Yamada: Prog. Theor. Phys. Suppl. **46** (1970) 244.

[17] K. Yamada: Prog. Theor. Phys. **53** (1975) 970.

[18] K. Yosida and K. Yamada: Prog. Theor. Phys. **53** (1975) 1286.

[19] K. Yamada: Prog. Theor. Phys. **54** (1975) 316.

[20] N. Andrei: Phys. Rev. Lett. **45** (1980) 379.

[21] N. Andrei and J. H. Lowenstein: Phys. Rev. Lett. **46** (1981) 356.

[22] N. Andrei, K. Furuya and J. H. Lowenstein: Rev. Mod. Phys. **55** (1983) 331.

[23] P. B. Wiegmann: JETP. Lett. **31** (1980) 364.

[24] P. B. Wiegmann: J. Phys. **C14** (1981) 1463.

[25] N. Kawakami and A. Okiji: Phys. Lett. **86A** (1981) 463.

[26] A. Okiji and N. Kawakami: J. Appl. Phys. **55** (1984) 1931.

[27] A. M. Tsvelick and P. B. Wiegmann: Adv. Phys. **32** (1983) 453.

[28] H. R. Krishna-murthy, J. W. Wilkins and K. G. Wilson: Phys. Rev. B **21** (1980) 1003.

[29] H. R. Krishna-murthy, J. W. Wilkins and K. G. Wilson: Phys. Rev. B **21** (1980) 1044.

[30] D. M. Cragg, P. Lloyd and P. Nozières: J. Phys. C **13** (1980) 803.

[31] B. A. Jones, C. M. Varma, and J. W. Wilkins: Phys. Rev. Lett. **61** (1988) 125.

[32] O. Sakai, Y. Shimizu, and T. Kasuya: Solid State Commun. **75** (1990) 81-87.

[33] O. Sakai and Y. Shimizu: J. Phys. Soc. Jpn. **61** (1992) 2333.

[34] D. L. Cox and A. Zawadowski: Adv. Phys. **47** (1998) 599.

[35] S. Yotsuhashi, K. Miyake and H. Kusunose: J. Phys. Soc. Jpn. **71** (2002) 389.

[36] S. Nishiyama and K. Miyake: J. Phys. Soc. Jpn. **80** (2011) 124706.

Chapter 2

Effect of Competition between Inter-Site and Kondo-Yosida Singlet States on Charge Transfer Susceptibility in Heavy Fermion Systems

2.1 Introduction

In the last two decades or so, quantum phase transitions in heavy fermion systems have been one of main issues studied extensively. In particular, the quantum critical point (QCP) related to antiferromagnetic (AF) fluctuations in Ce-based compounds has attracted much attention. This spin fluctuations related to AF-QCP arises from competition between the AF long-range order and the Kondo effect, giving rise to many anomalous phenomena like non-Fermi liquid (NFL) temperature dependences in the resistivity, susceptibility and specific heat. Moreover, an unconventional superconductivity is also a signature of the AF-QCP.

It also turned out that there exist a series of materials, like $CeAl_2$[1], $YbNi_2Ge_2$[2], $CeCu_5Au$[3] and $CeRu_2(Si_{1-x}Ge_x)_2$ with $x \simeq 0.1$[4], which show an enhancement in the residual resistivity ρ_0 not at the AF-QCP but where the Néel temperature T_N coincides with the Kondo temperature T_K. Recently, enhancement in the Hall coefficient R_H has also been observed in $CeRu_2(Si_{1-x}Ge_x)_2$ at $x \simeq 0.1$ [4], where the same situation as above is realized. This anomalous property is not yet understood theoretically.

Recently, it was shown that such an enhancement in ρ_0 is caused by the fluctuations of the charge sector in f-electrons [5, 6]. In particular, it was demonstrated that the two-impurity Anderson model (TIAM) exhibits an enhancement in the f-electron charge susceptibility $\chi_f \equiv -(dn_f/d\varepsilon_f)$ where the Kondo-Yosida (KY) singlet state competes with the singlet state composed by an inter-site spin singlet state by an inter-site interaction, the Ruderman-Kittel-Kasuya-Yosida (RKKY) interaction [6]. This competition is expected to appear also in the lattice case, where $T_{\rm K} \sim T_{\rm N}$ when the pressure or the chemical doping is tuned, because such a competition arises when two singlet states have equal characteristic energy scales.

In this chapter, we examine how the competition between the RKKY singlet and the KY singlet states affects the Hall effect in a system described by the TIAM, which gives us a clue to understand the physical origin of the phenomenon of the enhanced $R_{\rm H}$ at the point where $T_{\rm K} \sim T_{\rm N}$. As a first step, we investigate the TIAM on the basis of the Wilson numerical renormalization group (NRG) method [7], and show that those fluctuations of the charge transfer (CT) between f- and conduction electrons are enhanced when the characteristic energy scale of the RKKY singlet state is comparable to $T_{\rm K}$, that of the KY singlet state. On this basis, we investigate how these enhanced CT fluctuations give a singular contribution to $R_{\rm H}$, giving an explanation for the enhanced $R_{\rm H}$ observed in $CeRu_2(Si_{1-x}Ge_x)_2$ at around $x \simeq 0.1$ [4].

2.2 Model Hamiltonian

The model Hamiltonian of the TIAM is given as follows:

$$\begin{aligned}\mathcal{H} = &\sum_{\vec{k}\sigma} \varepsilon_{\vec{k}} c^\dagger_{\vec{k}\sigma} c_{\vec{k}\sigma} + \varepsilon_f \sum_{i\sigma} f^\dagger_{i\sigma} f_{i\sigma} + U \sum_i f^\dagger_{i\uparrow} f_{i\uparrow} f^\dagger_{i\downarrow} f_{i\downarrow} \\ &+ VN^{-1} \sum_{i\vec{k}\sigma} \left(e^{i\vec{k}\cdot\vec{x}_m} c^\dagger_{\vec{k}\sigma} f_{i\sigma} + \text{h.c.} \right) + I \vec{J}_1 \cdot \vec{J}_2, \end{aligned} \tag{2.1}$$

where $f_{i\sigma}(f^\dagger_{i\sigma})$ and $c_{\vec{k}\sigma}(c^\dagger_{\vec{k}\sigma})$ are annihilation (creation) operators of the f-electron on the site $i(=1,2)$ with the energy ε_f and the conduction electrons with the kinetic energy $\varepsilon_{\vec{k}}$ which hybridize with f-electrons with strength V. U and $\vec{J}_i$ are the Coulomb repulsion and the pseudospin operators of each f-electron, and N is the number of sites. I is the inter-site exchange interaction between two f-electrons simulating the RKKY interaction, which is assumed to be antiferromagnetic, i.e., $I > 0$.

The TIAM has two conduction bands which hybridize with even(+) and odd(-) parity combinations of local orbitals $f_{p=\pm,\sigma} \equiv (f_{1\sigma} \pm f_{2\sigma})/\sqrt{2}$. This model has been investigated thoroughly and shown to exhibit two stable fixed points [8, 9, 10, 11]. One is the KY singlet fixed point where two f-electrons are screened out independently by corresponding conduction electrons, and the total phase shift of conduction electrons is equal to $\pi(=\pi/2+\pi/2)$. The other is the RKKY singlet fixed point where two f-electrons form the spin singlet state, and the total phase shift of conduction electrons is equal to 0. At the boundary between them, there exists the unstable fixed point (UFP) where NFL behaviors appear in various physical quantities when the conduction bands hold the particle-hole (PH) symmetry.

To analyze properties of the Hamiltonian (2.1) by the Wilson NRG method [7], we transform these conduction bands with the logarithmic discretization parameter $\Lambda = 2.5$. We control the degree of the competition through variation of I, and the other parameter set of the Hamiltonian (2.1) is fixed as $\varepsilon_f = -0.4, U = 1.0, V = 0.26$ in the unit of D (D being half the bandwidth of conduction electrons), and $k_{\rm F} r_{12} = \pi$ where $r_{12} \equiv |\vec{x}_1 - \vec{x}_2|$ is the distance between two impurities and $k_{\rm F}$ is the Fermi momentum. We keep states up to 4000 states in each iteration step in all the calculations below.

In order to investigate how the valence fluctuations in the f-electron site is affected by the competition. we define the following quantities:

$$T_z \equiv \sum_{p\sigma} (f^\dagger_{p\sigma} f_{p\sigma} - c^\dagger_{0p\sigma} c_{0p\sigma}). \tag{2.2}$$

$$T_x \equiv \sum_{p\sigma} (f^\dagger_{p\sigma} c_{0p\sigma} + c^\dagger_{0p\sigma} f_{p\sigma}), \tag{2.3}$$

where $c_{0p\sigma}$ is the annihilation operator of conduction electrons with parity p and spin σ localized with an extent from the impurity being $k_{\rm F}^{-1}\Lambda^{1/2}$. The susceptibilities of each direction, "x" and "z", are defined as $\chi_x \equiv -\partial\langle T_x\rangle/\partial V$ and $\chi_z \equiv -\partial\langle T_z\rangle/\partial\varepsilon_f$, respectively.

2.3 Charge Transfer Susceptibility

First, we show the results with the PH symmetric conduction bands. In the case of $I = 0$, we obtain the same Kondo temperatures for both parities as $T_{\rm Ks} = 2.08 \times 10^{-3}$ by using Wilson's definition $4T_{\rm K}\chi_{\rm imp}(T=0) = 0.413$. With increasing I, the ground state changes at $I = I_{\rm cr} = 0.01282$ from the KY singlet state to the RKKY singlet state.

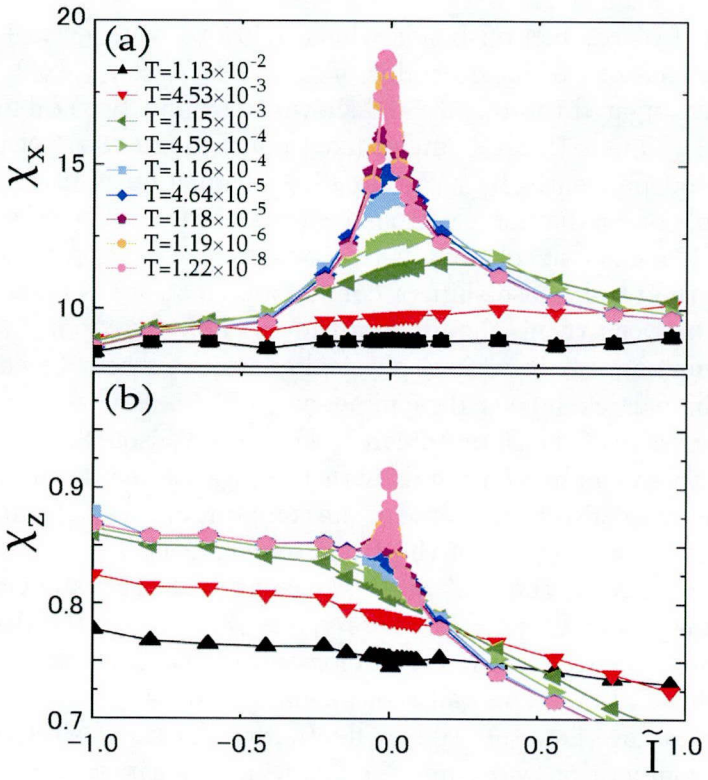

Figure 2.1: $\tilde{I}$ dependence of (a) χ_z and (b)χ_x for nine different temperatures.

Figure 2.1 shows the $\tilde{I} \equiv (I - I_{\rm cr})/I_{\rm cr}$ dependence of the static susceptibilities, χ_z and χ_x for various temperatures T, and Fig. 2.2 show the same figure but on the logarithmic scale of $\tilde{I}$. Both susceptibilities diverge at the critical point $\tilde{I} = 0$ as T decreases, although χ_x is larger than χ_z by more than ten times even away from the criticality. As seen in Fig. 2.2(a) and (b), both χ_z and χ_x take the logarithmic singularities of $\tilde{I}$, i.e., $-\log|\tilde{I}|$, in the low temperature limit. Except for this singularity at around $\tilde{I} \sim 0$, χ_z monotonously decreases with increasing $\tilde{I}$ as in the case of χ_f discussed in ref. [6], although χ_x does not show such a monotonous change. Such a monotonic decrease occurs even in the single impurity Anderson model with increasing V which stabilizes the KY singlet states. However, there exists no logarithmic divergence of $\chi_{x(z)}$ in the single impurity Anderson model: i.e., such a divergence in $\chi_{x(z)}$ is caused by the competition between the two singlet states.

As a more realistic situation, we also show the result without the PH asym-

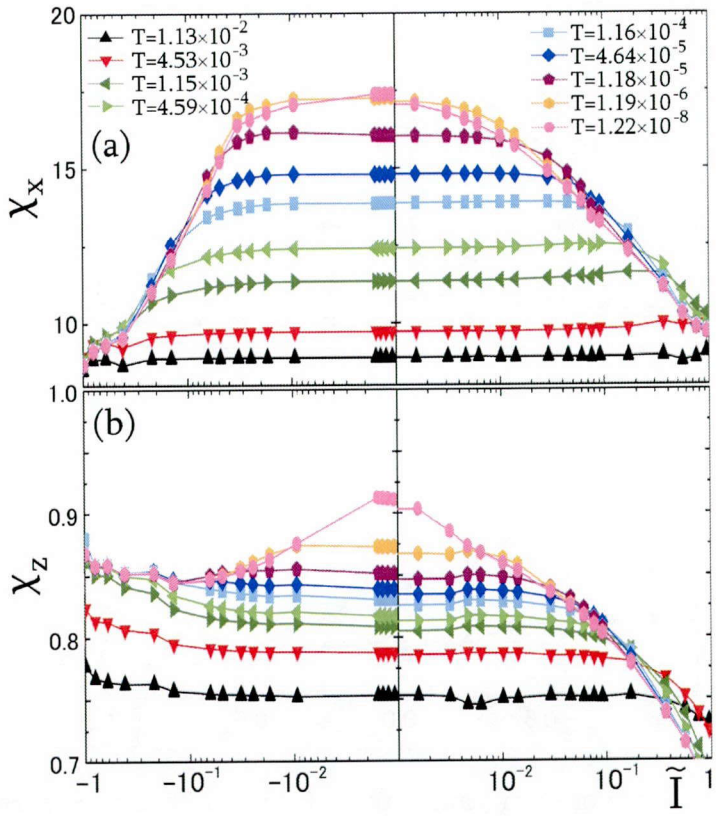

Figure 2.2: The same figure with Fig. 2.1 but on the logarithmic scale of $\tilde{I}$.

metric conduction bands. In the numerical calculation, we use linear dispersion $\varepsilon_{\vec{k}} \simeq v_{\rm F}(k - k_{\rm F})$ and $v_{\rm F}k_{\rm F} = D\pi$ where $v_{\rm F}$ is the Fermi velocity. In the case of $I = 0$, two KY singlet states are formed below each Kondo temperature, $T_{\rm Ka+} = 2.39 \times 10^{-3}$ for even parity channel and $T_{\rm Ka-} = 1.74 \times 10^{-3}$ for odd parity channel, which are close to $T_{\rm Ks}$. In this case, the UFP disappears and the total phase shift continuously varies between $\delta = 0$ and π [10]. However, the crossover from $\delta = 0$ and $\delta = \pi$ occurs very sharply, causing the pronounced enhancement in χ_f [6]. Here, according to ref. [6], we call the "hidden" UFP, which corresponds to $I = I_{\rm co} = 0.01302$.

Figure 2.2 shows the $\tilde{I}$ dependence of χ_z and χ_x for various temperatures for the PH asymmetric case. Here, we cannot see a striking difference between PH symmetric and PH asymmetric cases in static susceptibilities, while this difference can be seen in the dynamical susceptibility as discussed shortly.

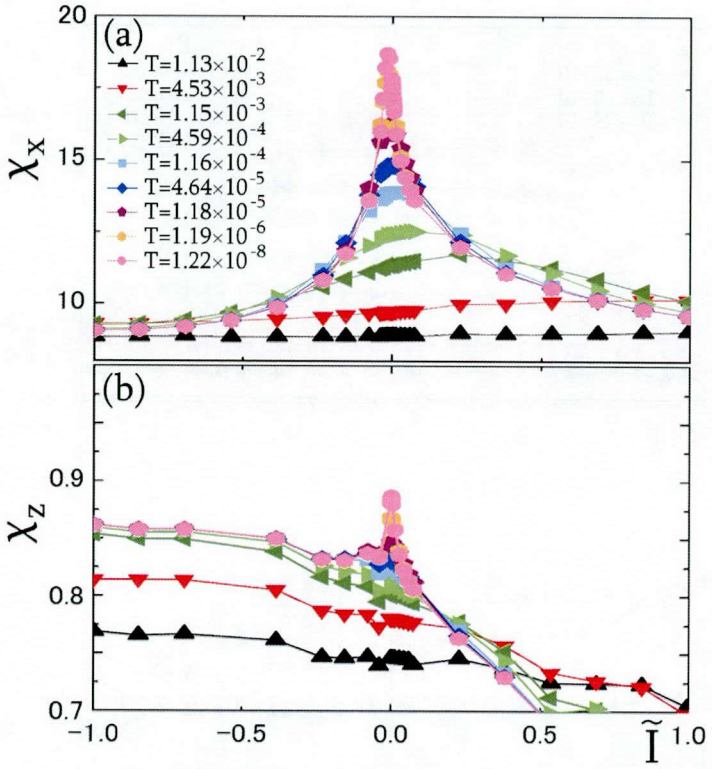

Figure 2.3: $\tilde{I}$ dependence of (a) χ_z and (b)χ_x for nine different temperatures for the model without PH symmetry.

Figure 2.5 shows the imaginary part of the dynamical susceptibilities of both $\chi_x(\omega)$ and $\chi_z(\omega)$ for (a) the PH symmetric and (b) the PH asymmetric cases. In both cases, $\mathrm{Im}\chi_z$ and $\mathrm{Im}\chi_x$ tend to take nonzero values even when $\omega < T_{\mathrm{Ks(a\pm)}}$ as the system approaches the UFP. However, in the PH asymmetric case (b), both susceptibilities decrease as $\mathrm{Im}\chi_z(x) \propto \omega$ at $\omega \lesssim 10^{-7}$, even at the "hidden" UFP. This is because the UFP disappears in the PH asymmetric case, while they remain nonzero at $\omega \to 0$ in the PH symmetric case. Such a difference between the PH symmetric and the PH asymmetric cases is expected to occur even in the static susceptibilities. However, it is difficult to calculate these susceptibilities in low temperatures with an enough accuracy because the parameter corresponding to the UFP is sensitive to tiny changes of V and ε_f for the differentiation of $\langle T_{x(z)} \rangle$.

We note again that $\mathrm{Im}\chi_x$ is larger than $\mathrm{Im}\chi_z$ by more than ten times in

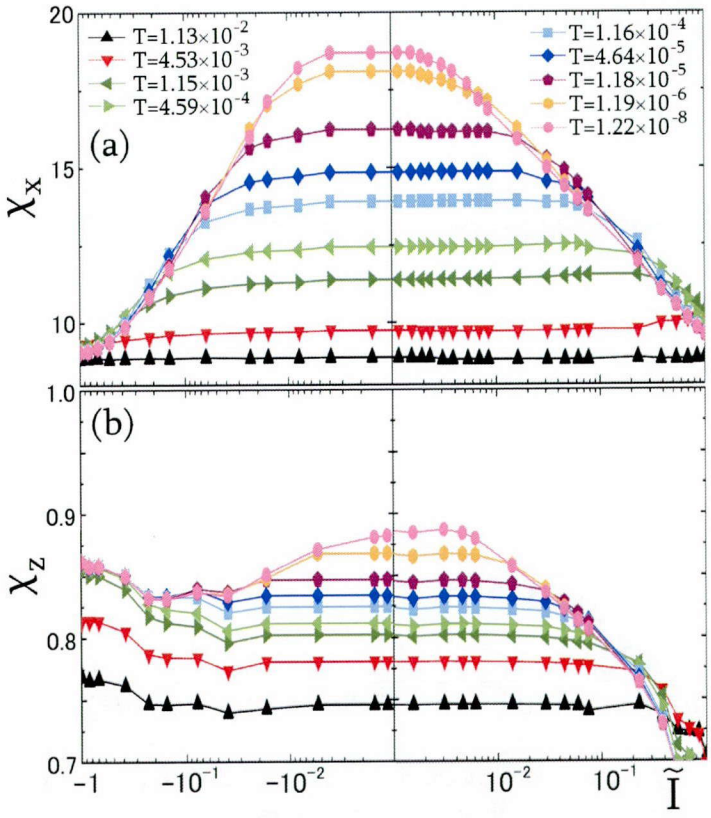

Figure 2.4: The same figure with Fig. 2.3 but on the logarithmic scale of $\tilde{I}$.

both cases, which means that the fluctuations of the charge sector in the "x"-direction are much larger than that in the "z"-direction. From this viewpoint, the original fluctuations in the charge sector may arise in the "x"-direction, and the fluctuations in the "z"-direction are induced by the fluctuations in the "x"-direction through the hybridization between the f- and the conduction electrons, i.e., $\chi_x \propto V^2\chi_z$. The origin of such anomalous behaviors is a critical valence fluctuations of f-electrons induced by the difference in the occupation number of f-electrons between the two fixed points [6]. This is because f-electrons have an itinerant character in the KY singlet fixed point while they have localized character in the RKKY singlet fixed point. There remains a residual entropy of $\log\sqrt{2}$ related to the quasi-degeneracy of these two fixed points [12], which gives the strong fluctuations in the charge sector.

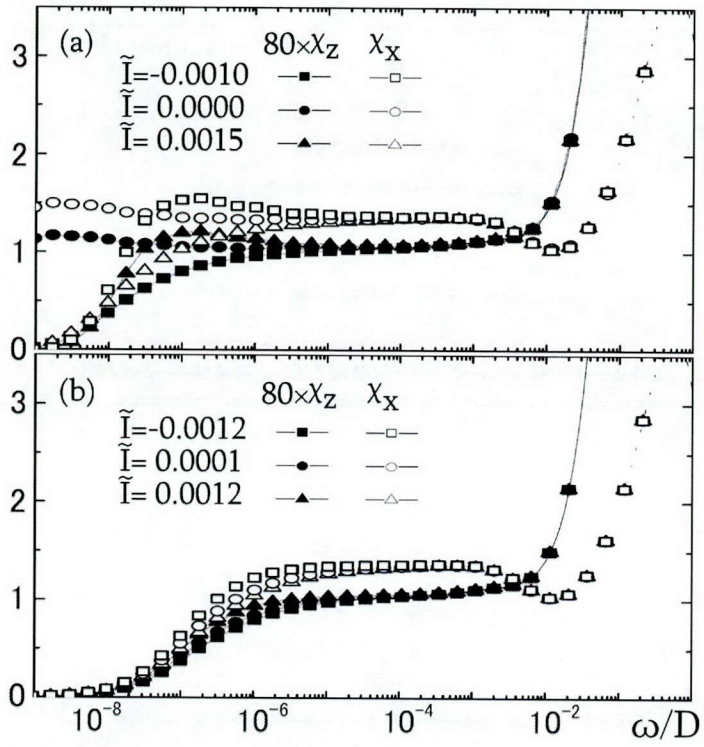

Figure 2.5: Imaginary part of the dynamical susceptibilities χ_z and χ_x for (a) the PH symmetric and (b) the PH asymmetric cases.

2.4 Discussion of Hall Coefficient

Next, let us discuss how these fluctuations contribute to the Hall coefficient $R_{\rm H}$ at the level of the impurity model. Since $\chi_x \sim 80\chi_z$, we only consider the correction by χ_x up to the first order for the diagonal and the Hall conductivities, σ_{xx} and σ_{xy}, extending the formalism given in ref. [13]. The formal expressions for these correction terms are

$$\Delta\sigma_{xx} = -n_{\rm imp}\frac{2e^2}{i\omega}V^2T^2\sum_{\vec{k}\varepsilon_n} F_{xx}(\vec{k}, i\tilde{\varepsilon}_n, i\tilde{\varepsilon}_n^-), \tag{2.1}$$

$$\Delta\sigma_{xy} = n_{\rm imp}\frac{e^3H}{m^2c\omega}V^2T^2\sum_{\vec{k}\varepsilon_n} F_{xy}(\vec{k}, i\tilde{\varepsilon}_n, i\tilde{\varepsilon}_n^-), \tag{2.2}$$

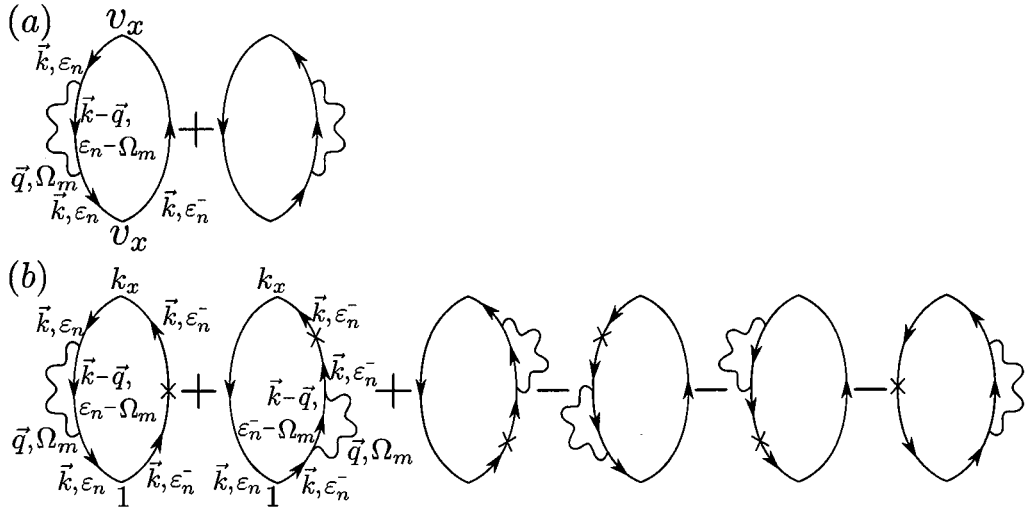

Figure 2.6: Diagrammatic representation of corrections for (a) the diagonal and (b) the off-diagonal conductivities. The solid lines with arrows are impurity-averaged Green's function, crosses indicates partial differentiation with respect to the x-component of wave vector, and wavy lines are the fluctuations propagators.

where $\tilde{\varepsilon}_n \equiv \varepsilon_n(1+1/2\tau|\varepsilon_n|)$, $\varepsilon_n^- \equiv \varepsilon_n - \omega_\lambda$, $\varepsilon_n \equiv (2n+1)\pi T$, $\tau^{-1} = 2\pi n_{\rm imp} u^2 N_{\rm F}$ with $n_{\rm imp}$ being the number density of impurities and u the Fourier component of the nonmagnetic impurity potential which is assumed to have only an s-wave component. We take the electronic charge as $e(<0)$, and diagrammatic representations of $F_{xx}(\vec{k},\tilde{\varepsilon}_n,\tilde{\varepsilon}_n^-)$ and $F_{xy}(\vec{k},\tilde{\varepsilon}_n,\tilde{\varepsilon}_n^-)$ are illustrated in Fig. 2.6(a) and (b), respectively. It is noted that the Aslamazov-Larkin type process [14] gives no contribution, unlike the case of superconducting fluctuations [15] because collective modes of the particle-hole process do not couple with current or velocity [16].

We perform summation in eqs. (2.1) and (2.2) by a procedure similar to that of ref. [13]. We adopt high temperature approximation by taking the only contribution, $\Omega_m = 0$, as dominant in Fig. 2.6. Using $G^{R(A)}(\vec{k},x) =$

$\left[x-\xi_{\vec{k}}+(-)i/2\tau\right]^{-1}$, the right-hand sides of eqs. (2.1) and (2.2) are given as

$$\Delta\sigma_{xx}=-2n_{\rm imp}\sigma_0 TV^2\tau\sum_{\vec{q}}\chi_x(\vec{q},0)\frac{\tan^{-1}(v_{\rm F}q\tau)}{v_{\rm F}q}, \tag{2.3}$$

$$\Delta\sigma_{xy}=n_{\rm imp}\sigma^0_{xy}TV^2\tau\sum_{\vec{q}}\chi_x(\vec{q},0)\left[\frac{4\tan^{-1}(v_{\rm F}q\tau)}{v_{\rm F}q}+\frac{\tau}{1+(v_{\rm F}q\tau)^2}\right], \tag{2.4}$$

where $\sigma^0_{xy}=-\omega_c\tau\sigma_0$, with $\omega_c=|e|H/mc$ and $\sigma_0=ne^2\tau/m$, with n being the carrier density. Using the fact that χ_x has no $\vec{q}$-dependence, $\chi_x(\vec{q},0)\equiv\chi_x$ in the impurity case, $\vec{q}$-integration is easily carried out leading to

$$\Delta\sigma_{xx}=-\pi n_{\rm imp}\sigma_0\frac{TV^2}{q_c v_{\rm F}}\tau\chi_x, \tag{2.5}$$

$$\Delta\sigma_{xy}=2\pi n_{\rm imp}\sigma^0_{xy}\frac{TV^2}{q_c v_{\rm F}}\tau\chi_x, \tag{2.6}$$

where q_c is the cut-off of the q-integration, $v_{\rm F}q_c$ being of the order of the Fermi energy of conduction electrons $\varepsilon_{\rm F}$. In deriving eqs. (2.5) and (2.6) from eqs. (2.3) and (2.4), we have assumed that the impurity scattering rate of conduction electrons is smaller than $\varepsilon_{\rm F}$, i.e., $\varepsilon_{\rm F}\tau\gg 1$. It has been shown in ref. 13 that, in the limit $T=0$, $\Delta R_{\rm H}$ comes from the momentum-dependence of the real part of self-energy function. In the present paper, we also take into account such a momentum-dependence of the self-energy function by considering the correction due to χ_x up to the first order as shown in Fig. 2.6, which gives rise to $\Delta R_{\rm H}$ being proportional to χ_x. It is noted that the self-energy of conduction electrons acquires the momentum dependence even though the charge transfer susceptibility χ_x has no its dependence.

Expanding σ_{xx} and σ_{xy} up to the linear term of $\Delta\sigma_{xx}$ and $\Delta\sigma_{xy}$, we obtain the correction to $R_{\rm H}=\sigma_{xy}/\sigma^2_{xx}H$ due to χ_x as follows:

$$\Delta R_{\rm H}\simeq\frac{\Delta\sigma_{xy}\sigma_0-2\Delta\sigma_0\sigma_{xy}}{H\sigma_0^3}=4\pi n_{\rm imp}\frac{\sigma^0_{xy}}{\sigma_0^2}\frac{V^2T}{v_{\rm F}q_c}\tau\chi_x. \tag{2.7}$$

This result remains valid even if we take the hole bands, in which $\sigma^0_{xy}=\omega_c\tau\sigma_0$ [13].

At around UFP, we can approximate $\chi_x\propto-\log\eta+$const, where η depends both on temperature T and deviation from the UFP $\tilde{I}$. Thus, η is expressed as $\eta(T,\tilde{I})=\bar{\eta}(T)+x$, with $x\equiv\eta(0,\tilde{I})$. Using this, the correction to $R_{\rm H}$ is given as

$$\Delta R_{\rm H}\propto-\log\left[\bar{\eta}(T)+x\right]+\text{const.} \tag{2.8}$$

This result implies that $R_{\rm H}$ has a peak structure at the UFP. Experimentally, x is changed by the chemical or real pressures, and $\bar{\eta}(T)$ decreases toward zero as T decreases.

This result can explain the enhanced $R_{\rm H}$ observed in $CeRu_2(Si_{1-x}Ge_x)_2$ at $x \simeq 0.1$ [4]. As demonstrated above in the case of the TIAM, $R_{\rm H}$ is expected to be enhanced also in the lattice system if valence fluctuations are developed. Indeed, such valence fluctuations are expected to occur at around $x \simeq 0.1$ where $T_{\rm K}$ is comparable with $T_{\rm N}$ [5, 6]. Although our discussions are carried out in the impurity level, it is expected that the same phenomenon occurs in lattice systems. Further theoretical extensions to lattice systems are necessary to elucidate the relation between the enhancement in $R_{\rm H}$ and the valence fluctuations. It is interesting to note that the enhancement in $R_{\rm H}$ was observed in $CeCu_2Si_2$ under the pressure [17, 18] at which sharp crossover of the valence of the Ce ion is observed [19], suggesting that strong valence fluctuations are developed. Such an enhancement of $R_{\rm H}$ can be explained qualitatively by an effect of critical valence fluctuation [20].

2.5 Discussion in Two-Orbital Anderson Model

We have also obtained the same result in the two-orbital Anderson model which exhibits similar UFP due to the competition between the Kondo-Yosida singlet and the crystalline-electric-field singlet states [21, 22]. In the Hamiltonian to discuss this issue, the f^2-states are also restricted to the four low-lying CEF states in the $J = 4$ manifold of tetragonal symmetry as shown in Fig. 2.7: i.e., we assume the Γ_4 singlet ground state and K and Δ represent the excitation energies. The f^2-states can be rewritten in the j-j coupling scheme using f^1-states in the $j = 5/2$ manifold whose Hilbert space is restricted to two low lying Kramers pairs. Using the following pseudospin states alloted to the f^1-states,

$$|\Gamma_{7+}^{(2)}\rangle = \frac{3}{\sqrt{14}}|+\frac{5}{2}\rangle - \sqrt{\frac{5}{14}}|-\frac{3}{2}\rangle \equiv |\uparrow, 0\rangle, \tag{2.1}$$

$$|\Gamma_{7-}^{(2)}\rangle = -\frac{3}{\sqrt{14}}|-\frac{5}{2}\rangle + \sqrt{\frac{5}{14}}|+\frac{3}{2}\rangle \equiv |\downarrow, 0\rangle, \tag{2.2}$$

$$|\Gamma_{6,+}\rangle = |+\frac{1}{2}\rangle \equiv |0, \uparrow\rangle, \tag{2.3}$$

$$|\Gamma_{6,-}\rangle = |-\frac{1}{2}\rangle \equiv |0, \downarrow\rangle, \tag{2.4}$$

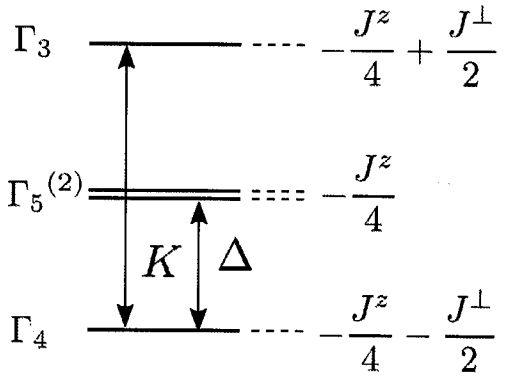

Figure 2.7: CEF level scheme of low-lying f^2 states and their eigenstates.

f^2-states are written as follows [11,13]:

$$|\Gamma_4\rangle = \frac{1}{\sqrt{2}}(|+2\rangle - |-2\rangle) = \frac{1}{\sqrt{2}}(|\downarrow,\uparrow\rangle - |\uparrow,\downarrow\rangle), \tag{2.5}$$

$$|\Gamma_3\rangle = \frac{1}{\sqrt{2}}(|+2\rangle + |-2\rangle) = \frac{1}{\sqrt{2}}(|\uparrow,\downarrow\rangle + |\downarrow,\uparrow\rangle), \tag{2.6}$$

$$|\Gamma^{(2)}_{5,+}\rangle = \beta|+3\rangle - \alpha|-1\rangle = |\uparrow,\uparrow\rangle, \tag{2.7}$$

$$|\Gamma^{(2)}_{5,-}\rangle = \beta|-3\rangle - \alpha|+1\rangle = |\downarrow,\downarrow\rangle. \tag{2.8}$$

With the use of the pseudospin states (2.1)-(2.4), the f^2-level scheme is reproduced by the "antiferromagnetic" Hund's-rule coupling [11, 13],

$$\mathcal{H}_{\rm Hund} = \frac{J_\perp}{2}\left[S_1^+ S_2^- + S_1^- S_2^+\right] + J_z S_1^z S_2^z, \tag{2.9}$$

where coupling constants are defined as $J_\perp = K$ and $J_z = 2\Delta - K$, respectively. $\vec{S}_m$ is a pseudospin operator of the f-electron in the Hilbert space of f^1-state spanned by the orbitals $m = 1$ ($\Gamma_7^{(2)}$) or 2 (Γ_6), and is defined as

$$\vec{S}_m \equiv \frac{1}{2} f^\dagger_{m\sigma} \vec{\sigma}_{\sigma,\sigma'} f_{m\sigma'}, \tag{2.10}$$

where $f_{m\sigma}$ is an annihilation operator of the f-electron in orbital m.

Thus the two-orbital Anderson model in tetragonal symmetry is given by

the following form [11, 13]:

$$\mathcal{H} = \mathcal{H}_{\rm c} + \mathcal{H}_{\rm hyb} + \mathcal{H}_{\rm f} + \mathcal{H}_{\rm Hund}, \tag{2.11}$$

$$\mathcal{H}_{\rm c} = \sum_{m=1,2} \sum_{\vec{k}\sigma} \varepsilon_{\vec{k}} c^{\dagger}_{\vec{k}m\sigma} c_{\vec{k}m\sigma}, \tag{2.12}$$

$$\mathcal{H}_{\rm hyb} = \sum_{m=1,2} \sum_{\vec{k}\sigma} \left(V_m c^{\dagger}_{\vec{k}m\sigma} f_{m\sigma} + {\rm h.c.} \right), \tag{2.13}$$

$$\mathcal{H}_{\rm f} = \sum_{m\sigma} E_{fm} f^{\dagger}_{m\sigma} f_{m\sigma} + \sum_{m} U_m f^{\dagger}_{m\uparrow} f_{m\uparrow} f^{\dagger}_{m\downarrow} f_{m\downarrow}, \tag{2.14}$$

where $c_{m\vec{k}\sigma}$ is an annihilation operator of a conduction electron with the wave vector $\vec{k}$ and the spin σ hybridizing with the f-electron in orbital m with a strength V_m. E_{fm} and U_m are the energy level of the f-electron and an intra-orbital Coulomb repulsion in orbital m, and the other Coulomb repulsion terms, like an inter-orbital interaction, are implicitly included in the "antiferromagnetic" Hund's-rule coupling (4.10).

The Hamiltonian (2.11) has two stable fixed points. One is the K-Y singlet fixed point where the spin degree of freedom of each f-electron is screened by the conduction electrons with the same symmetry as the f-electron, leading to the phase shift in the unitarity limit as $\delta_m = \pi/2$ $(m = 1, 2)$. The other is the CEF singlet fixed point where two f-electrons form the singlet state due to the CEF effect, characterized by $\delta_m = 0$ $(m = 1, 2)$. Along the boundary of these two stable-fixed-point regions, there exists a locus of the unstable fixed points across which the ground state is interchanged. Around this line, NFL behaviors appear at $T^*_{\rm F} < T < T_x = \min(T_{\rm K2}, K)$, where $T_{\rm K2}$ is the lower Kondo temperature of two f-orbitals.

We control the degree of the competition by varying the CEF level splitting Δ, and the other parameters of the Hamiltonian (2.11) are fixed as $E_{f1} = -0.4$, $E_{f2} = -0.3, U_1 = U_2 = 1.0, V_1 = 0.45$, $V_2 = 0.30$ and $K = 0.20$ in the unit of D throughout this section. In the case of $K = \Delta = 0$, the Hamiltonian (4.11) reduces to two independent impurity Anderson models, where the Kondo temperatures determined by the Wilson's definition, $4T_{\rm K}\chi_{\rm imp}(T = 0) = 0.413$, are $T_{\rm K1} = 6.48 \times 10^{-2}$ and $T_{\rm K2} = 9.28 \times 10^{-3}$, respectively. With increasing Δ, the ground state changes at $\Delta = \Delta_{\rm cr} = 0.1263$ from the K-Y singlet state to the f^2-CEF singlet state.

In order to see the valence fluctuations susceptibility in the f-electron site,

we again define the following quantities:

$$T_z \equiv \sum_{m\sigma} (f^\dagger_{m\sigma} f_{m\sigma} - c^\dagger_{0m\sigma} c_{0m\sigma}), \tag{2.15}$$

$$T_x \equiv \sum_{m\sigma} (f^\dagger_{m\sigma} c_{0m\sigma} + c^\dagger_{0m\sigma} f_{m\sigma}), \tag{2.16}$$

where $c_{0m\sigma}$ is the annihilation operator of conduction electrons in orbital m and spin σ localized with an extent from the impurity being $k_{\rm F}^{-1}\Lambda^{1/2}$. The susceptibilities of each direction, "x" and "z", are defined as follow:

$$\chi_x \equiv -\frac{{\rm d}\langle T_x\rangle}{{\rm d}V} = -\frac{\partial\langle T_x\rangle}{\partial V_1} - \frac{\partial\langle T_x\rangle}{\partial V_2} \tag{2.17}$$

$$\chi_z \equiv -\frac{{\rm d}\langle T_z\rangle}{{\rm d}\varepsilon_f} = -\frac{\partial\langle T_z\rangle}{\partial \varepsilon_{f1}} - \frac{\partial\langle T_z\rangle}{\partial \varepsilon_{f2}}. \tag{2.18}$$

Figure 2.8 shows the $\tilde{\Delta} \equiv (\Delta - \Delta_{\rm cr})/\Delta_{\rm cr}$ dependence of the static susceptibilities, χ_z and χ_x for various temperatures T on the logarithmic scale of $\tilde{\Delta}$. As in the case of the two-impurity Anderson model, both susceptibilities diverge in the form $-\log|\tilde{\Delta}|$ at the critical point $\tilde{\Delta} = 0$ as T decreases, and χ_x is larger than χ_z by about ten times even away from the criticality. Although it is not shown, the same result as the case of the two-impurity Anderson model is obtained about the dynamical susceptibilities.

This result is natural because both the two-orbital and the two-impurity Anderson model have similar type of UFP. Therefore, we expect that there exist materials which show an enhancement in the Hall coefficient in heavy fermion systems with f^2-configuration.

2.6 Summary

In summary, we have investigated the charge transfer susceptibilities $\chi_{x(z)}$ between f-electrons and conduction bands in the two-impurity Anderson model. In both cases of the PH symmetric and asymmetric conduction bands, we have shown that $\chi_{x(z)}$ diverges where the KY singlet and the RKKY singlet states mostly compete. In particular, χ_x gives a dominant contribution to the enhancement in the Hall coefficient through that to the diagonal and the off-diagonal conductivities. This result gives a possible scenario for understanding the enhancement in the Hall coefficient observed in some heavy fermion materials, like $CeRu_2(Si_{1-x}Ge_x)_2$ at $x \simeq 0.1$ [4], where $T_{\rm N}$ coincides with $T_{\rm K}$.

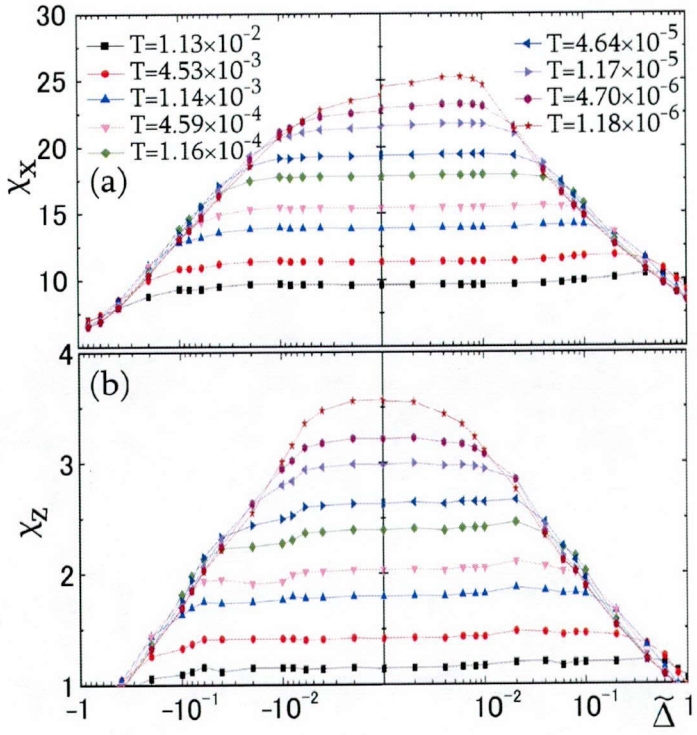

Figure 2.8: $\tilde{I}$ dependence of (a) χ_z and (b)χ_x for nine different temperatures.

Bibliography of Chapter 2

[1] B. Barbara, J. Beille, B. Cheaito, J. M. Laurant, M. F. Rossignol, A. Waintal, and S. Zemirli: J. Phys. (Paris) **48** (1987) 635.

[2] G. Knebel, D. Braithwaite, G. Lapertot, P. C. Canfield, and J. Flouquet: J. Phys: Condens. Matter **13** (2001) 10935.

[3] H. Wilhelm, S. Raymond, D. Jaccard, O. Stockert, H. v. Löhneysen, and A. Rosch: J. Phys: Condens. Matter **13** (2001) L329.

[4] Y. Matsumoto, M. Sugi, K. Aoki, Y. Shimizu, N. Kimura, T. Komatsubara, H. Aoki, M. Kimata, T. Terashima, and S. Uji: J. Phys. Soc. Jpn. **80** (2011) 074715.

[5] K. Miyake and H. Maebashi: J. Phys. Soc. Jpn. **71** (2002) 1007.

[6] K. Hattori and K. Miyake: J. Phys. Soc. Jpn. **79** (2010) 073702.

[7] K. G. Wilson: Rev. Mod. Phys. **47** (1975) 773.

[8] B. A. Jones, C. M. Varma, and J. W. Wilkins: Phys. Rev. Lett. **61** (1988) 125.

[9] O. Sakai, Y. Shimizu, and T. Kasuya: Solid State Commun. **75** (1990) 81-87.

[10] O. Sakai and Y. Shimizu: J. Phys. Soc. Jpn. **61** (1992) 2333.

[11] D. L. Cox and A. Zawadowski: Adv. Phys. **47** (1998) 599.

[12] I. Affleck, A. W. W. Ludwig, and B. A. Jones: Phys. Rev. B **52** (1995) 9528.

[13] H. Fukuyama, H. Ebisawa, and Y. Wada: Prog. Theor. Phys. **42** (1969) 494.

[14] L. G. Asmalazov and A. I. Larkin: Sov.-Phys. Solid State **10** (1968) 875; Phys. Lett. **26A** (1968) 238.

[15] H. Fukuyama, H. Ebisawa, and T. Tsuzuki: Prog. Theor. Phys. **46** (1971) 1028.

[16] O. Narikiyo: private communication.

[17] G. Seyfarth, A. -S. Rüetschi, K. Sengupta, A. Georges, D. Jaccard, S. Watanabe, and K. Miyake: Phys. Rev. B **85** (2012) 205105.

[18] S. Araki, Y. Shiroyama, Y. Ikeda, T. C. Kobayashi, S. Seiro, C. Geibel, and F. Steglich: J. Phys. Soc. Jpn. Supple. A **80** (2011) SA061.

[19] K. Fujiwara, Y. Hata, K. Kobayashi, K. Miyoshi, J. Takeuchi, Y. Shimaoka, H. Kotegawa, T. C. Kobayashi, C. Geibel, and F. Steglich: J. Phys. Soc. Jpn. **77** (2008) 123711; private communication.

[20] K. Miyake and S. Watanabe: unpublished.

[21] S. Yotsuhashi, K. Miyake, and H. Kusunose: J. Phys. Soc. Jpn. **71** (2002) 389.

[22] S. Nishiyama and K. Miyake: J. Phys. Soc. Jpn. **80** (2011) 124706.

Chapter 3

Magnetically Robust Non-Fermi Liquid Behavior in Heavy Fermion Systems with f^2-Configuration: Competition between Crystalline-Electric-Field and Kondo-Yosida Singlet States

3.1 Introduction

In the last decade or so, non-Fermi liquid (NFL) behaviors around quantum critical point (QCP) have been one of main issues in physics, not only in heavy fermion systems [1], but also in those exhibiting the Mott transition [2]. Of these NFL behaviors, those of heavy fermion systems with f^2-configuration form a kind of subclass in which the QCP is triggered by local criticalities: such as the two-channel Kondo effect (TCKE) due to the non-Kramers doublet state [3, 4], and that caused by the competition between the crystalline-electric field (CEF) singlet and the Kondo-Yosida (K-Y) singlet states [5, 6]. The former TCKE was reported to be observed in $La_{1-x}Pr_xPb_3$ that has a Γ_3 non-Kramers doublet ground state in the cubic symmetry [7]. The NFL behaviors in $Th_{1-x}U_xRu_2Si_2$ were understood in a unified way by assuming that the system is located near the phase boundary between the CEF singlet and the

K-Y singlet states [5]. However, a detailed study about the magnetic field dependence on NFL behaviors has not been performed so far.

In the present chapter, we investigate the magnetic field dependence of NFL behaviors in the specific heat $C_{\rm imp}(T)$ and the entropy $S_{\rm imp}(T)$ due to f-electrons with the two-orbital impurity Anderson model in a tetragonal symmetry with the CEF singlet ground state on the basis of the numerical renormalization group (NRG) method [8, 9]. We discuss how the magnetic field, H_z, changes the characteristic temperature, $T_{\rm F}^*$, which is defined as the temperature at which the temperature derivative of entropy, $\partial S_{\rm imp}(T)/\partial(\log T)$, takes the maximum value as $S_{\rm imp}(T)$ approaching 0 as $T \to 0$. In the vicinity of the QCP, $T_{\rm F}^*$ is suppressed by the effect of the competition between the CEF singlet and the K-Y singlet states for $H_z = 0$, and the NFL behaviors occur at $T_{\rm F}^* < T < T_{\rm K2}$, where $T_{\rm K2}$ is the lower Kondo temperature of two orbitals, as in the case of TCKE. The magnetic field is shown not to affect $T_{\rm F}^*$ up to a certain value H_z^* which is determined approximately by the condition that the effect of the magnetic field, destroying a criticality of the TCKE type, becomes comparable to the effect of the deviation from the criticality at $H_z = 0$. H_z^* so determined is far larger than $T_{\rm F}^*(H_z = 0)$ for a reasonable set of parameters. As a result, the NFL behaviors become robust against the magnetic field up to $H_z^* \sim T_{\rm K2}$ which is about hundred times larger than $T_{\rm F}^*(H_z = 0)$.

This chapter is organized as follows. In §3.2, the model Hamiltonian is introduced and transformed into a form suitable for the NRG calculation. In §3.3, we discuss how the characteristic temperature $T_{\rm F}^*$ is affected by the effect of the competition between the CEF singlet and the K-Y singlet states in the case of $H_z = 0$. In §3.4, we demonstrate the magnetic field dependence of $T_{\rm F}^*$ and $\gamma_{\rm imp}(T) = C_{\rm imp}/T$. In the vicinity of the QCP, there are parameter regions where $-\log T$ behavior of $\gamma_{\rm imp}$, at temperature $T_{\rm F}^* < T < \min(T_{\rm K}, \Delta)$, is robust against the magnetic field. In §3.5, we investigate how such an anomalous NFL is affected by the change of the characteristic energy scale of two singlet states. In §3.6, we summarize our results and discuss their applicability for understanding the magnetically robust NFL behaviors observed in UBe_{13} because such an NFL being robust against the magnetic field can arise in systems with other symmetry if the K-Y singlet state and the CEF singlet state compete for the ground state.

3.2 Model Hamiltonian

In this section, we recapitulate discussions of ref. 5 about how to derive the model Hamiltonian for discussing the competition between the K-Y singlet

and the CEF singlet states in f^2-configuration on the basis of the j-j coupling scheme in the tetragonal symmetry. We restrict the f^1 state within two low-lying doublet states out of three doublets of $j = 5/2$ orbitals, and allot the pseudospin representation for these states as follows:

$$|\Gamma_{7+}^{(2)}\rangle = \frac{3}{\sqrt{14}}|+\frac{5}{2}\rangle - \sqrt{\frac{5}{14}}|-\frac{3}{2}\rangle \equiv |\uparrow,0\rangle, \tag{3.1}$$

$$|\Gamma_{7-}^{(2)}\rangle = -\frac{3}{\sqrt{14}}|-\frac{5}{2}\rangle + \sqrt{\frac{5}{14}}|+\frac{3}{2}\rangle \equiv |\downarrow,0\rangle, \tag{3.2}$$

$$|\Gamma_{6,+}\rangle = |+\frac{1}{2}\rangle \equiv |0,\uparrow\rangle, \tag{3.3}$$

$$|\Gamma_{6,-}\rangle = |-\frac{1}{2}\rangle \equiv |0,\downarrow\rangle. \tag{3.4}$$

Here, for example, $|\uparrow,0\rangle$ represents the state where orbital 1 ($\Gamma_7^{(2)}$) with up pseudospin is occupied and orbital 2 (Γ_6) is empty. We also restrict the f^2 state within four low-lying states out of states allowed in $J = 4$ manifold, and construct these four states with the direct product of f^1 states. Here, we have discarded states where two f-electrons occupy the same orbital, $|\uparrow\downarrow,0\rangle$, $|0,\uparrow\downarrow\rangle$, because the intra-orbital Coulomb repulsion is larger than the inter-orbital one. Then, low-lying four f^2 states are expressed as

$$|\Gamma_4\rangle = \frac{1}{\sqrt{2}}(|+2\rangle - |-2\rangle) = \frac{1}{\sqrt{2}}(|\downarrow,\uparrow\rangle - |\uparrow,\downarrow\rangle), \tag{3.5}$$

$$|\Gamma_3\rangle = \frac{1}{\sqrt{2}}(|+2\rangle + |-2\rangle) = \frac{1}{\sqrt{2}}(|\uparrow,\downarrow\rangle + |\downarrow,\uparrow\rangle), \tag{3.6}$$

$$|\Gamma_{5,+}^{(2)}\rangle = \beta|+3\rangle - \alpha|-1\rangle = |\uparrow,\uparrow\rangle, \tag{3.7}$$

$$|\Gamma_{5,-}^{(2)}\rangle = \beta|-3\rangle - \alpha|+1\rangle = |\downarrow,\downarrow\rangle. \tag{3.8}$$

It is noted that we cannot determined coefficients, α and β, because we have discarded one of the doublet in f^1-configuration. Therefore, in this chapter, we take its j-j coupling representation as f^2 states with $\Gamma_5^{(2)}$ symmetry as shown in Appendix including the derivation of eqs.(3.1)-(3.8).

We assume that the CEF ground state is the singlet (Γ_4), the first excited CEF states are magnetic doublet (Γ_5) with the excitation energy Δ, and the second excited CEF state is the singlet (Γ_3) with the excitation energy K, as shown in Fig.3.1. Such a CEF level scheme can be reproduced by introducing the "antiferromagnetic Hund's-rule coupling" for the pseudospin as

$$\mathcal{H}_{\rm Hund} = \frac{J_\perp}{2}\left[S_1^+ S_2^- + S_1^- S_2^+\right] + J_z S_1^z S_2^z, \tag{3.9}$$

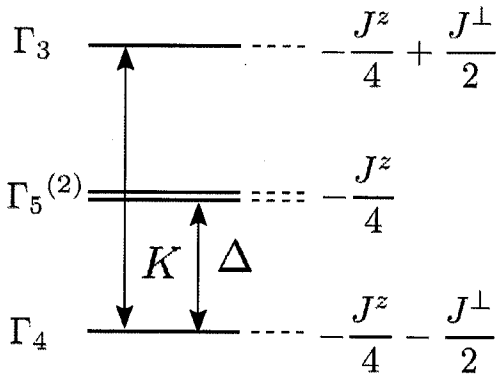

Figure 3.1: CEF level scheme of low-lying f^2 states and their eigenstates.

where coupling constants are defined as $J_\perp = K$ and $J_z = 2\Delta - K$, respectively, and $\vec{S}_i$ is a pseudospin operator of the localized electron in the orbital i defined as

$$\vec{S}_i = \frac{1}{2}\sum_{\sigma\sigma'} f^\dagger_{i\sigma}\vec{\sigma}_{\sigma\sigma'}f_{i\sigma'}. \tag{3.10}$$

Furthermore, assuming that f-electrons constructing the f^2 state hybridize with conduction electrons which have the same symmetry as each f^1 state. Thus the system can be described by the two-orbital impurity Anderson model with the "antiferromagnetic Hund's-rule coupling" as follows:

$$\mathcal{H} = \mathcal{H}_{\rm c} + \mathcal{H}_{\rm hyb} + \mathcal{H}_{\rm f} + \mathcal{H}_{\rm Hund}, \tag{3.11}$$

$$\mathcal{H}_{\rm c} = \sum_{i=1,2}\sum_{\vec{k}\sigma} \varepsilon_{\vec{k}} c^\dagger_{\vec{k}i\sigma} c_{\vec{k}i\sigma}, \tag{3.12}$$

$$\mathcal{H}_{\rm hyb} = \sum_{i=1,2}\sum_{\vec{k}\sigma} \left(V_{i\vec{k}} c^\dagger_{\vec{k}i\sigma} f_{i\sigma} + {\rm h.c.} \right), \tag{3.13}$$

$$\mathcal{H}_{\rm f} = \sum_{i=1,2}\sum_{\sigma} E_{fi} f^\dagger_{i\sigma} f_{i\sigma} + \sum_{i=1,2}\sum_{\sigma} \frac{U_i}{2} f^\dagger_{i\sigma} f^\dagger_{i\bar{\sigma}} f_{i\bar{\sigma}} f_{i\sigma}, \tag{3.14}$$

where $f_{i\sigma}(f^\dagger_{i\sigma})$ and $c_{\vec{k}i\sigma}(c^\dagger_{\vec{k}i\sigma})$ are annihilation (creation) operators of the f-electron on the orbital i with the energy E_{fi} and the conduction electron with wave vector $\vec{k}$ hybridizing with the f-electron with the symmetry of the orbital i with strength $V_{i\vec{k}}$. Here, the on-site intra-orbital Coulomb repulsion U_i is explicitly taken into account, while other Coulomb repulsion terms like

the inter-orbital or the exchange interaction, are implicitly included in the "antiferromagnetic Hund's-rule coupling" of (3.9).

To analyze properties of the system described by the Hamiltonian (3.11) by the Wilson NRG method [8, 9], we transform the conduction electron part as usual. For simplicity, we take conduction bands to be isotropic in momentum space, i.e. the hybridization depends only on the orbital i, $V_{i\vec{k}} \equiv V_i$, and symmetric in the energy space (with an extent from $-D$ to D) about the Fermi level. We discretize conduction bands logarithmically with the discretization parameter, Λ, and perform the unitary transformation assuming the density of state in conduction bands as constant. Thus, eqs. (3.12) and (3.13) can be rewritten as

$$\mathcal{H}_{\rm c} = \sum_{i,\sigma}\sum_{n=0}^{\infty} \Lambda^{-n/2} t_n \left(f^\dagger_{i,n\sigma} f_{i,n+1\sigma} + f^\dagger_{i,n+1\sigma} f_{i,n\sigma} \right), \tag{3.15}$$

$$\mathcal{H}_{\rm hyb} = \sum_{i,\sigma} V_i \left(f^\dagger_{i,0\sigma} f_{i,-1\sigma} + f^\dagger_{i,-1\sigma} f_{i,0\sigma} \right), \tag{3.16}$$

where $f_{i,n}$ ($f^\dagger_{i,n}$) is the annihilation (creation) operator of the conduction electron in the shell orbital whose extent is $k_{\rm F}\Lambda^{n/2}$ and $f_{i,-1\sigma} \equiv f_{i\sigma}$. The hopping integral between n-th and $(n+1)$-th shell states, t_n, is expressed as

$$t_n = \frac{D(1+\Lambda^{-1})(1-\Lambda^{-n-1})}{2\sqrt{(1-\Lambda^{-2n-1})(1-\Lambda^{-2n-3})}}. \tag{3.17}$$

Then, we define $\mathcal{H}_N$ which approaches $\mathcal{H}/(D(1+\Lambda^{-1})/2)$ in the limit $N \to \infty$ as follows:

$$\begin{aligned} \mathcal{H}_N = \Lambda^{(N-1)/2} \Bigg[& \tilde{\mathcal{H}}_{\rm f} + \sum_{i,\sigma} \tilde{V}_i \left(f^\dagger_{i,0\sigma} f_{i,-1\sigma} + f^\dagger_{i,-1\sigma} f_{i,0\sigma} \right) \\ & + \sum_{i,\sigma}\sum_{n=0}^{N-1} \Lambda^{-n/2} \tilde{t}_n \left(f^\dagger_{i,n\sigma} f_{i,n+1\sigma} + f^\dagger_{i,n+1\sigma} f_{i,n\sigma} \right) \Bigg], \end{aligned} \tag{3.18}$$

where the tilde indicates that energies are measured in a unit of $D(1+\Lambda^{-1})/2$. The Hamiltonian (3.18) satisfies the recursion relation

$$\mathcal{H}_{N+1} = \Lambda^{1/2}\mathcal{H}_N + \sum_{i\sigma} \tilde{t}_N \left(f^\dagger_{i,N\sigma} f_{i,N+1\sigma} + f^\dagger_{i,N+1\sigma} f_{i,N\sigma} \right). \tag{3.19}$$

We solve the whole sequence of Hamiltonian ($\mathcal{H}_N$) by using the recursive form (3.19) with keeping states up to 1500 states in each iteration step, and use $\Lambda = 3.0$ in all the calculations below unless explicitly stated.

3.3 Non-Fermi Liquid Behavior due to Competition between Crystalline-Electric-Field and Kondo-Yosida Singlets

In this section, we discuss the effect of the competition between the CEF singlet and the K-Y singlet states, which can give rise to a NFL state. It is already known that the system described by the Hamiltonian (3.11) has the competition between the K-Y singlet and the f^2-CEF singlet states [5]. In general, the energy level and the strength of hybridization with conduction electron in each f-orbital are different. In the present chapter, we take parameters so that the Kondo temperature of orbital 2 is always lower than that of orbital 1: i.e., we set parameters of the two-orbital impurity Anderson model, eq (3.11), as $E_{f1} = E_{f2} = -0.4, U_1 = U_2 = 1.0, V_1 = 0.45$, and $V_2 = 0.3$. Hereafter, the unit of energy is taken as D unless stated explicitly. In the case of $K = \Delta = 0$, the model Hamiltonian, eq. (3.11), reduces to two independent impurity Anderson models. The Kondo temperature of each orbital can be determined by the Wilson's definition, $4T_{\rm K}\chi_{\rm imp}(T = 0) = 0.413$, for conventional Anderson model as $T_{\rm K1} = 6.10 \times 10^{-2}$ and $T_{\rm K2} = 6.01 \times 10^{-3}$, respectively.

For the finite value of CEF parameters, (K, Δ), there are two stable Fermi Liquid (FL) fixed points corresponding to two singlet ground states as shown in Fig.3.2: the K-Y singlet (filled circles) and the CEF singlet (open circles) fixed points. At the boundary of these two regions of FL fixed points, there exists a curve of critical points, across which energy spectra for even and odd iteration interchange, and NFL behaviors appear in the vicinity of the boundary. To analyze further, we fix one of the CEF parameters as $K = 0.16$, and calculate the physical properties for a series of values of the CEF splitting parameter Δ. Analyzing near the critical point in more detail, the critical value of Δ is determined as $\Delta^* \simeq 0.112$ for $K = 0.16$.

Fig.3.3 shows the result of the temperature dependence of $S_{\rm imp}(T)$, the entropy due to f-electrons, near the critical point. As mentioned above, the characteristic temperature $T_{\rm F}^*$ is defined as the temperature at which the temperature derivative of entropy, $\partial S_{\rm imp}(T)/\partial(\log T)$, takes the maximum value just before $S_{\rm imp}(T)$ approaching 0 as $T \to 0$. As seen in Fig.3.3, $T_{\rm F}^*$ is drastically suppressed by the effect of the competition near the critical value of CEF splitting $\Delta = 0.112 \simeq \Delta^*$.

Fig.3.4 shows the Δ dependence of $T_{\rm F}^*$ which is obtained by numerical calculations of $S_{\rm imp}(T)$. In the case of $\Delta < \Delta^*$, the K-Y singlet state is the ground state, and two localized moments $\vec{S}_1$ and $\vec{S}_2$ are screened out independently by corresponding conduction electrons, where each Kondo temperature is affected

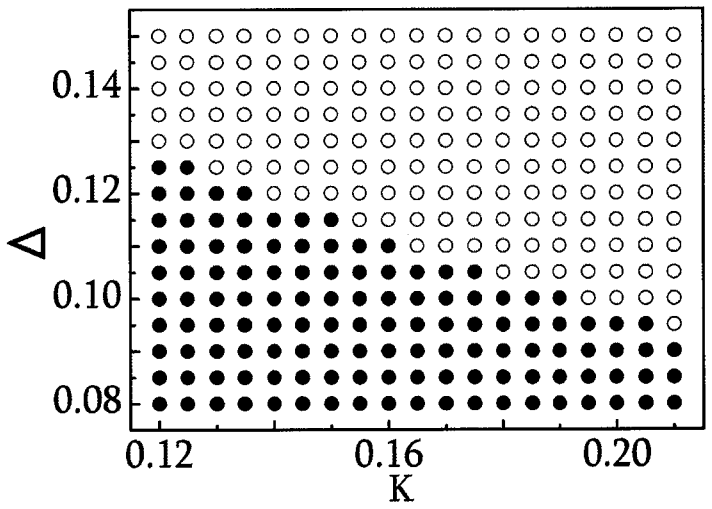

Figure 3.2: Phase diagram of the ground state in $K - \Delta$ plane. Filled circles represent the K-Y singlet fixed point and open circles represent the f^2-CEF singlet fixed point. Parameter set is $E_{f1} = E_{f2} = -0.4, U_1 = U_2 = 1.0, V_1 = 0.45$, and $V_2 = 0.3$.

by the interaction between f-electrons. In this case, the total phase shift of conduction electrons characterizing this fixed point is $\delta = \pi$ ($\delta_1 = \pi/2, \delta_2 = \pi/2$), and $T_{\rm F}^*$ is given by a value slightly lower than the Kondo temperature $T_{\rm K2}$, if Δ is much smaller than Δ^*. On the other hand, in the case of $\Delta > \Delta^*$, the CEF splitting (antiferromagnetic interaction between f-electrons in the model Hamiltonian, (3.11)) is so large compared to the energy gain related to the formation of K-Y singlet states that the CEF singlet becomes the ground state. In this case, the remaining conduction electrons are not scattered by f-electrons, and as a result the total phase shift is $\delta = 0$ ($\delta_1 = 0, \delta_2 = 0$). When $\Delta \gg \Delta^*$, $T_{\rm F}^*$ becomes close to the excitation energy K between two singlet states.

Such an interchange of the ground state can be understood by considering that the increase of Δ causes the stabilization of the level of the CEF singlet state as shown in Fig.3.5. In the case of $\Delta \sim \Delta^*$, $T_{\rm F}^*$ is determined not by characteristic energies of the K-Y singlet and the CEF singlet states, but by the energy splitting between two singlet states, ΔE: i.e., $T_{\rm F}^* \sim \Delta E$. Particularly, at the critical point, the degeneracy of the K-Y singlet and the CEF singlet states is not lifted even at $T = 0$, making $T_{\rm F}^* = 0$ and $\lim_{T\to 0} S_{\rm imp} = 0.5 \log 2$.

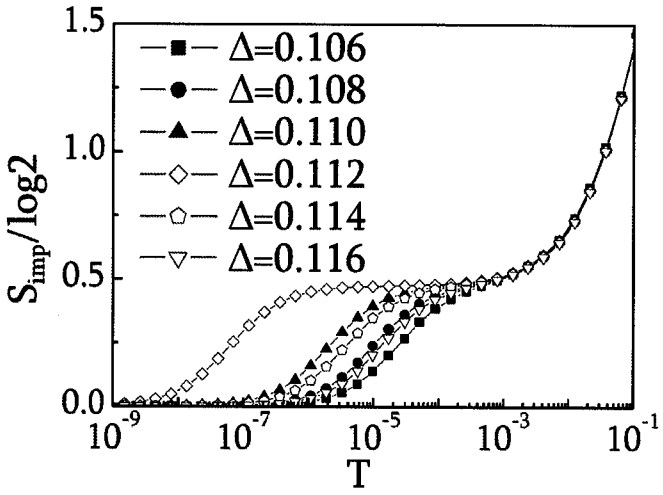

Figure 3.3: Temperature dependence of the entropy due to f-electrons in systems near the critical point. Parameter set is the same as that used in Fig.3.2. In order to obtain the result with a higher accuracy, 3000 states are kept in each step of NRG. Ground states of each system are indicated by open symbols for the K-Y singlet, and filled symbols for the CEF singlet. The characteristic temperature $T_{\rm F}^*$ is given by that making $\partial S_{\rm imp}(T)/\partial(\log T)$ maximum at the lower temperature side.

In other words, at low enough temperatures, the localized moment $\vec{S}_1$ of orbital 1 has already been screened out by conduction electrons in orbital 1 below $T_{\rm K1}$, while $\vec{S}_2$ of orbital 2 still has the degree of freedom as localized moment. Therefore, the effective Hamiltonian of (3.11) near the fixed point behaves as the two-channel Kondo model (TCKM) [10, 11] because $\vec{S}_2$ interacts with two "conduction" electron channels, one is the conduction electrons on orbital 2 and the other is a complex of conduction electrons on orbital 1 and screened $\vec{S}_1$ as discussed in ref. 10.

Fig.3.6 shows the Δ dependence of the Sommerfeld coefficient, $\gamma_{\rm imp}(T) \equiv C_{\rm imp}(T)/T$, due to f-electrons for various temperatures. For all Δ shown in Fig.3.6, $\gamma_{\rm imp}(T)$ increases monotonically down to $T = 7.0 \times 10^{-7}$ as decreasing T. At $\Delta = \Delta^* \simeq 0.112$, the increase of $\gamma_{\rm imp}(T)$ does not stop and exhibits divergence in the limit $T \to 0$ because the structure of the fixed point is the same as that of TCKM as discussed above. For Δ off the critical value Δ^*, the

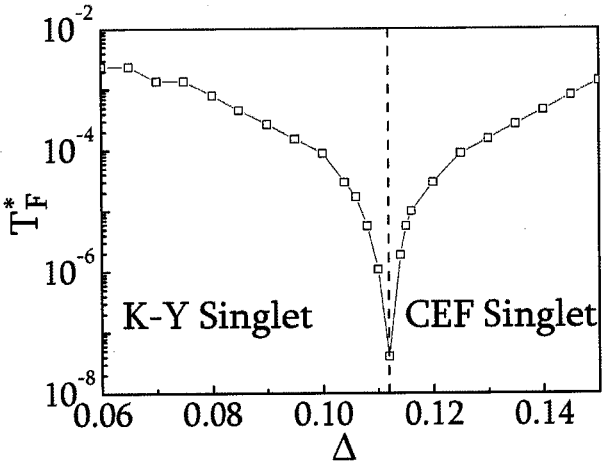

Figure 3.4: Δ dependence of $T_{\rm F}^*$. The effect of the competition between two singlet states suppresses $T_{\rm F}^*$, and in particular $T_{\rm F}^* = 0$ at the critical point $\Delta = 0.112 \simeq \Delta^*$.

increase of $\gamma_{\rm imp}(T)$ stops at around the characteristic temperature $T_{\rm F}^*$ leading to the Fermi liquid behavior at $T < T_{\rm F}^*$. $\gamma_{\rm imp}(T)$ takes a dip structure around $\Delta \sim \Delta^*$ at higher temperature region. This is because $S_{\rm imp}(T)$ has only a weak T dependence in a wide temperature range $0 \sim T_{\rm F}^* < T < T_{\rm K2}$ or Δ around $\Delta \simeq \Delta^*$ as can be seen in Fig.3.3.

It is remarked that the enhanced part of $\gamma_{\rm imp}(T)$ near $\Delta \sim \Delta^*$ in the low temperature limit from the background part at $|\Delta - \Delta^*| \gg \Delta^*$ arises from the effect of the competition between the K-Y singlet and the CEF singlet states. The part of the background is essentially given by an inverse of $T_{\rm K2}$ or Δ, and is overwhelmed by the enhanced part near $\Delta \sim \Delta^*$. Note that the ordinate of Fig.3.6 is represented in a logarithmic scale.

Although we take Δ as a control parameter here, we can expect a similar behavior of $\gamma_{\rm imp}$ through other parameters, such as the hybridizations V_1 and V_2, which can also control the competition between levels of two singlet states. It is also remarked that such an anomalous behavior of $\gamma_{\rm imp}$ can be realized in systems with other symmetry: e.g., in UBe_{13} with cubic symmetry [12, 13, 14]. Fig. 3.7 shows the Sommerfeld coefficient due to the f-electron, γ, and the lattice constant a_0 for system of solid solution, $U_{1-x}M_xBe_{13}$. Here, the lattice constant, a_0 is controlled by replacing the U atom partly with other elements M, and γ shows the similar behavior as shown in Fig. 3.6. It is remarkable

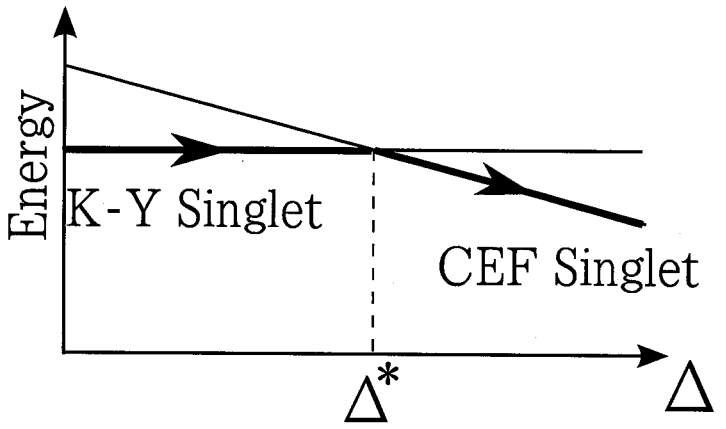

Figure 3.5: Schematic energy levels of two singlet ground states. The CEF singlet state is stabilized relative to the K-Y singlet state as Δ increases.

that γ takes a maximum value at $a_0 = a_0^*$, which is approximately the same as the lattice constant of UBe_{13} [15]. Experimentally, as shown in Fig. 3.8, in a series of materials with $a_0 < a_0^*$ such as $U_{0.1}Y_{0.9}Be_{13}$ and $U_{0.1}Sc_{0.9}Be_{13}$, the Kondo like upturn is observed in the resistivity in the low temperature region. On the other hand, in those with $a_0 > a_0^*$ such as $U_{0.1}La_{0.9}Be_{13}$ and $U_{0.1}Th_{0.9}Be_{13}$, the temperature dependence of the resistivity can be explained by the effect of the CEF with the singlet ground state. Then, we expect that UBe_{13} is located near the critical point in this series of materials.

3.4 Magnetic Field Dependence of Non-Fermi Liquid Behaviors

In this section, we discuss the magnetic field dependence of the NFL behavior of $\gamma_{\rm imp}(T)$. The effect of the magnetic field on f^1 states is taken into account through the Zeeman term for total angular moment, $\mathcal{H}_{\rm Zeeman}(f^1) = -g_J\mu_{\rm B}j_zH_z$, with $j = 5/2$ and $g_j = 6/7$. That on f^2 states arises from the diagonal (for $\Gamma_5^{(2)}$ doublet) and the off-diagonal (for Γ_3 and Γ_4 singlets) matrix elements of two-electron Zeeman term $\mathcal{H}_{\rm Zeeman}(f^2)$; e.g., $\langle\Gamma_{5\pm}^{(2)}|\mathcal{H}_{\rm Zeeman}(f^2)|\Gamma_{5\pm}^{(2)}\rangle = \mp 11 g_j\mu_{\rm B}H_z/7$, and $\langle\Gamma_3|\mathcal{H}_{\rm Zeeman}(f^2)|\Gamma_4\rangle = -2g_j\mu_{\rm B}H_z$. Here, $\mathcal{H}_{\rm Zeeman}(f^2)$ consists of two $\mathcal{H}_{\rm Zeeman}(f^1)$.

In Fig.3.9, we show the magnetic field dependence of the characteristic temperature $T_{\rm F}^*$ near the critical point; i.e., $\Delta = 0.108, 0.110, 0.112(\simeq \Delta^*), 0.114, 0.116$

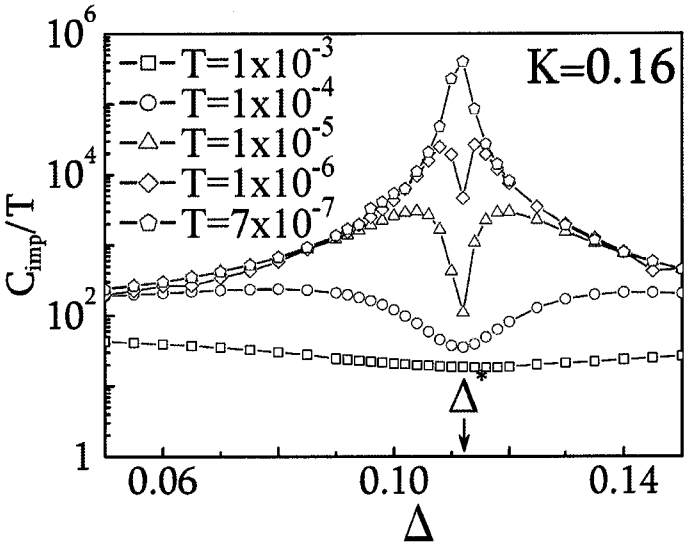

Figure 3.6: Δ dependence of the Sommerfeld coefficient $\gamma_{\rm imp}(T) \equiv C_{\rm imp}(T)/T$ due to the f-electrons for various temperature. The ground state switch at $\Delta = \Delta^* \simeq 0.112$ from the K-Y singlet ground state for $\Delta < \Delta^*$ to the CEF singlet for $\Delta > \Delta^*$.

and 0.118. It is noted that $T_{\rm F}^*(H_z)$ remains constant for H_z less than the characteristic magnetic field H_z^* which is defined approximately as that from which $T_{\rm F}^*(H_z)$ starts to increase as increasing H_z (as shown by circles in Fig.3.9). Explicitly, the characteristic magnetic field H_z^*'s are given as $H_z^* \simeq 3 \times 10^{-4}$ for $\Delta = 0.106$ and 0.118, $H_z^* \simeq 2 \times 10^{-4}$ for $\Delta = 0.108$ and 0.116, $H_z^* \simeq 3 \times 10^{-5}$ for $\Delta = 0.110$ and 0.114, and $H_z^* \simeq 1 \times 10^{-5}$ for $\Delta = 0.112$. H_z^* has a tendency of approaching zero as the critical fixed point is approached, i.e., $\Delta \to \Delta^*$. For CEF parameter Δ shown in Fig.3.9, H_z^* is much smaller than the lower Kondo temperature $T_{\rm K2} \simeq 6.01 \times 10^{-3}$, so that the magnetic field $H_z < H_z^*$ has little influence on the K-Y singlet state. Then, H_z^* is considered to be determined by a competition of two effects which destroy the TCKM-type NFL fixed point: one is a distance of Δ from Δ^* and the other is the magnetic field which breaks the degeneracy corresponding to $S_{\rm imp}(T = 0) = 0.5 \log 2$ due to the TCKE, the origin of the TCKM-type NFL fixed point. Namely, H_z^* is given by the energy scale characterizing a crossover from the TCKM-type NFL behavior to the polarized Fermi liquid behavior beyond the effect of the distance of Δ from the critical value Δ^*. Since $\gamma_{\rm imp}(T)$ exhibits the divergent increase around $\Delta \sim \Delta^*$

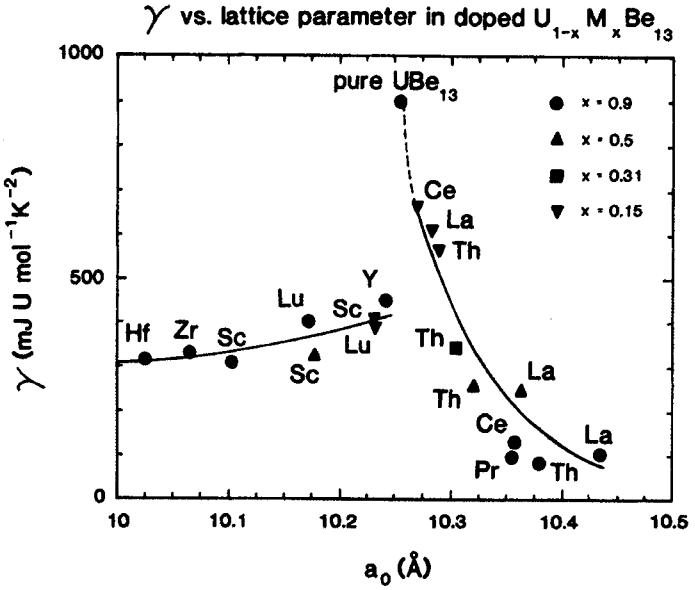

Figure 3.7: Lattice constant a_0 and the Sommerfeld coefficient γ of 18 $U_{1-x}M_xBe_{13}$ at $T \sim 0.5$[K] [15]. The γ value takes peak structure at $a_0 = a_0^*$ where a_0^* is the lattice constant of UBe_{13}.

in the temperature region $T > T_F^*(H_z)$ as decreasing T, $\gamma_{\rm imp}(T)$ exhibits a NFL behavior in the same temperature region $T > T_F^*(H_z)$. Since $T_F^*(H_z)$ remains almost unchanged up to $H_z = H_z^*$, the NFL behaviors are expected to remain robustly even under the magnetic field $H_z > T_F^*(H_z)$ so long as $H_z < T_{K2}$. This behavior is reproduced by explicit calculations of $\gamma_{\rm imp}(T)$ under various magnetic fields as shown below.

In Fig.3.10, we show the temperature dependence of $\gamma_{\rm imp}(T)$ for $\Delta = 0.112$ ($\simeq \Delta^*$) and $\Delta = 0.118$ under various magnetic fields of up to $H_z = 1.2 \times 10^{-3}$. Extremely close to the criticality at $\Delta = 0.112 \simeq \Delta^*$, $\gamma_{\rm imp}(T)$ is enhanced by the magnetic field as shown in Fig.3.10(a). This is because $T_F^*(H_z)$ increases appreciably from 10^{-7} to 10^{-5} corresponding to the increase of the magnetic field H_z from 10^{-4} to 10^{-3}, resulting in an increase of $\partial S_{\rm imp}(T)/\partial(\log T) = C_{\rm imp}(T)$, so $\gamma_{\rm imp}(T)$, at $T > 10^{-5}$. On the other hand, at $\Delta = 0.118$ slightly off the criticality, $\gamma_{\rm imp}(T)$ is robust against the magnetic field up to $H_z = 1.2 \times 10^{-3}$ for the temperature region $T > 3 \times 10^{-5}$ as shown in Fig.3.10(b). This is because $T_F^*(H_z)$ remains almost unchanged up to $H_z = H_z^* \sim 10^{-3}$ so that $\gamma_{\rm imp}(T)$ remains the same as that at $H_z = 0$ for $T > T_F^* \simeq 10^{-5}$.

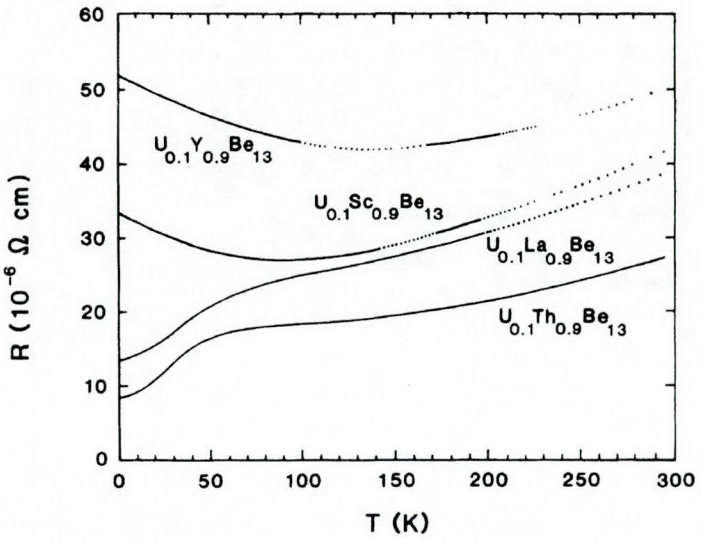

Figure 3.8: Temperature dependence of the resistivity for $U_{0.1}M_{0.9}Be_{13}$ where M=Th, La, Sc and Y [15]. Material with M=Y and Sc, which has smaller lattice constant than UBe_{13} show the Kondo like upturn in the low temperature region, while materials with M=La and Th, which has larger lattice constant than UBe_{13} shows the resistivity which can be explained by the effect of the CEF with the singlet ground state.

These kinds of NFL behaviors arise also in the region of the K-Y singlet state, i.e., $\Delta < \Delta^*$, although we do not show the results explicitly.

3.5 Kondo-Temperature Dependence of Non-Fermi Liquid Behavior under Magnetic Field

In this section, we investigate the properties of the NFL behavior of $\gamma_{\rm imp}(T)$ under magnetic field of systems with other $T_{\rm K2}$ by changing V_2 as $V_2 = 0.25$ and 0.20 for various sets of the CEF parameter, (K, Δ). Other parameters are set to be the same as those in the previous section: i.e., $E_{f1} = E_{f2} = -0.4, U_1 = U_2 = 1.0$, and $V_1 = 0.45$. In the case of $K = \Delta = 0$, each lower Kondo temperature can also be determined by the Wilson's definition as $T_{\rm K2} = 1.27 \times 10^{-3}$ for $V_2 = 0.25$ and $T_{\rm K2} = 8.92 \times 10^{-5}$ for $V_2 = 0.20$, respectively. To analyze further, we also fix one of the CEF parameters as $K = 0.16$ and calculate $\gamma_{\rm imp}(T)$ for a series of Δ under various magnetic

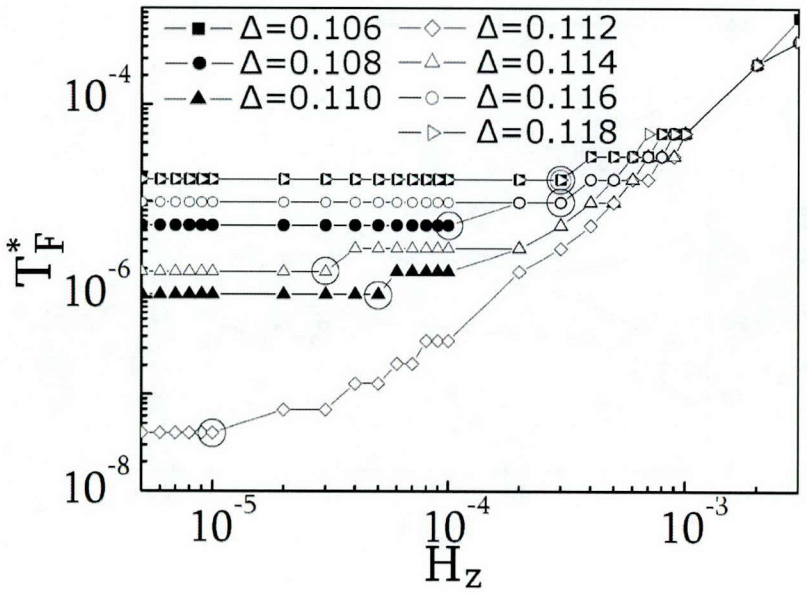

Figure 3.9: Magnetic field dependence of $T_{\rm F}^*$ near the critical point. The parameters related to f-electrons are the same as Fig.3.2. Circles indicate characteristic magnetic fields Hz^*'s.

fields. It is natural that Δ^* (corresponding to the critical point) becomes small with decreasing $T_{\rm K2}$ because the energy gain due to the formation of the K-Y singlet state decreases with a smaller V_2. The critical value of Δ is determined as $\Delta^* \simeq 0.054$ for $V_2 = 0.25$ and $\Delta^* \simeq 0.024$ for $V_2 = 0.20$, respectively. Fig.3.11 shows the temperature dependence of $\gamma_{\rm imp}(T)$ of the system with the CEF ground state: (a) $\Delta = 0.062 > \Delta^* \simeq 0.054$ for $V_2 = 0.25$ and (b) $\Delta = 0.032 > \Delta^* \simeq 0.024$ for $V_2 = 0.20$. The NFL behavior being robust against the magnetic field occurs in a temperature region of $T > T_{\rm F}^*$ up to $H_z \simeq H_z^*$ in the former case (a), while in the latter case (b) the magnetic field has considerable influence on the NFL behavior.

For $H_z = 0$, $T_{\rm F}^*$ is also suppressed as in the case of $V_2 = 0.30$ in the vicinity of the critical point $\Delta \sim \Delta^*$. It is noted that the decrease of $T_{\rm K2}$ and Δ does not appreciably affect $T_{\rm F}^*$, i.e. $T_{\rm F}^* \sim 10^{-5}$ for both cases of (a) and (b), which is determined from calculations corresponding to Fig.3.3. This is because $T_{\rm F}^*$ is determined by the energy splitting between the K-Y singlet and the CEF singlet states, and does not depend on the characteristic energy scale of each singlet state. Under the magnetic field, the effect on the NFL behavior is

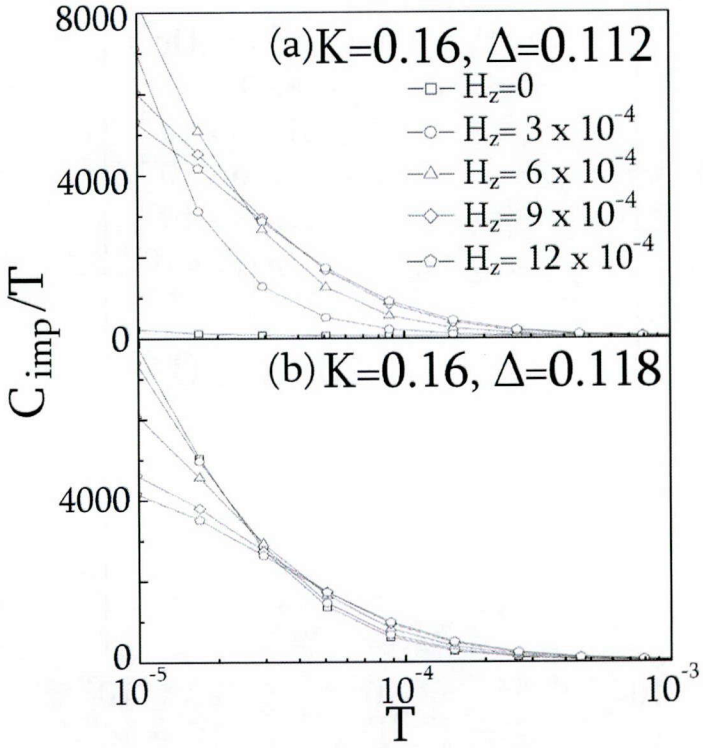

Figure 3.10: Temperature dependence of γ for (a) $\Delta = 0.112$ ($\simeq \Delta^*$) and (b) $\Delta = 0.118$ under various magnetic fields. In the case of (b), the NFL behavior of γ is robust against a magnetic field of up to $H_z = 1.2 \times 10^{-3}$ for $T > 3.0 \times 10^{-5}$ in spite of $T_{\rm F}^* \simeq 1.69 \times 10^{-5}$. The parameters related to f-electrons are the same as those used in Fig.3.2.

markedly different in two cases (a) and (b). In the case of (a) with $V_2 = 0.25$, the NFL behavior of $\gamma_{\rm imp}(T)$ is rather robust against the magnetic field (up to H_z^*) in a wide temperature range ($T > T_{\rm F}^*$) as in the case of $V_2 = 0.30$, while in the case of (b) with $V_2 = 0.20$, $\gamma_{\rm imp}(T)$ is sensitive to the magnetic field because the characteristic magnetic field H_z^* is comparable to the lower Kondo temperature, $T_{\rm K2}$. Namely, in the case of $V_2 = 0.20$, the magnetic field $H_z > T_{\rm K2} \simeq 8.92 \times 10^{-5}$ suppresses $\gamma_{\rm imp}(T)$ by breaking the K-Y singlet ground state. It is noted that in the case $T_{\rm K2} > \Delta$, the suppression of $\gamma_{\rm imp}(T)$ as in the case of Fig.3.10(b) is expected for $H_z > \Delta$ by breaking the CEF singlet states. Thus, the magnetic field dependence of the NFL behavior of $\gamma_{\rm imp}(T)$ is

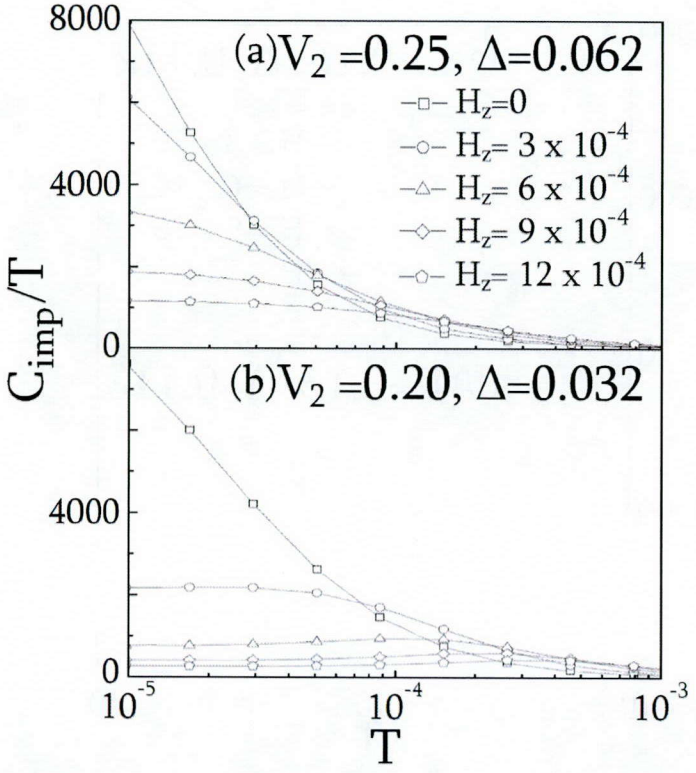

Figure 3.11: Temperature dependence of $\gamma_{\rm imp}(T)$ for a series of magnetic fields in the system for the hybridization (a)$V_2 = 0.25$ and (b)$V_2 = 0.20$.

determined not by the characteristic temperature $T_{\rm F}^*$, but by the characteristic magnetic field H_z^* which is determined by the characteristic energy scale of each singlet state, $T_{\rm K2}$ and Δ, or the distance from the critical point.

3.6 Conclusion and Discussion

We have investigated the effect of the magnetic field on the NFL behaviors due to the competition between the K-Y singlet and the CEF singlet states in f^2-based heavy fermion systems with tetragonal symmetry. The effect of the competition suppresses the characteristic temperature $T_{\rm F}^*$, corresponding to a peak of the specific heat, $C_{\rm imp}(T)$, to a much smaller value than the characteristic energy scale of each singlet states: i.e., $T_{\rm K2}$, the lower Kondo

temperature, and Δ, the energy splitting between the CEF singlet ground state and the first excited doublet states. $T_{\rm F}^*$ is determined approximately by ΔE, the energy difference between two singlet states, and there exists the two-channel Kondo model (TCKM) type NFL behaviors at $T_{\rm F}^* < T < T_{\rm K2}$. Namely, near the critical point, $\Delta \sim \Delta^*$, the Sommerfeld coefficient $\gamma_{\rm imp}(T)$ exhibits a NFL behavior ($\gamma_{\rm imp}(T) \propto -\log T$) at $T > T_{\rm F}^*$.

In the vicinity of the critical point, $T_{\rm F}^*$ was shown not to be affected by the magnetic field up to a certain value H_z^*, while $T_{\rm F}^*$ is increased for $H_z^* < H_z < \min(T_{\rm K2}, \Delta)$. As a result, the NFL behavior of $\gamma_{\rm imp}$ at $T > T_{\rm F}^*$ is robust against the magnetic field $H < H_z^*$. Then, for reasonable sets of parameters, the NFL behaviors being robust against a magnetic field of up to H_z^* can occur at an observable temperature range. Thus, the magnetic field dependence of this NFL is characterized by H_z^* which is determined by the characteristic energy scales of two singlet states and the distance from the critical point.

In the present chapter, we have discussed physical properties in the tetragonal symmetry. However, also in the case of other crystal symmetries, it is expected that there remains the effect of the competition between the K-Y singlet and the CEF singlet states, leading to the NFL behaviors similar to the present case. One example would be the case of the cubic system UBe_{13} which seems to be located near the phase boundary between the K-Y singlet and the CEF singlet states, according to a series of experiments of $\lim_{T\sim 0} C(T)/T$ for systems of solid solution, $U_{1-x}T_xBe_{13}$ shown in Fig. 3.7, where the lattice constant a_0 is changed in a wide range covering both the K-Y singlet and the CEF singlet ground states [15]. Moreover, pure UBe_{13} exhibits the NFL behavior, $C(T)/T \sim -\log T$ up to $H_z = 12$ Tesla as shown in Fig. 3.12 [14]. Of course, precisely speaking, results of the present chapter are for the system of f^2-impurity so that we should be careful in deriving a solid conclusion. Indeed, an approach based on the dynamical mean field concept is indispensable for deriving a solid conclusion for lattice systems, in which the present results would be inherited to the solver of impurity problem. Nevertheless, we expect that the effect of the competition plays an important role for UBe_{13} to exhibit such a NFL behavior rather robust against the magnetic field larger than the effective Fermi energy inferred from the value of $\lim_{T\sim 0} C(T)/T$. Namely, the lower Kondo temperature would be larger than 12K from the fact that the NFL behavior $\lim_{T\sim 0} C(T)/T \sim -\log T$ in UBe_{13} is robust against the magnetic field up to 12 Tesla at least [14]. Were it not for the superconducting state at $T < T_{\rm c} \simeq 1$K, there would exist the peak with specific heat near at $T = T_{\rm F}^*$. Predictions of the present chapter may be checked by experiments in some U-diluted system of UBe_{13} near the phase boundary between the K-Y

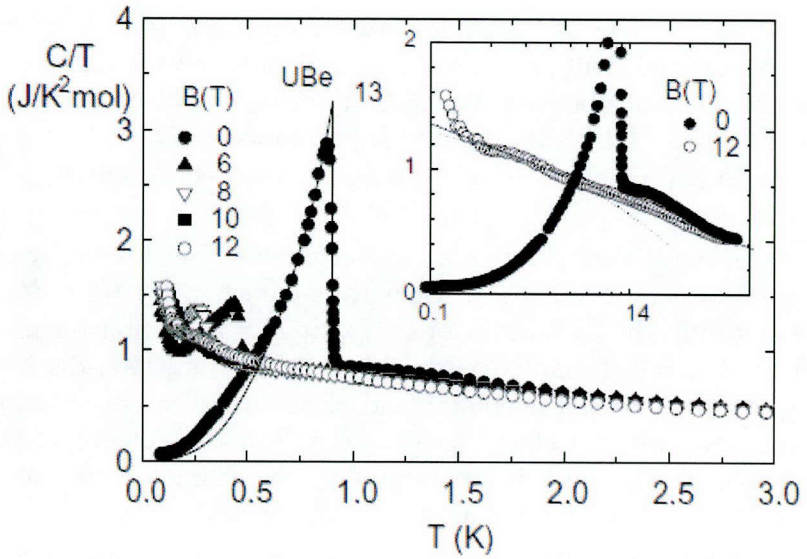

Figure 3.12: Temperature dependence of the Sommerfeld coefficient of UBe_{13} after subtraction from raw data the nuclear contribution due to Zeeman splitting of ^{9}Be states [14] at some magnetic field, B =0, 6, 8, 10, 12 Tesla. The sharp peak at $T \sim 0.9$ at $B = 0$Tesla is due to the superconducting transition. Inset shows 0 and 12 Tesla's data on a logarithmic temperature scale. The Sommerfeld coefficient of UBe_{13} shows -log T behavior at $B = 0$ Tesla, and that is not affected by magnetic field up to 12 Tesla.

singlet and the CEF singlet states under pressures and/or magnetic fields.

Appendix: f^2 States in Tetragonal Symmetry

In the tetragonal symmetry, wave functions for each CEF level are given within f^1 states of $j = 5/2$ orbitals as follows:

$$|\Gamma_{7,\pm}^{(1)}\rangle = \zeta|\pm\frac{5}{2}\rangle + \eta|\mp\frac{3}{2}\rangle, \tag{3.1}$$

$$|\Gamma_{7,\pm}^{(2)}\rangle = \pm\eta|\pm\frac{5}{2}\rangle \mp \zeta|\mp\frac{3}{2}\rangle, \tag{3.2}$$

$$|\Gamma_{6,\pm}\rangle = |\pm\frac{1}{2}\rangle, \tag{3.3}$$

where ζ and η are the coefficients determined by the effect of the CEF. In this appendix, we determine these coefficients on the basis of the condition that

the energy level of low-lying f^2 states with $J = 4$ manifold can be reproduced by Hamiltonian (3.9). First, we construct states with $J = 4$ manifold from the direct product of states with $j = 5/2$ manifold.

$$|\pm 3\rangle = \pm|\pm\frac{5}{2}\rangle|\pm\frac{1}{2}\rangle, \tag{3.4}$$

$$|\pm 2\rangle = \pm\frac{3}{\sqrt{14}}|\pm\frac{5}{2}\rangle|\mp\frac{1}{2}\rangle \pm \sqrt{\frac{5}{14}}|\pm\frac{3}{2}\rangle|\pm\frac{1}{2}\rangle, \tag{3.5}$$

$$|\pm 1\rangle = \pm\sqrt{\frac{2}{7}}|\pm\frac{5}{2}\rangle|\mp\frac{3}{2}\rangle \pm \sqrt{\frac{5}{7}}|\pm\frac{1}{2}\rangle|\mp\frac{3}{2}\rangle. \tag{3.6}$$

By using the inversion relation of eqs.(3.1)-(3.3) representing $|\pm 5/2\rangle$, $|\pm 3/2\rangle$, and $|\pm 1/2\rangle$ in terms of $\Gamma_7^{(1)}$, $\Gamma_7^{(2)}$, and Γ_6, we obtain the f^2 states in the tetragonal symmetry as follows:

$$\begin{aligned}|\Gamma_4\rangle = \frac{1}{\sqrt{2}}(|2\rangle - |-2\rangle) = \frac{1}{2\sqrt{7}}\Big[&\left(3\zeta + \sqrt{5}\eta\right)\left(|\Gamma_{7+}^{(1)}\rangle|\Gamma_{6-}\rangle + |\Gamma_{7-}^{(1)}\rangle|\Gamma_{6+}\rangle\right) \\ &+ \left(\sqrt{5}\zeta - 3\eta\right)\left(|\Gamma_{7-}^{(2)}\rangle|\Gamma_{6+}\rangle - |\Gamma_{7+}^{(2)}\rangle|\Gamma_{6-}\rangle\right)\Big],\end{aligned} \tag{3.7}$$

$$\begin{aligned}|\Gamma_3\rangle = \frac{1}{\sqrt{2}}(|2\rangle + |-2\rangle) = \frac{1}{2\sqrt{7}}\Big[&\left(3\zeta - \sqrt{5}\eta\right)\left(|\Gamma_{7+}^{(1)}\rangle|\Gamma_{6-}\rangle - |\Gamma_{7-}^{(1)}\rangle|\Gamma_{6+}\rangle\right) \\ &+ \left(\sqrt{5}\zeta + 3\eta\right)\left(|\Gamma_{7+}^{(2)}\rangle|\Gamma_{6-}\rangle + |\Gamma_{7-}^{(2)}\rangle|\Gamma_{6+}\rangle\right)\Big],\end{aligned} \tag{3.8}$$

$$\begin{aligned}|\Gamma_{5,+}^{(2)}\rangle = \beta|3\rangle - \alpha|-1\rangle = &\left(\beta\zeta + \sqrt{\frac{5}{7}}\alpha\eta\right)|\Gamma_{7+}^{(1)}\rangle|\Gamma_{6+}\rangle + \sqrt{\frac{2}{7}}\alpha|\Gamma_{7-}^{(1)}\rangle|\Gamma_{7-}^{(2)}\rangle \\ &+ \left(\beta\eta - \sqrt{\frac{5}{7}}\alpha\zeta\right)|\Gamma_{7+}^{(2)}\rangle|\Gamma_{6+}\rangle,\end{aligned} \tag{3.9}$$

$$\begin{aligned}|\Gamma_{5,-}^{(2)}\rangle = \beta|-3\rangle - \alpha|1\rangle = &-\left(\beta\zeta + \sqrt{\frac{5}{7}}\alpha\eta\right)|\Gamma_{7-}^{(1)}\rangle|\Gamma_{6-}\rangle + \sqrt{\frac{2}{7}}\alpha|\Gamma_{7+}^{(1)}\rangle|\Gamma_{7+}^{(2)}\rangle \\ &+ \left(\beta\eta - \sqrt{\frac{5}{7}}\alpha\zeta\right)|\Gamma_{7-}^{(2)}\rangle|\Gamma_{6-}\rangle,\end{aligned} \tag{3.10}$$

are the same as those expressed in eqs. (3.5)-(3.8).

Here, terms where states with $\Gamma_7^{(1)}$ symmetry are occupied in eqs.(3.7)-(3.10) can be negligible because their energy levels are assumed to be higher than the other states so that the hybridization between $\Gamma_7^{(1)}$ and the f^2-states (3.7)-(3.10) may be neglected for forming a heavy fermion state as discussed in

refs. 16 and 17. The coefficients, ζ and η, can be determined by the condition that the coefficients of the remaining terms in eqs.(3.7)-(3.8) are equal to those in eqs.(3.5)-(3.6). The result is

$$\zeta = \sqrt{\frac{5}{14}}, \qquad \eta = \frac{3}{\sqrt{14}}. \tag{3.11}$$

A relation between α and β is also derived by comparing eqs.(3.9)-(3.10) with eqs.(3.7)-(3.8) as follows:

$$\beta\frac{3}{\sqrt{14}} - \sqrt{\frac{5}{7}}\alpha\sqrt{\frac{5}{14}} = x. \tag{3.12}$$

It is noted that the coefficient of the first term in (3.7), including $\Gamma_{7\pm}^{(1)}$, becomes larger than that of the second term in (3.7), including $\Gamma_{7\pm}^{(2)}$, if we use the values of (3.11). However, it is allowable to discard the first term because the $\Gamma_{7\pm}^{(1)}$ state is assumed to play a negligible role in forming the heavy fermion state as discussed above. The normalization condition for the right part of eqs.(3.9)-(3.10) requires $x = 1$. Nevertheless, by combining the normalization condition for $\Gamma_5^{(2)}$ symmetry in f^2 states, i.e., $|\alpha|^2 + |\beta|^2 = 1$, there are no solutions for these coefficients as far as $2\sqrt{11}/7 < x \leq 1$ ($2\sqrt{11}/7 \simeq 0.947\cdots$). This is because we have discarded the states relating to $\Gamma_7^{(1)}$ as discussed above, and increased the weight of the remaining terms in eqs.(3.9)-(3.10). In view of such a situation, for simplicity, we use the pseudospin representations, $|\uparrow,\uparrow\rangle$ and $|\downarrow,\downarrow\rangle$, written in eqs.(3.7)-(3.8), respectively, as $\Gamma_5^{(2)}$ states instead of using α and β.

Bibliography of Chapter 3

[1] H. Löhneysen, A. Rosch, M. Vojta, and P. Wölfle: Rev. Mod. Phys. **79** (2007) 1015.

[2] M. Imada, A. Fujimori, and Y. Tokura: Rev. Mod. Phys. **70** (1998) 1039.

[3] D. L. Cox: Phys. Rev. Lett **59** (1987) 1240.

[4] D. L. Cox and A. Zawadowski: Adv. Phys. **47** (1998) 599: and references therein.

[5] S. Yotsuhashi, K. Miyake and H. Kusunose: J. Phys. Soc. Jpn. **71** (2002) 389.

[6] K. Hattori and K. Miyake: J. Phys. Soc. Jpn **74** (2005) 2193.

[7] T. Kawae, T. Yamamoto, K. Yurue, N. Tateiwa, K. Takeda, and T. Kitai: J. Phys. Soc. Jpn. **72** (2003) 2141.

[8] K. G. Wilson: Rev. Mod. Phys. **47** (1975) 773.

[9] H. R. Krishna-murthy, J. W. Wilkins and K. G. Wilson: Phys. Rev. B **21** (1980) 1003.

[10] D. M. Cragg, P. Lloyd and P. Nozières: J. Phys. C **13** (1980) 803.

[11] H. B. Pang and D. L. Cox: Phys. Rev. B **44** (1991) 9454.

[12] H. R. Ott, H. Rudigier, Z. Fisk and J. L. Smith: Phys. Rev. Lett. **50** (1983) 1595.

[13] H. R. Ott, H. Rudigier, E. Felder, Z. Fisk and J. L. Smith: Phys. Rev. B **33** (1986) 126.

[14] P. Gegenwart, C. Langhammer, R. Helfrich, N. Oeschler, M. Land, J. S. Kim, G. R. Stewart, and F. Steglich: Physica. C **408-410** (2004) 157-160.

[15] J. S. Kim, B. Andraka, C. S. Jee, S. B. Roy, and G. R. Stewart: Phys. Rev. B **41** (1990) 11073.

[16] H. Kusunose and H. Ikeda: J. Phys. Soc. Jpn **74** (2005) 405.

[17] H. Ikeda and K. Miyake: J. Phys. Soc. Jpn **66** (1997) 3714.

Chapter 4

Effect of Competition between Kondo-Yosida and Crystalline-Electric-Field Singlet States in f^2-Configuration System with Tetragonal Symmetry

4.1 Introduction

In recent decades, non-Fermi-liquid (NFL) behaviors observed in some heavy fermion compounds and high-T_c cuprates have created interest in the issues around the quantum-critical point (QCP). Of these NFL behaviors, those based on a single correlated impurity in systems with f^2-configuration are classified into two subclasses in which the QCP is triggered by the local criticality: one is caused by the two-channel Kondo (TCK) effect due to the non-Kramers doublet state [1, 2, 3, 4, 5, 6, 7, 8, 9], and the other is caused by the competition between the crystalline-electric field (CEF) singlet and the Kondo-Yosida (K-Y) singlet states [10, 11, 12, 13]. Each of these mechanisms shows NFL behaviors below its characteristic energy scale T_x because the systems flow toward the unstable fixed point. However, in real systems, small but relevant perturbations, leading the systems away from the unstable fixed point, give rise to a finite characteristic temperature T_F^*, the crossover temperature from NFL behavior to Fermi-liquid behavior. Namely, these two NFL behaviors are

observed in the temperature (T) region $T_{\rm F}^* \leq T \leq T_x$ when $T_{\rm F}^* \ll T_x$.

The NFL behaviors due to these two mechanisms are, in general, difficult to distinguish experimentally, especially in the case of U-impurity compounds, because there exists some ambiguity in determining the CEF level scheme of U-ions. $Th_{1-x}U_xRu_2Si_2$ (x$\leq$0.07) is one such complicated heavy fermion impurity system. The NFL behaviors of this material are well scaled by impurity concentrations, so that many theoretical and experimental works have been carried out based on these two mechanisms treating U-ion as an impurity [5, 10, 11, 14, 15, 16]. Actually, in $Th_{1-x}U_xRu_2Si_2$, $-\ln T$ divergences are observed in both the magnetic susceptibility $\chi_{\rm imp}$ and the Sommerfeld coefficient $\gamma_{\rm imp} \equiv C_{\rm imp}/T$ as shown in Fig. 4.1 (a) and (b), $C_{\rm imp}$ being the specific heat due to the impurity. Moreover, the resistivity $\rho_{\rm imp}$ shows the anomalous temperature dependence as shown in Fig. 4.2. These NFL behaviors are consistent with those predicted by theories based on these two mechanisms. In the case of $R_{1-x}U_xRu_2Si_2$ (R=Y and La), degrees of NFL behaviors are less prominent. Namely, Fermi liquid behaviors recover in the low temperature regions where $Th_{1-x}U_xRu_2Si_2$ exhibits prominent NFL behaviors [16, 17]. These differences can be understood from a viewpoint that distances from the QCP are different from compounds to compounds. In other words, $Th_{1-x}U_xRu_2Si_2$ is assumed to be accidentally located near the QCP.

With the application of a magnetic field, however, there exist some aspects inconsistent with the NFL behaviors based on the TCK effect even in the case of $Th_{1-x}U_xRu_2Si_2$. First, if the NFL behaviors originated from the TCK effect, the magnetic field would induce the increase of $\gamma_{\rm imp}$ due to the release of the residual entropy by lifting the degeneracy due to the doublet $\Gamma_5^{(2)}$ ground state of $J = 4$ orbitals in tetragonal symmetry. However, the suppression of the $-\log T$ divergence of $\gamma_{\rm imp}$ is observed in $Th_{1-x}U_xRu_2Si_2$ by applying a magnetic field as shown in Fig. 4.2 [16]. Next, it was reported that $T_{\rm F}^*(H)$ of $Th_{1-x}U_xRu_2Si_2$ shows an anomalous magnetic field (H) dependence. Fig. 4.4 (a) shows the temperature dependence of the resistivity (ρ_{5f}) under the magnetic field, and Fig. 4.4 (b) shows the magnetic field dependence of the characteristic temperature (defined by $T_{\rm F}(H)$ in this figure) determined by the temperature at which the resistivity starts to shows the Fermi-liquid behavior, i.e., $\rho_{5f} \propto T^2$. Clearly seen from Fig 4.4 (c), which shows the H^2-dependence of $T_{\rm F}(H)$, the magnetic field dependence of $T_{\rm F}(H)$ does not written in the form a quadratic dependence of H expected in the TCK model [2, 4, 7, 8]. Considering these inconsistencies, it is troublesome to argue that the NFL behaviors in $Th_{1-x}U_xRu_2Si_2$ can be understood by the theory based on the TCK effect [11].

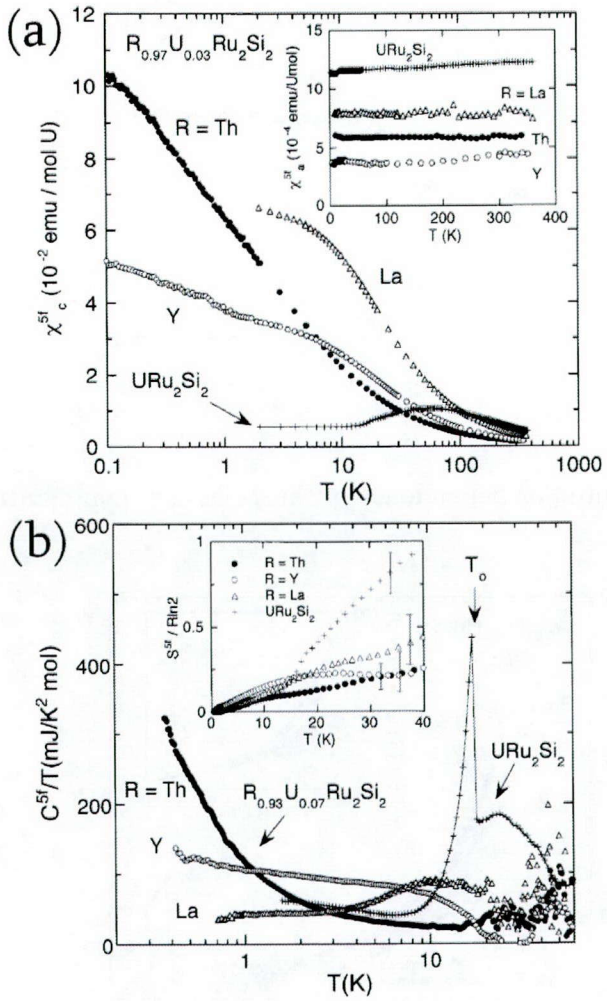

Figure 4.1: Temperature (T) dependence of (a) magnetic susceptibility (χ^{5f}) and (b) Sommerfeld coefficient (C^{5f}/T) due to f-electrons[16]. In the case of $Th_{1-x}U_xRu_2Si_2$, both shows logarithmic divergence as T decreases.

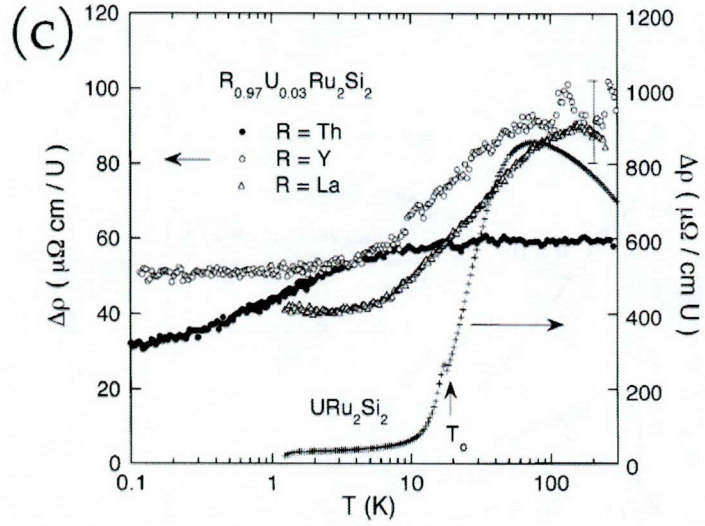

Figure 4.2: Temperature (T) dependence of the f-electron contribution to the resistivity ($\Delta\rho$) [16].

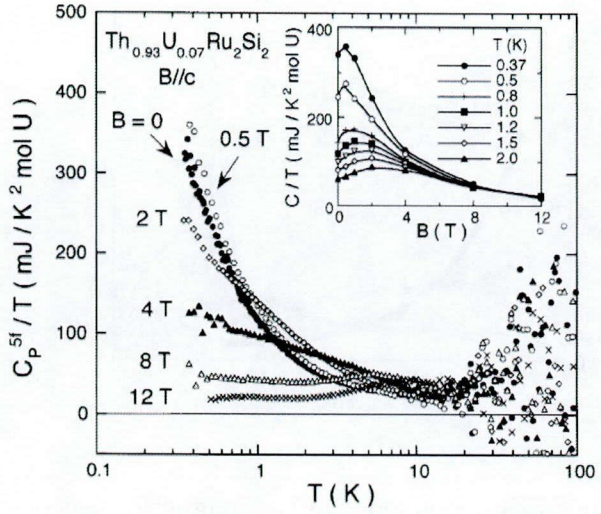

Figure 4.3: Temperature (T) dependence of the Sommerfeld coefficient due to the f-electron under magnetic field (B) [16].

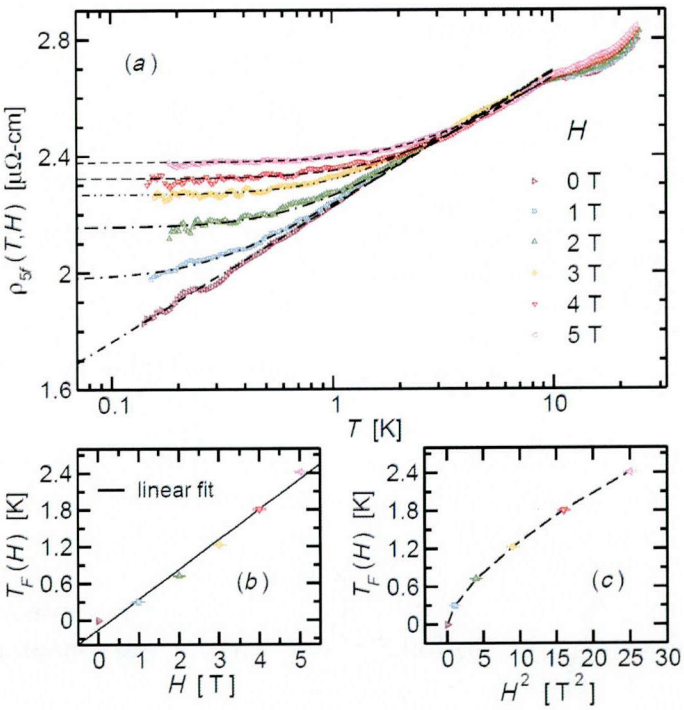

Figure 4.4: (a) Temperature (T) dependence of the characteristic temperature ($T_{\rm F}(H)$) under the magnetic field H. (b) H dependence and (c) H^2 dependence of $T_{\rm F}(H)$.

In this chapter, we study the magnetic field dependence of the NFL behaviors due to the competition between the K-Y singlet and the CEF singlet states in tetragonal symmetry, and discuss its applicability to the magnetic properties in $Th_{1-x}U_xRu_2Si_2$. Yotsuhashi *et al* have already discussed this problem on the basis of the two-orbital Anderson model with the "antiferromagnetic" Hund's-rule coupling [11], the same as in the present chapter. They have shown that the logarithmic enhancement of $\gamma_{\rm imp}$ due to the competition between the two singlet states is suppressed by applying the magnetic field in a wide set of parameters near the unstable fixed point, which is consistent with the experimental results of $Th_{1-x}U_xRu_2Si_2$ in a wide-temperature region. Here, we also take the same CEF scheme as [11], and investigate the H-dependence of the magnetic susceptibility $\chi_{\rm imp}$, the resistivity $\rho_{\rm imp}$, and, in particular, the characteristic temperature $T_{\rm F}^*(H)$ obtained from these physical quantities. On

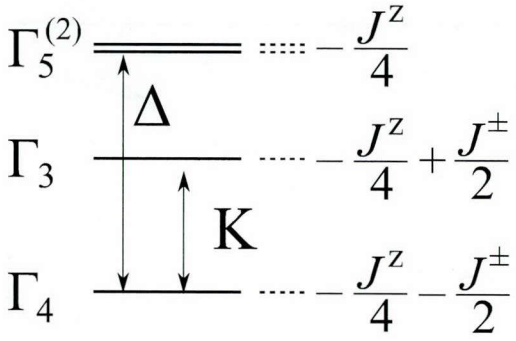

Figure 4.5: CEF level scheme of low-lying f^2 states and their eigenstates.

the basis of the Wilson numerical renormalization group (NRG) method [19], we show that the H-dependence of $T_{\rm F}^*(H)$ changes at around the crossover magnetic field $H_{\rm cr}$, and that $T_{\rm F}^*(H)$ at $H \sim H_{\rm cr}$ reproduces the anomalous behavior observed in $Th_{1-x}U_xRu_2Si_2$. Namely, the anomalous properties in $Th_{1-x}U_xRu_2Si_2$ can be fully explained by the present model. Moreover, the anomalous properties in $R_{1-x}U_xRu_2Si_2$ (R=Y and La) are also consistent with our results.

This chapter is organized as follows. In §4.2, we introduce the model Hamiltonian to discuss the competition between the two singlet states. In §4.3, the numerical result by the NRG calculation of the magnetic field effect on $T_{\rm F}^*(H)$, the resistivity $\rho_{\rm imp}$, and the magnetic susceptibility $\chi_{\rm imp}$, are given in the case of both singlet ground states. In §4.5, the H-dependence of $T_{\rm F}^*(H)$ is given in the case of the another f^2-CEF level scheme. In §4.4, we discuss a scaling property of the H-dependence of $T_{\rm F}^*(H)$ and its origin on the basis of the similarity of the unstable fixed point with the case of TCK effect. In §4.6, we discuss the applicability of this scenario to the experimental result of $Th_{1-x}U_xRu_2Si_2$, and we summarize our results in §4.7.

4.2 Model Hamiltonian

To discuss the competition between the two singlet states, we rewrite f^2-states in the j-j coupling scheme using f^1-states in the $j = 5/2$ manifold. Here, we restrict the Hilbert space of f^1-states to two low lying Kramers pairs and allot

them the pseudospin states as follows [11, 13]:

$$|\Gamma_{7\perp}^{(2)}\rangle = \frac{3}{\sqrt{14}}|+\frac{5}{2}\rangle - \sqrt{\frac{5}{14}}|-\frac{3}{2}\rangle \equiv |\uparrow,0\rangle, \tag{4.1}$$

$$|\Gamma_{7-}^{(2)}\rangle = -\frac{3}{\sqrt{14}}|-\frac{5}{2}\rangle + \sqrt{\frac{5}{14}}|+\frac{3}{2}\rangle \equiv |\downarrow,0\rangle, \tag{4.2}$$

$$|\Gamma_{6,+}\rangle = |+\frac{1}{2}\rangle \equiv |0,\uparrow\rangle, \tag{4.3}$$

$$|\Gamma_{6,-}\rangle = |-\frac{1}{2}\rangle \equiv |0.\downarrow\rangle. \tag{4.4}$$

The f^2-states are also restricted to the four low-lying CEF states in the $J = 4$ manifold of tetragonal symmetry, which are written in the j-j coupling scheme within a manifold of $j = 5/2$ in f^1-configuration as follows [11, 13]:

$$|\Gamma_4\rangle = \frac{1}{\sqrt{2}}\left(|+2\rangle - |-2\rangle\right) = \frac{1}{\sqrt{2}}\left(|\downarrow,\uparrow\rangle - |\uparrow,\downarrow\rangle\right), \tag{4.5}$$

$$|\Gamma_3\rangle = \frac{1}{\sqrt{2}}\left(|+2\rangle + |-2\rangle\right) = \frac{1}{\sqrt{2}}\left(|\uparrow,\downarrow\rangle + |\downarrow,\uparrow\rangle\right). \tag{4.6}$$

$$|\Gamma_{5,+}^{(2)}\rangle = \beta|+3\rangle - \alpha|-1\rangle = |\uparrow,\uparrow\rangle, \tag{4.7}$$

$$|\Gamma_{5,-}^{(2)}\rangle = \beta|-3\rangle - \alpha|+1\rangle = |\downarrow,\downarrow\rangle. \tag{4.8}$$

Here, we assume the Γ_4 singlet ground state as shown in Fig. 4.5, where K and Δ represent the excitation energies. With the use of the pseudospin states (4.1)-(4.4), the f^2-level scheme is reproduced by the "antiferromagnetic" Hund's-rule coupling [11, 13],

$$\mathcal{H}_{\text{Hund}} = \frac{J_\perp}{2}\left[S_1^+ S_2^- + S_1^- S_2^+\right] + J_z S_1^z S_2^z, \tag{4.9}$$

where coupling constants are defined as $J_\perp = K$ and $J_z = 2\Delta - K$, respectively. $\vec{S}_m$ is a pseudospin operator of the f-electron in the Hilbert space of f^1-state spanned by the orbitals $m = 1$ ($\Gamma_7^{(2)}$) or 2 (Γ_6), and is defined as

$$\vec{S}_m \equiv \frac{1}{2} f_{m\sigma}^\dagger \vec{\sigma}_{\sigma,\sigma'} f_{m\sigma'}, \tag{4.10}$$

where $f_{m\sigma}$ is an annihilation operator of the f-electron in orbital m [11, 13]. The use of the j-j coupling scheme for f^2-states is not necessary in principle for solving the present problem. However, it makes the problem more tractable in calculations on the basis of the Wilson NRG method.

Thus, the Hamiltonian is given by the two-orbital impurity Anderson model with the "antiferromagnetic" Hund's-rule coupling as follows [11, 13]:

$$\mathcal{H} = \mathcal{H}_{\rm c} + \mathcal{H}_{\rm hyb} + \mathcal{H}_{\rm f} + \mathcal{H}_{\rm Hund}, \tag{4.11}$$

$$\mathcal{H}_{\rm c} = \sum_{m=1,2} \sum_{\vec{k}\sigma} \varepsilon_{\vec{k}} c^{\dagger}_{\vec{k}m\sigma} c_{\vec{k}m\sigma}, \tag{4.12}$$

$$\mathcal{H}_{\rm hyb} = \sum_{m=1,2} \sum_{\vec{k}\sigma} \left(V_m c^{\dagger}_{\vec{k}m\sigma} f_{m\sigma} + {\rm h.c.} \right), \tag{4.13}$$

$$\mathcal{H}_{\rm f} = \sum_{m\sigma} E_{fm} f^{\dagger}_{m\sigma} f_{m\sigma} + \sum_{m} U_m f^{\dagger}_{m\uparrow} f_{m\uparrow} f^{\dagger}_{m\downarrow} f_{m\downarrow}, \tag{4.14}$$

where $c_{m\vec{k}\sigma}$ is an annihilation operator of a conduction electron with the wave vector $\vec{k}$ and the spin σ hybridizing with the f-electron in orbital m with a strength V_m. E_{fm} and U_m are the energy level of the f-electron and an intra-orbital Coulomb repulsion in orbital m, and the other Coulomb repulsion terms, like an inter-orbital interaction, are implicitly included in the "antiferromagnetic" Hund's-rule coupling (4.10).

We consider the case when the magnetic field is applied in the z-direction, the c-axis of $Th_{1-x}U_xRu_2Si_2$. The effect of the magnetic field for f^1-states is taken into account through the Zeeman terms defined by

$$\mathcal{H}_{\rm Zeeman}({\rm f}^1) = -\sum_{m} g_m \mu_{\rm B} S^z_m H, \tag{4.15}$$

where g-factors of orbital 1 and 2 are $g_1 = 90/49$ and $g_2 = 6/7$, respectively. The effects of the magnetic field for f^n-states ($n = 2, 3, 4$) are calculated by $\mathcal{H}_{\rm Zeeman}({\rm f}^n)$, which is the sum of the Zeeman term (4.15) for each f-electron. For example, $\langle \Gamma^{(2)}_{5,\pm} | \mathcal{H}_{\rm Zeeman}({\rm f}^2) | \Gamma^{(2)}_{5,\pm} \rangle = \pm(g_1 + g_2)\mu_{\rm B} H/2$ for f^2-state $|\Gamma^{(2)}_{5,\pm}\rangle$, (4.7) and (4.8), and $\langle \uparrow\downarrow, \uparrow | \mathcal{H}_{\rm Zeeman}({\rm f}^3) | \uparrow\downarrow, \uparrow \rangle = g_2 \mu_{\rm B} H/2$ for f^3-state $| \uparrow\downarrow, \uparrow \rangle \equiv f^{\dagger}_{1\uparrow} f^{\dagger}_{1\downarrow} f^{\dagger}_{2\uparrow} |0\rangle$, where $|0\rangle$ is the vacuum state, and so on. In the same manner, the Van Vleck contribution arising from the off-diagonal term between Γ_4 and Γ_3 in the f^2-singlet manifold is estimated as $\langle \Gamma_3 | \mathcal{H}_{\rm Zeeman}({\rm f}^2) | \Gamma_4 \rangle = -(g_1 - g_2)\mu_{\rm B} H/2$. However, this value is much smaller than that estimated in the LS-coupling scheme in the $J = 4$ manifold, $\langle \Gamma_4 | - g_J \mu_{\rm B} J_z H | \Gamma_3 \rangle = -2 g_J \mu_{\rm B} H_z$ with $g_J = 4/5$, because the higher $\Gamma^{(1)}_7$ doublet state in the $j = 5/2$ manifold in f^1-configuration has been discarded in constructing our model Hamiltonian (4.11)-(4.14). In fact, if we construct the Γ_4 and Γ_3 singlet states in the $j = 5/2$

manifold as

$$|\Gamma_3\rangle = \frac{3}{2\sqrt{7}}\left(|+\frac{5}{2}\rangle|-\frac{1}{2}\rangle + |+\frac{1}{2}\rangle|-\frac{5}{2}\rangle\right) + \frac{1}{2}\sqrt{\frac{5}{7}}\left(|+\frac{3}{2}\rangle|+\frac{1}{2}\rangle + |-\frac{1}{2}\rangle|-\frac{3}{2}\rangle\right), \tag{4.16}$$

$$|\Gamma_4\rangle = \frac{3}{2\sqrt{7}}\left(|+\frac{5}{2}\rangle|-\frac{1}{2}\rangle - |+\frac{1}{2}\rangle|-\frac{5}{2}\rangle\right) + \frac{1}{2}\sqrt{\frac{5}{7}}\left(|+\frac{3}{2}\rangle|+\frac{1}{2}\rangle - |-\frac{1}{2}\rangle|-\frac{3}{2}\rangle\right), \tag{4.17}$$

the off-diagonal term is estimated as $\langle\Gamma_3|\mathcal{H}_{\rm Zeeman}({\rm f}^2)|\Gamma_4\rangle = 2g_j\mu_{\rm B}H$ with $g_j = 6/7$, which almost coincides with the value estimated in the LS-coupling scheme in the $J = 4$ manifold. Thus, in order to take into account the Van Vleck contribution properly, we adopt the off-diagonal matrix element in the $J = 4$ manifold other than the contribution from the f^1-based Zeeman term.

We transform the conduction-band part of the Hamiltonian (4.12), with a logarithmic discretization parameter, $\Lambda = 2.5$, into the one-dimensional semi-infinite chain model and carry out the Wilson NRG method [19]. For simplicity, we take conduction bands to be symmetric in the energy space (with an extent from $-D$ to D) around the Fermi level. We keep the low lying 4000 states in each iteration step.

4.3 Characteristic Temperature $T_{\rm F}^*(H)$

The Hamiltonian (4.11) has two stable fixed points. One is the K-Y singlet fixed point (KY SFP) where the spin degree of freedom of each f-electron is screened by the conduction electrons with the same symmetry as the f-electron, leading to the phase shift in the unitarity limit as $\delta_m = \pi/2$ $(m = 1, 2)$. The other is the CEF singlet fixed point (CEF SFP) where two f-electrons form the singlet state due to the CEF effect, characterized by $\delta_m = 0$ $(m = 1, 2)$. Along the boundary of these two stable-fixed-point regions, there exists a locus of the unstable fixed points across which the ground state is interchanged. Around this line, NFL behaviors appear at $T_{\rm F}^* < T < T_x = \min(T_{\rm K2}, K)$, where $T_{\rm K2}$ is the lower Kondo temperature of two f-orbitals.

In general, E_{fm} and U_m, the energy level and the Coulomb interaction of each f-orbital, are different. However, for simplicity, we take the same values for each orbital, and the difference in characters of each orbital is introduced only through V_m. The Kondo temperature of orbital 2 is postulated to always

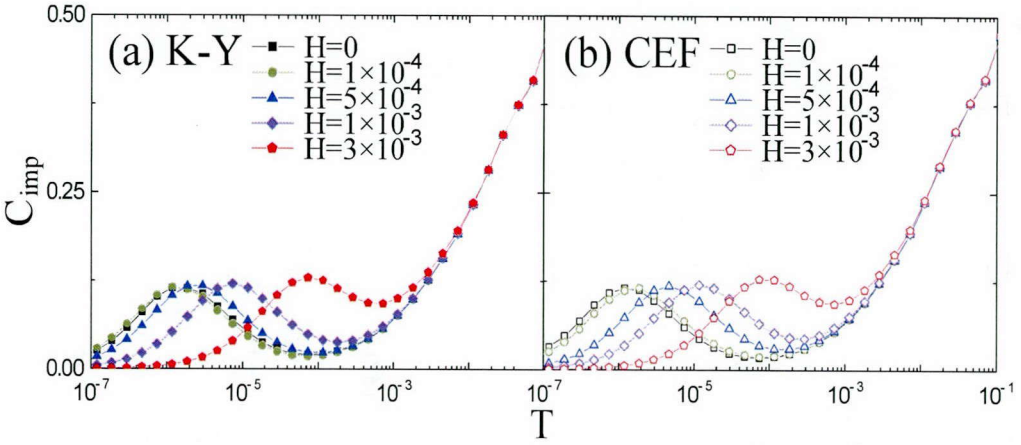

Figure 4.6: Temperature dependence of the specific heat $C_{\rm imp}$ for a series of magnetic fields H ($0 \leq H \leq 3\times10^{-3}$) for (a) $K = 0.0440$ with $T_{\rm F}^* = 1.44\times10^{-6}$ in the KY SFP, and (b) $K = 0.0488$ with $T_{\rm F}^* = 1.33 \times 10^{-6}$ in the CEF SFP.

be lower than that of orbital 1, $T_{\rm K1} > T_{\rm K2}$, and the parameters of the Hamiltonian (4.11) are fixed as $E_{f1} = E_{f2} = -0.4, U_1 = U_2 = 1.5, V_1 = 0.45$ and $V_2 = 0.30$ in the unit of D throughout this section. In addition, the magnetic field H is measured in the unit of $D/\mu_{\rm B}$. In the case of $K = \Delta = 0$, the Hamiltonian (4.11) reduces to two independent impurity Anderson models, where the Kondo temperatures determined by the Wilson's definition, $4T_{\rm K}\chi_{\rm imp}(T = 0) = 0.413$, are $T_{\rm K1} = 4.52 \times 10^{-2}$ and $T_{\rm K2} = 3.43 \times 10^{-3}$, respectively. In this chapter, we set the CEF level splittings as $K > \Delta$ which reproduces the anisotropy of the magnetic susceptibility, $\chi_z > \chi_\perp$ as pointed out in ref. 11. Moreover, we fix $\Delta = 0.12$ and control the degree of the competition by varying the CEF level splitting K. For the parameter set above, $K^* \simeq 0.0464$ gives the unstable fixed point, i.e., the ground state is the K-Y singlet for $K < K^*$ and the CEF singlet for $K > K^*$.

Figure 4.6 shows the temperature dependence of the specific heat for two cases: $K = 0.0440$ in the KY SFP region and for $K = 0.0488$ in the CEF SFP region, respectively. The characteristic temperature $T_{\rm F}^*$ is defined by the lowest temperature at which the specific heat $C_{\rm imp}(H) = \partial S_{\rm imp}(H)/\partial \ln T$, $S_{\rm imp}$ being the entropy due to the impurity, has a peak corresponding to the release of $\log\sqrt{2}$ entropy which characterizes the unstable fixed point [11, 13]. For these parameters, the characteristic temperatures are obtained as $T_{\rm F}^* \sim 1.44 \times 10^{-6}$ in the K-Y SFP region, and at $T_{\rm F}^* \sim 1.33 \times 10^{-6}$ in the CEF SFP region.

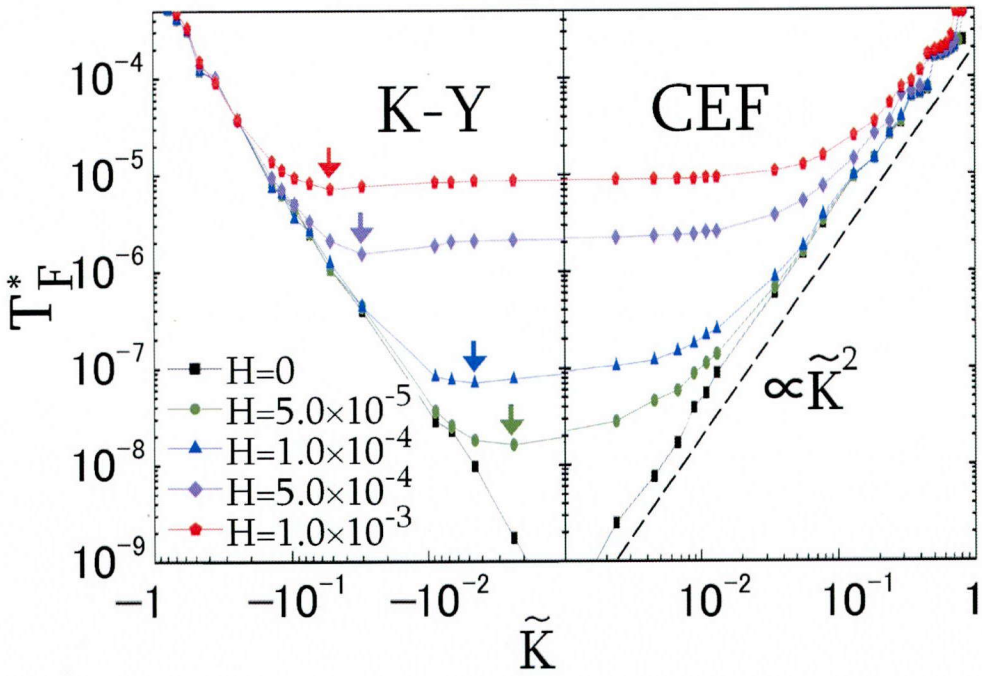

Figure 4.7: Characteristic temperature T_F^* vs $\tilde{K} \equiv (K - K^*)/K^*$ for a series of magnetic field H. Data points in the KY SFP are represented by closed symbols, while those in the CEF SFP are represented by open symbols. Arrows indicate the positions of the dip of $T_F^*(H)$.

In the case of the K-Y SFP region, T_F^* slightly decreases for a magnetic field $H = 1.0 \times 10^{-4}$, while the other values of the magnetic field increase T_F^*. On the other hand, in the case of the CEF SFP region, all values of the magnetic field increases T_F^*.

Figure 4.7 shows $\tilde{K} \equiv (K - K^*)/K^*$ dependence of $T_F^*(H)$. The characteristic temperature T_F^* is decreased by the competition. One can see in Fig. 4.7 that the $\tilde{K}$-dependence of T_F^* at $H = 0$ is given by $T_F^* \propto \tilde{K}^2$ around the QCP, indicating that T_F^* gives a degree of deviation from the QCP. When the magnetic field is applied, T_F^* increases, and the energy spectrum no longer suddenly interchanges at $K = K^*$ because the ground state is the mixed state between the CEF singlet and the K-Y singlet states. In the KY SFP region, there appears a dip (indicated by arrow in Fig. 4.7) at which T_F^* takes a minimum but remains non-zero. The energy spectrum obtained by the NRG calculation

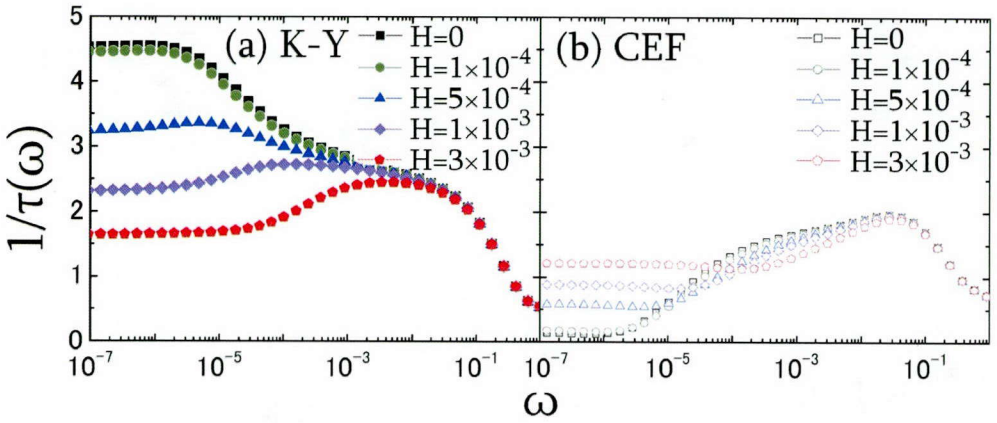

Figure 4.8: Frequency dependence of the total scattering rate $1/\tau(\omega)$ for a series of magnetic fields H ($0 \leq H \leq 3 \times 10^{-3}$) for (a) $K = 0.0440$ with $T_{\rm F}^* = 1.44 \times 10^{-6}$ in the KY SFP, and (b) $K = 0.0488$ with $T_{\rm F}^* = 1.33 \times 10^{-6}$ in the CEF SFP.

"gradually" crosses over between the types of the CEF and the K-Y singlet states around this dip. Namely, it is the point where the dominant singlet state of the two singlet states interchanges. As the magnetic field increases, this dip moves from $K = K^*$ to the low K region, which indicates that the magnetic field increases the weight of the CEF singlet state compared to that of the K-Y singlet state. This increase in the weight of the CEF singlet state originates in the off-diagonal term between Γ_3 and Γ_4 f^2-CEF singlet states because it stabilizes the energy level of the Γ_4 CEF singlet ground state. Hereafter, we investigate the H-dependence of physical quantities in two cases being close to the QCP: $K = 0.0440$ with $T_{\rm F}^* = 1.44 \times 10^{-6}$ in the KY SFP region and for $K = 0.0488$ with $T_{\rm F}^* = 1.33 \times 10^{-6}$ in the CEF SFP region, respectively.

Figure 4.8 shows the frequency dependence of the total scattering rate $1/\tau(\omega)$ at $T = 0$ for two cases, $K = 0.0440$ and $K = 0.0488$, where $1/\tau(\omega)$ is the sum of contributions from each orbital, and spin component $1/\tau_{m\sigma}(\omega) = 2\pi|V_m|^2 A_{m\sigma}(\omega)$, $A_{m\sigma}(\omega)$ being the single-particle spectral function. Data points in the KY SFP region are represented by closed symbols, while those in the CEF SFP region are represented by open symbols unless stated explicitly. The T-dependence of the resistivity can be inferred from $1/\tau(\omega)$ because ω and T are of the same order in the Fermi-liquid theory [20], e.g., in the case of the single orbital Anderson model, $1/\tau(\omega, T) \simeq [1/\tau(0,0)]\,[1 - (\omega^2 + \pi^2 T^2)/3T_{\rm K}^2 + \cdots]$

[21]. Although it is not shown as figures in the present chapter, $1/\tau(\omega)$ increases logarithmically in the region of $\omega \gtrsim T_{\rm K1}$ due to the screening of the f-electron by conduction electrons in orbital 1 in both cases. With decreasing ω toward $T_{\rm F}^*(\ll T_{\rm K2} < T_{\rm K1})$, $1/\tau(\omega)$ shows a logarithmic *increase* in the K-Y SFP region, but it shows a logarithmic *decrease* in the CEF SFP region. Finally, the Fermi-liquid behavior is restored in both regions, i.e., $1/\tau(\omega) \propto \omega^2$, at $\omega < T_{\rm F}^*(H=0)$.

When the magnetic field is applied, the residual scattering rate $1/\tau_0 \equiv 1/\tau(\omega)|_{\omega\to 0}$ decreases in the K-Y SFP region as seen in Fig. 4.8(a). There are two origins which induce such an increase of $1/\tau_0$: one is the mixing between the K-Y singlet and CEF singlet state in the ground state, and the other is the mixing between Γ_4 and Γ_3 singlet states through the off-diagonal term. As a result, the magnetic field leads the polarization of each f-electron. These magnetic moments make a singlet state, leading to the reduction of the phase shift. On the other hand, in the CEF SFP region, $1/\tau_0$ increases because the CEF-type ground state is polarized, and its magnetic moment scatters off the conduction electrons, leading to an increase of the phase shift and $1/\tau(\omega)$ at $\omega < T_{\rm F}^*(H=0)$. Because the weight of the CEF singlet state in the ground state drastically increases compared to that of the K-Y singlet state around the QCP, $1/\tau(\omega)$ in the K-Y SFP region shows the same T-dependence as in the CEF SFP region under high magnetic field. After all, the T-dependence of the resistivity $\rho_{\rm imp}$ due to the impurity scattering is essentially given by that of $1/\tau(\omega = T)$.

The magnetic susceptibilities, $\chi_{\rm imp} \equiv \partial M/\partial H$, are shown in Fig. 4.9 for these two cases. The magnetization M consists of M_1 (arising from the Zeeman term $\mathcal{H}_{\rm Zeeman}({\rm f}^n)$) and M_2 (arising from the Van Vleck term in f^2 configuration, eqs. (4.5) and (4.6)). M_1 is given as the thermal average of the magnetic moment m which is calculated as $m = \pm(g_1+g_2)\mu_{\rm B}/2$ for f^2-state $|\Gamma^{(2)}_{5,\pm}\rangle$, (4.7) and (4.8), and $m = \mu_{\rm B}g_2/2$ for f^3-state $|\uparrow\downarrow,\uparrow\rangle$, and so on. On the other hand, M_2 is given by an effect of the off-diagonal element of the magnetization between the f^2-CEF singlet states Γ_3, eq. (4.6), and Γ_4, eq. (4.5). In both cases, $\chi_{\rm imp}(T)$ shows the logarithmic T-dependence at around $T \sim T_{\rm K1}$ and $T_{\rm F}^* < T < \min(T_{\rm K2}, K)$. The magnetic field reduces the coefficient of the $-\log T$ term at $T_{\rm F}^* < T < \min(T_{\rm K2}, K)$ and the Van Vleck contribution. In particular, these reductions in the KY SFP region are smaller than those in the CEF SFP region. The origin of this phenomenon is the interchange of the weight of the two singlet states in the ground state. At higher magnetic fields, in both cases, the broad peak appears at $T \sim T_{\rm F}^*(H)$, where $T_{\rm F}^*$ is obtained from $C_{\rm imp}$ as mentioned above.

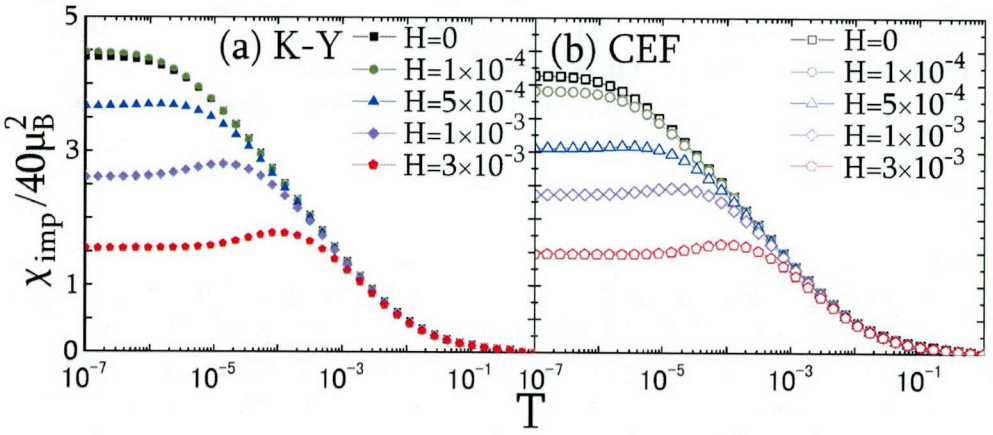

Figure 4.9: Temperature dependence of the susceptibility $\chi_{\rm imp}$ for a series of magnetic fields H ($0 \leq H \leq 3\times10^{-3}$) for (a) $K = 0.0440$ with $T_{\rm F}^* = 1.44\times10^{-6}$ in the KY SFP, and (b) $K = 0.0488$ with $T_{\rm F}^* = 1.33 \times 10^{-6}$ in the CEF SFP.

The Sommerfeld coefficients, $\gamma_{\rm imp}(T) \equiv C_{\rm imp}(T)/T$, are shown in Fig. 4.10 for two cases. As it is same with the case of $\chi_{\rm imp}$ $\gamma_{\rm imp}(T)$ shows the logarithmic T-dependence at around $T \sim T_{\rm K1}$ and $T_{\rm F}^* < T < \min(T_{\rm K2}, K)$ in both cases. When applying the magnetic field $H = 1.0 \times 10^{-4}$, $\gamma_{\rm imp}(T)$ is increased at $T \lesssim 10^{-6}$ in both cases. Such an increase of $\gamma_{\rm imp}(T)$ can be seen for all magnetic field although the temperature regions depends on the value of magnetic field. At $T \ll T_{\rm F}^*$, $\gamma_{\rm imp}(T)$ takes the constant value. This constant value is decreased by magnetic field, which means that the magnetic field relaxes the competition between two singlet states.

4.4 Scaling Behavior of Characteristic Temperature $T_{\rm F}^*(H)$

From the data of the T or ω dependence of $C_{\rm imp}$, $\chi_{\rm imp}$ and $1/\tau$ under the magnetic field H, we obtain the H-dependence of $T_{\rm F}^*(H)$, as shown in Fig. 4.11(a), where the $T_{\rm F}^*(H)$ of $1/\tau$ and $\chi_{\rm imp}$ are defined as the temperature at which the logarithmic T-dependence stops with decreasing ω and T toward 0. We define the crossover magnetic field $H_{\rm cr}$ as the intersection point of linear fits (dotted lines) on the log-log plot for high and low magnetic field regions in the CEF SFP region ($K = 0.0488$ and $\tilde{K} = 0.05172$) as shown in Fig. 4.11(a). It is remarkable that so determined $H_{\rm cr}$'s for three different physical quantities, $C_{\rm imp}$, $\chi_{\rm imp}$, and $1/\tau$, almost coincide with each other as shown by arrows in Fig.4.11(a), giving a solid basis for defining the crossover magnetic field $H_{\rm cr}$. In

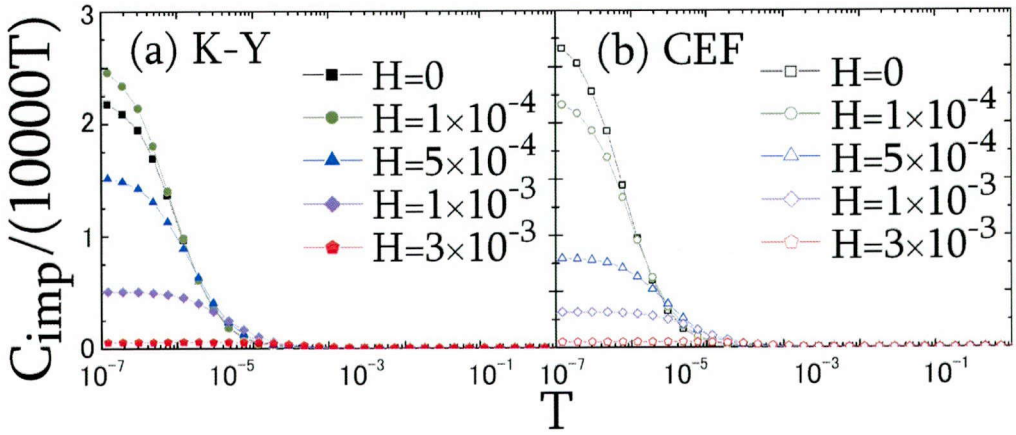

Figure 4.10: Temperature dependence of the Sommerfeld coefficient $C_{\rm imp}/T$ for a series of magnetic fields H ($0 \leq H \leq 3 \times 10^{-3}$) for (a) $K = 0.0440$ with $T_{\rm F}^* = 1.44 \times 10^{-6}$ in the KY SFP, and (b) $K = 0.0488$ with $T_{\rm F}^* = 1.33 \times 10^{-6}$ in the CEF SFP.

the KY SFP region ($K = 0.0440$ and $\tilde{K} = -0.05172$), the $H_{\rm cr}$'s are similarly defined, although $T_{\rm F}^*$ obtained from $\chi_{\rm imp}$ exhibits a tiny dip near $H = H_{\rm cr}$. Linear fits are not shown for the clarity of the presentation. The crossover magnetic field $H_{\rm cr}$ so determined for $C_{\rm imp}$, $1/\tau$, and $\chi_{\rm imp}$ almost coincide again. These $H_{\rm cr}$'s in the two singlet-fixed-point regions almost coincide with each other because the absolute values of $\tilde{K}$ for these two parameters are almost the same, while $H_{\rm cr}$ depends crucially on $\tilde{K} \equiv (K - K^*)/K^*$, the deviation from the QCP. Normalized characteristic temperatures, $T_{\rm F}^*(H)/T_{\rm F}^*(H = 0)$, are shown in Figs. 4.11(b) and 4.11(c) as a function of a normalized magnetic field $H/H_{\rm cr}$ from the three physical quantities as above. Figure 4.11(b) is for the KY SFP with parameters $K = 0.0440$ giving $T_{\rm F}^*(H = 0) = 1.44 \times 10^{-6}$ and $K = 0.0460$ giving $T_{\rm F}^*(H = 0) = 2.80 \times 10^{-8}$, and Fig. 4.11(c) is for the CEF SFP with parameters $K = 0.0488$ giving $T_{\rm F}^*(H = 0) = 1.33 \times 10^{-6}$ and $K = 0.0468$ giving $T_{\rm F}^*(H = 0) = 3.79 \times 10^{-8}$. These four lines exhibit a good scaling property in both cases, which indicates the following two important facts.

First, $T_{\rm F}^*(H)$'s of the three quantities, $C_{\rm imp}$, $1/\tau$, and $\chi_{\rm imp}$, exhibit qualitatively the same behaviors while they are qualitatively different. Second, the scaling property holds both in the CEF SFP and the KY SFP regions even if a degree of the deviation from the QCP is different. It is noted that the shapes of the normalized plots for the two stable fixed points are different from each

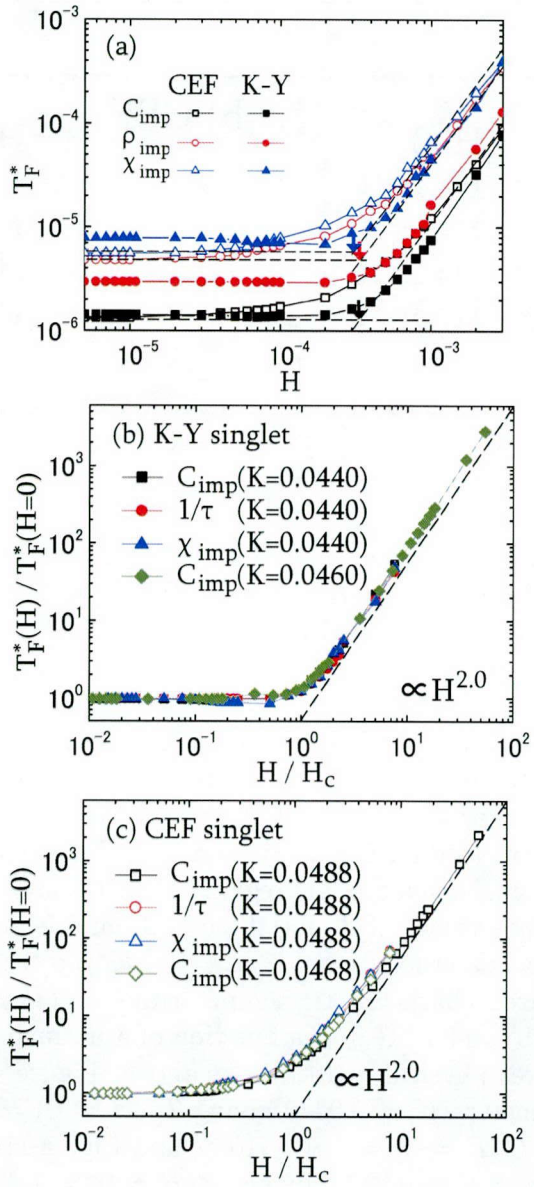

Figure 4.11: (a) Characteristic temperature $T_{\rm F}^*(H)$ vs magnetic field H for the two cases with CEF (for $K = 0.0488$ and $\tilde{K} = 0.05172$ shown by open symbols) and K-Y (for $K = 0.0440$ and $\tilde{K} = -0.05172$ shown by closed symbols) singlet fixed points. The crossover magnetic field $H_{\rm cr}$'s are shown by down arrows in the case of the CEF singlet fixed point. (b) and (c) are scaling plots of $T_{\rm F}^*(H)/T_{\rm F}^*(H = 0)$ vs $H/H_{\rm cr}$ for the KY SFP and the CEF SFP, respectively.

other. In the region $H \ll H_{\rm cr}(\tilde{K})$, $T_{\rm F}^*(H)$ is independent of H, and $T_{\rm F}^*(H)$ is robust against the low magnetic field in particular, so that the three physical quantities discussed above are not affected appreciably. We have previously found this robustness of $T_{\rm F}^*(H)$ against H, as seen in ref. 13. On the other hand, all the $T_{\rm F}^*(H)$'s show the H-dependent form as $T_{\rm F}^*(H) \propto H^x$ in the region $H_{\rm cr}(\tilde{K}) \ll H < \min(T_{\rm K2}, K)$. The exponent x is estimated to be $x \simeq 2.0$ both in the CEF and the K-Y SFP regions. These two regions continuously cross over at around $H \simeq H_{\rm cr}(\tilde{K})$. Of course, it is possible that $T_{\rm F}^*(H)$ can be fitted as $T_{\rm F}^*(H) \propto H$ in a very narrow region of the magnetic field near $H = H_{\rm cr}$, especially in the CEF SFP region as seen in Fig. 4.11(c). However, such a scaling behavior should be regarded as that of a cross over, but not an asymptotic anomalous behavior.

Such a H-dependence of $T_{\rm F}^*(H)$ can be understood by considering the similarity of the unstable fixed point with that of the TCK effect. In the case of the TCK model, there are two origins which break the unstable fixed point, the magnetic field which polarizes the local spin leading to the "unusual" Fermi-liquid fixed point characterized by the energy scale $T_{\rm F}^* \propto H^2/T_{\rm K}$ [8], and the channel anisotropy of the exchange interaction which leads to the Fermi-liquid fixed point [3, 4, 9]. Indeed, the Hamiltonian (4.11) can be regarded as the TCK model below $T_{\rm K1}$ because the f-electron in orbital 2 interacts with two "conduction" electron channels: one is the conduction electrons in orbital 2, and the other is a complex of conduction electrons and screened the f-electron in orbital 1 [11, 13]. In the present model, these two types of "conduction" electron play the role of the channels. The change of the energy difference between two singlet states, which is induced by the magnetic field as mentioned above, affects the coupling constants between f-electron in orbital 2 and these "conduction" electrons. Namely, these two coupling constants have the magnetic field dependences. Thus, the "channel" anisotropy for two types of "conduction" electrons is induced by the magnetic field, and system goes to the Fermi-liquid fixed point, even though the ground state is the mixed state of the two singlet states. In other words, in the present model, the magnetic field breaks the unstable fixed point by two mechanisms, the polarization of f-electrons and the "channel" anisotropy.

In the region $H \ll H_{\rm cr}$, the system flows into the Fermi-liquid fixed point induced by the "channel" anisotropy. In the CEF SFP region, $T_{\rm F}^*$ shows little change against low H. However, in the K-Y SFP region, $T_{\rm F}^*$ slightly decreases as H increases, which corresponds to the dip in Fig. 4.7. Namely, the weight of the CEF singlet state in the ground state increases compared to that of the K-Y singlet state, and the dominant singlet state of the two singlet states

interchanges at $H = H_{\rm cr}$. On the other hand, in the region $H_{\rm cr} \ll H$, the magnetic field induces the Fermi-liquid fixed point by the polarization of f-electrons as in the case of the TCK effect because $T_{\rm F}^*(H)$ is characterized by H^2 as in the case of the TCK effect under the magnetic field. These two effects compete with each other at around $H \sim H_{\rm cr}(\tilde{K})$ giving the crossover between the two regions.

The exponent of H in $T_{\rm F}^*(H)$ asymptotically approaches 2.0 in the high magnetic field region $H \gg H_{\rm cr}$ in both SFP regions, as shown in Figs. 4.11(b) and (c). However, the magnetic field necessary for reaching the $T_{\rm F}^* \propto H^2$ behavior in the CEF SFP region is higher than that in the K-Y SFP region. This difference stems from the existence of the Γ_3 excited CEF singlet state which gives additional magnetic field dependence for the Γ_4 CEF singlet ground state through the off-diagonal term between these two CEF singlet states. This is verified by a NRG calculation that the exponent of H in the CEF SFP region readily comes close to 2.0 at $H > H_{\rm cr}$, as in the K-Y SFP region, if we discard the off-diagonal term between f^2-CEF singlet states by the magnetic field, although an explicit result is not shown here.

4.5 Result for Another Crystalline-Electric-Field Scheme

Although we shows the results when we take the low-lying CEF scheme as $\Gamma_4 - \Gamma_3 - \Gamma_5^{(2)}$, we obtain similar NFL behaviors and the magnetic field dependence of $T_{\rm F}^*(H)$ even if the low-lying CEF scheme is $\Gamma_4 - \Gamma_5^{(2)} - \Gamma_3$, i.e., $K < \Delta$. Here, we shows the results for another parameter set of the Hamiltonian (4.11) as $E_{f1} = E_{f2} = -0.4, U_1 = U_2 = 1.5, V_1 = 0.36$ and $V_2 = 0.30$, which gives $T_{\rm K1} = 1.10 \times 10^{-2}$ and $T_{\rm K2} = 2.31 \times 10^{-3}$ by the Wilson's definition in the case of $K = \Delta = 0$. In this section, we fix $K = 0.10$ and control the degree of the competition by varying the CEF level splitting Δ. For the parameter set above, $\Delta^* \simeq 0.00858$ gives the unstable fixed point, i.e., the ground state is the K-Y singlet for $\Delta < \Delta^*$ and the CEF singlet for $\Delta > \Delta^*$.

With the same procedure as the previous section, we obtain the H-dependence of $T_{\rm F}^*(H)$ as shown in Fig. 4.12(a). We define the crossover magnetic field $H_{\rm cr}$ as the same way as shown in Fig. 4.12(a). It is noted again that so determined $H_{\rm cr}$'s for three different physical quantities, $C_{\rm imp}$, $\chi_{\rm imp}$, and $1/\tau$, almost coincide with each other as shown by arrows in Fig.4.12(a). Here, in the K-Y SFP region ($\Delta = 0.0081$ and $\tilde{\Delta} = -0.0559$), the $H_{\rm cr}$'s are defined by where $T_{\rm F}^*$ takes a minimum. As in the case of the previous section, the crossover magnetic field $H_{\rm cr}$'s for $C_{\rm imp}$, $1/\tau$, and $\chi_{\rm imp}$ almost coincide again. Normalized characteristic temperatures, $T_{\rm F}^*(H)/T_{\rm F}^*(H = 0)$, are shown in Figs. 4.12(b) for the K-Y SFP

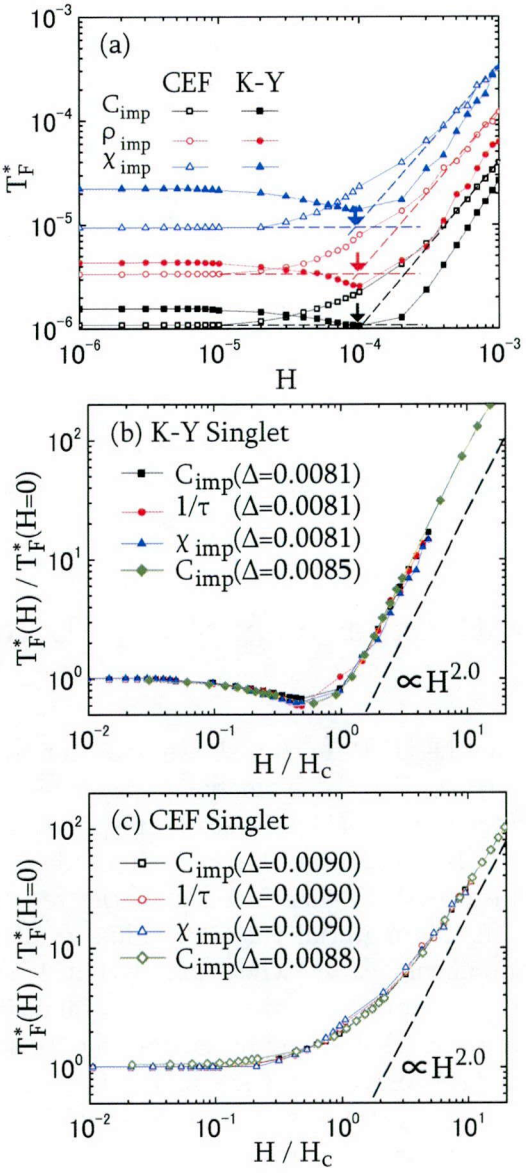

Figure 4.12: (a) Characteristic temperature $T_{\rm F}^*(H)$ vs magnetic field H for the two cases with CEF (for $\Delta = 0.0090$ and $\tilde{\Delta} = 0.0490$ shown by open symbols) and K-Y (for $\Delta = 0.0081$ and $\tilde{\Delta} = -0.0559$ shown by closed symbols) singlet fixed points. The crossover magnetic field $H_{\rm cr}$'s are shown by down arrows in the case of the CEF singlet fixed point. (b) and (c) are scaling plots of $T_{\rm F}^*(H)/T_{\rm F}^*(H = 0)$ vs $H/H_{\rm cr}$ for the K-Y singlet fixed point and the CEF singlet fixed point, respectively.

and 4.12(c) for the CEF SFP as a function of a normalized magnetic field $H/H_{\rm cr}$ from the three physical quantities as above. It is noted that, in the K-Y SFP region, $T_{\rm F}^*$ decreases as H increases in the region $H \ll H_{\rm cr}$, which does not occur in another CEF level scheme, i.e., Fig. 4.11(a). As mentioned above, the magnetic field increases the weight of the CEF singlet state. Furthermore, the magnetic field could decrease the weight of the K-Y singlet state because the magnetic field lifts the degeneracy of $\Gamma^{(5)}$-doublet and increases the energy level of state written in eq. 3.8 which stabilize the K-Y singlet state through the "spin"-flip process. (Here, "spin" means the quasispin.) On the other hand, the H-dependence of $T_{\rm F}^*(H)$'s in Fig. 4.12(b) and Fig. 4.12(c) are almost coincide with that in Fig. 4.11(b) and Fig. 4.11(c) in the region $H_{\rm cr}(\tilde{\Delta}) \ll H < \min(T_{\rm K2}, \Delta)$. This fact indicates that the similar NFL behaviors would be obtained if there exist the CEF singlet ground state and the strong hybridization between conduction electrons and f-electron, namely details of the CEF scheme would not be essential matters.

4.6 Comparison with Experiment of $Th_{1-x}U_xRu_2Si_2$ with $x \simeq 0.03$

In the CEF SFP region near the QCP, $1/\tau(\omega)$ shows behavior consistent with the results of $\rho_{\rm imp}(T)$ in $Th_{1-x}U_xRu_2Si_2$. Namely, $1/\tau(\omega)$ exhibits a $\log\omega$-like decrease toward $T_{\rm F}^*$ and increases as H increases corresponding to the positive magnetic resistance. It is noted that the $T_{\rm K1}$ is considered to be much higher than the $T_{\rm K2}$ because the $\log T$-like increase of the resistivity around $T \simeq T_{\rm K1}$ is not observed in this material [14, 16]. This result is consistent with that obtained by Yotsuhashi *et al*, who showed that $1/\tau(\omega)$, $\chi_{\rm imp}(T)$ and the H-dependence of $\gamma_{\rm imp}$ reproduces these physical quantities observed in $Th_{1-x}U_xRu_2Si_2$. A more remarkable finding is that the H-dependence of $T_{\rm F}^*(H)$ at around $H \sim H_{\rm cr}(\tilde{K})$ for $K = 0.0488$ in the CEF SFP region reproduces the H-dependence of $T_{\rm F}^*(H)$ observed in $Th_{1-x}U_xRu_2Si_2$ analyzed from the resistivity [22]. As shown in Figs. 4.13 and 4.14, the agreement between our theoretical result and experimental one is nearly perfect concerning the normalized magnetic field, H/H_1, dependence of $T_{\rm F}^*(H)$ normalized by $T_{\rm F}^*(H_1)$, where $H_1 = 3.0 \times 10^{-4} D/\mu_{\rm B}$ (D being half the bandwidth of conduction electrons) for our theoretical result and $H_1 = 1$[T] for experimental result. Namely, our scaling plot is in good agreement with that of the experimental one of $Th_{1-x}U_xRu_2Si_2$ [22].

It is also emphasized that our theoretical analysis strongly suggests that

$Th_{1-x}U_xRu_2Si_2$ is located in the CEF singlet side near the critical phase boundary between the KY SFP and the CEF SFP regions. On the other hand, it was emphasized that $T_F^*(H)$ is proportional to the magnetic field H [22], especially in the analysis of the T-dependence of χ_{imp}. However, it is apparent that the linear fit fails to reproduce the experimental results for the $T_F^*(H)$ obtained from the resistivity ρ_{imp}. Their statement stemmed from the analysis of χ_{imp} assuming that the coefficient of the $-\log T$ term in χ_{imp} were independent of H. Experimentally, however, magnetic fields up to 5 Tesla seem to change this coefficient and drastically decrease the Van Vleck contribution to χ_{imp} [22].

In the case of $R_{1-x}U_xRu_2Si_2$ (R= La and Y), the experimental results show that T_F^*'s of these material are higher than that in the case of R=Th [16, 17]. It indicates that parameter sets of these materials may be located more distant from the QCP than that of $Th_{1-x}U_xRu_2Si_2$. Our theoretical result predicts that pressure may induce the transition from the CEF SFP region to the K-Y SFP region, giving rise to the drastic increase of $1/\tau_0$.

In the present chapter, we take the same CEF level scheme as that discussed in ref. 11, because their level scheme can reproduce the experimental results in $R_{1-x}U_xRu_2Si_2$ (R=Th, Y and La). However, even if the low-lying CEF scheme is Γ_4-$\Gamma_5^{(2)}$-Γ_3, we have verified that the similar NFL behaviors and the magnetic field dependence of $T_F^*(H)$ occur as shown in section 4.5.It indicates that the similar NFL behaviors would be obtained if there exist the CEF singlet ground state and the strong hybridization between conduction electrons and f-electron, namely details of the CEF scheme would not be essential matters. It is remarked that CEF states with Γ_2 singlet ground state, proposed as a plausible candidate for "Hidden Order" state of URu_2Si_2 [23, 24], would exhibit the local non-Fermi liquid behaviors discussed in the present chapter. The actual calculation in those CEF level schemes is left for the future study.

Quite recently, it is argued that the H-dependence of NFL behaviors observed in $Th_{1-x}U_xRu_2Si_2$ can be understood within the TCK model if some conditions would be satisfied in the CEF level scheme [22, 23]. A crucial difference between ref. 24 and our present result is the magnetic-field dependence of T_F^* in the high magnetic field region $H > 5$ Tesla. Namely, there exists a region of a magnetic field where $T_F^* \propto H^2$ in the high magnetic field region in our result as shown in Fig. 4.13, while there exists no such a region of a magnetic field in the scenario of ref. 24. Because our theoretical result almost completely reproduces $T_F^*(H)$ observed experimentally in the magnetic field $H < 5$T, which corresponds to the crossover region of the H-dependence of $T_F^*(H)$ from $T_F^* \propto H^0$ to $T_F^* \propto H^2$. Therefore, we expect that our theory can also be applied to the high magnetic field region beyond $H = 5$T, where

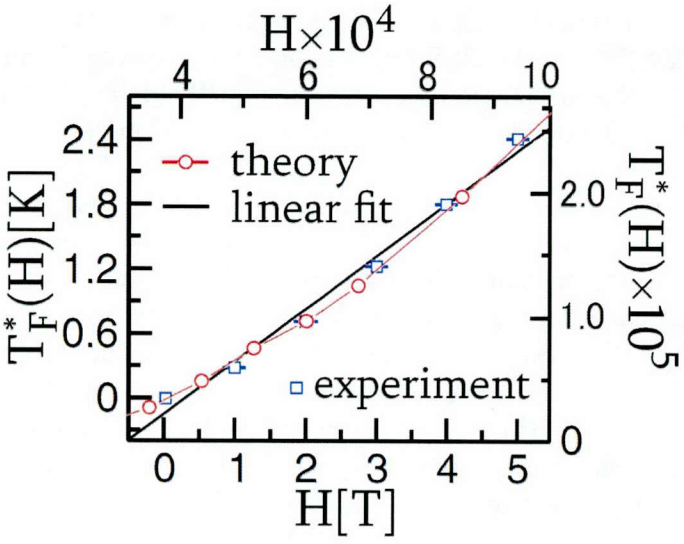

Figure 4.13: Comparison between theoretical and experimental results of $T_{\rm F}^*(H)$. The red ∘ symbols are for the H-dependence of $T_{\rm F}^*(H)$ (the upper and the right scales) obtained theoretically from $C_{\rm imp}$ for $K = 0.0488$. The blue □ symbols are for the H-dependence $T_{\rm F}^*(H)$ (the lower and the left scales) observed in $Th_{1-x}U_xRu_2Si_2$ for the resistivity $\rho_{\rm imp}$, which was scaled linearly by Tóth *et al*[22].

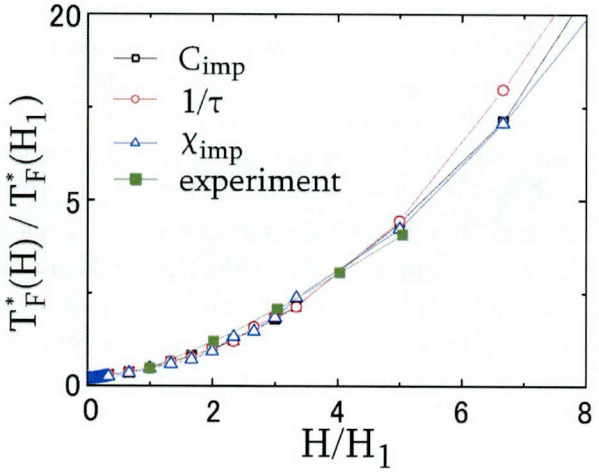

Figure 4.14: H/H_1 vs $T_{\rm F}^*(H)/T_{\rm F}^*(H_1)$, the normalized characteristic temperature, for theoretical and experimental results. Those obtained from $C_{\rm imp}$ and $\rho_{\rm imp}$ are normalized by the value at $H_1 = 3.0 \times 10^{-4}$, while the experimental result is normalized by the value at $H_1 \simeq 1$[T].

$T_{\rm F}^{*} \propto H^2$ is expected theoretically.

4.7 Conclusion

We have investigated the magnetic field (H) dependence of the NFL behaviors arising from the competition between the CEF singlet and the K-Y singlet states in tetragonal symmetry. We have found that the characteristic temperature $T_{\rm F}^{*}(H)$, below which the Fermi liquid behavior recovers, changes its H-dependence at around the critical magnetic field $H_{\rm cr}$. While $T_{\rm F}^{*}$ is not affected by H in the region $H \ll H_{\rm cr}$, it is expressed as $T_{\rm F}^{*} \propto H^{x}$ ($x \simeq 2.0$) in the region $H \gg H_{\rm cr}$. For both high and low magnetic field regions, such a behavior of $T_{\rm F}^{*}(H)$ follows the scaling form even if the degree of the deviation from the QCP is different. We have also found that $T_{\rm F}^{*}(H)$ shows the anomalous H-dependence around $H \sim H_{\rm cr}$, which is in good agreement with that observed in $Th_{1-x}U_xRu_2Si_2$.

Bibliography of Chapter 4

[1] D. L. Cox: Phys. Rev. Lett. **59** (1987) 1240.

[2] P. D. Sacramento and P. Schlottmann: Phys. Rev. B **43** (1991) 13294.

[3] H. B. Pang and D. L. Cox: Phys. Rev. B **44** (1991) 9454.

[4] I. Affleck, A. W. W. Ludwig, H. B. Pang, and D. L. Cox: Phys. Rev. B **45** (1992) 7918.

[5] O. Sakai, S. Suzuki, Y. Shimizu, H. Kusunose, and K. Miyake: Solid State Commun. **99** (1996) 461.

[6] H. Kusunose, K. Miyake, S. Shimizu, and O. Sakai: Phys. Rev. Lett. **76** (1996) 271.

[7] D. L. Cox and A. Zawadowski: Adv. Phys. **47** (1998) 599, and references therein.

[8] G. Zaránd, T. Costi, A. Jerez, and N. Andrei: Phys. Rev. B **65** (2002) 134416.

[9] S. Yotsuhashi and H. Maebashi: J. Phys. Soc. Jpn. **71** (2002) 1705.

[10] Y. Shimizu, O. Sakai, and Y. Kuramoto: Physica B **206-207** (1995) 135.

[11] S. Yotsuhashi, K. Miyake, and H. Kusunose: J. Phys. Soc. Jpn. **71** (2002) 389.

[12] K. Hattori and K. Miyake: J. Phys. Soc. Jpn. **74** (2005) 2193.

[13] S. Nishiyama, H. Matsuura, and K. Miyake: J. Phys. Soc. Jpn. **79** (2010) 104711.

[14] H. Amitsuka and T. Sakakibara: J. Phys. Soc. Jpn. **63** (1994) 736.

[15] K. Marumoto, T. Takeuchi, and Y. Miyako: Phys. Rev. B **54** (1996) 12194.

[16] H. Amitsuka, K. Kuwahara, M.Yokoyama, K.Tenya, T. Sakakibara, M. Mihalik, and A. Menovský: Physica B **281-282** (2000) 326.

[17] M. Yokoyama, H. Amitsuka, K. Kuwahara, K. Tenya, and T. Sakakibara: J. Phys. Soc. Jpn. **71** (2002) 3037.

[18] A. Tóth, P. Chandra, P. Coleman, G. Kotliar, and H. Amitsuka: Phys. Rev. B **82** (2010) 235116.

[19] K. G. Wilson: Rev. Mod. Phys. **47** (1975) 773.

[20] A. A. Abrikosov, L. P. Gor'kov, and I. Y. Dzyaloshinskii: *Quantum Field Theoretical Method in Statistical Physics* (Pergamon Press, London, 1965), Chap. 4, Sect. 21.

[21] P. Nozières: J. Low Temp. Phys. **17** (1974) 31; Note that the coefficient of the T^2 term in the resistivity $\rho_{\rm imp}$ is larger than that of $1/\tau$ by three times, as discussed in this reference.

[22] A. Tóth and G. Kotliar: Phys. Rev. Lett. **107** (2011) 266405.

[23] K. Haule and G. Kotliar: Nat. Phys. **5** (2009) 796.

[24] H. Kusunose and H. Harima: J. Phys. Soc. Jpn. **80** (2011) 084702.

Chapter 5

Analysis in f^2 Crystalline-Electric-Field Singlet-Triplet Configuration with Cubic Symmetry

5.1 Introduction

In most Pr- and U-based compounds with two localized f-electrons, the crystalline-electric-field (CEF) ground state can be the singlet state. Some of these materials show a resistance minimum phenomenon, the Kondo effect, in which each f-electron forms the Kondo-Yosida (K-Y) singlet state with conduction electrons in the ground state due to the hybridization between an f-electron and conduction electrons. In the tetragonal symmetry, it is already known that competition between the f^2-CEF singlet state and the K-Y singlet state in the ground state gives rise to an unstable fixed point which causes non-Fermi liquid behavior in various physical quantities, such as the resistivity, the Sommerfeld coefficient and the magnetic susceptibility. In order to clarify the rich properties caused by competition in the tetragonal symmetry, many theoretical works concerning a model for the level of impurity have been carried out [1, 2, 3, 4, 5]. Some theoretical works in cubic symmetry have also been carried out [1, 6, 7, 8, 9]. However, a more detail discussion is desirable.

In this chapter, we investigate how a system with the f^2-CEF singlet ground state in the cubic symmetry is affected by hybridizations with conduction electrons with an impurity model. Recently, some studies using conduction electrons of either Γ_7 or Γ_8 symmetry have been carried out in the cubic symmetry

[6, 7, 9]. Such a treatment may be sufficient to discuss properties of some materials with the f^2-configuration, e.g., the conduction electrons in $PrRu_4Sb_{12}$ mainly come from the pnictogen molecular orbital with A_{1u} (i.e., Γ_7) symmetry [11]. However, it is natural to suspect that hybridizations with conduction electrons of various symmetries determine the properties and the fixed point of the systems in most materials. Theoretically, when the hybridization with the Γ_8 conduction band is considered, there exist two fixed points: one is the f^2-CEF singlet fixed point, and the other is the triplet fixed point [8]. However, there certainly exists the K-Y singlet fixed point when hybridizations with Γ_7 and Γ_8 conduction bands are considered [1]. Thus, it is necessary to clarify the properties of the model in which hybridizations with conduction electrons of both Γ_7 and Γ_8 symmetries are considered as a first step prior to discussing the anomalous properties in f^2-configuration heavy fermion systems.

The purpose of this chapter is to elucidate the properties of the f^2 configuration system with cubic symmetry in an impurity model. Hattori and Miyake have already discussed this issue on an extended impurity Anderson model with the f^2-CEF level scheme of Γ_1-Γ_4 symmetry hybridizing with Γ_7 and Γ_8 conduction bands [8] on the basis of the numerical renormalization group (NRG) method [10]. They have shown that there are two stable fixed points: one is the CEF singlet fixed point, the other is the triplet fixed point caused by the stabilization of the Γ_4 first excited triplet state due to the hybridization with conduction electrons of Γ_8 symmetry, and there exists an unstable fixed point at the boundary between these two stable fixed points. Here, we also investigate the same model as that in ref. 8 on the basis of the NRG method [10], and show that the CEF singlet state smoothly crosses over to the K-Y singlet state as hybridizations with Γ_7 and Γ_8 conduction bands increase in cubic symmetry, although it has been shown that these two singlet states interchange sharply, giving rise to an unstable fixed point between them in tetragonal symmetry [3, 4, 5].

This chapter is organized as follows. In §5.2, we recapitulate the model Hamiltonian by taking into account hybridizations with conduction electrons of Γ_7 and Γ_8 symmetries, to discuss the properties in cubic symmetry. In §5.3, we show there exist two fixed points, the singlet fixed point and the triplet fixed point, and the CEF singlet state and the K-Y singlet state smoothly cross over within the singlet fixed point. Moreover, we find that the characteristic temperature is suppressed at the boundary between these two fixed points, which indicates that there exists the unstable fixed point. In §5.4, we show the physical behaviors such as the entropy, the Sommerfeld coefficient, and the resistivity, and discuss how these physical behaviors are affected at

the boundary between two fixed points and the crossover between two singlet states. In §5.5, we discuss the applicability of the present result for understanding the experimental result of UBe_{13}, i.e., the Sommerfeld coefficient has the peak structure at the lattice constant of UBe_{13} when the lattice constant is controlled by replacing U atoms partly with other nonmagnetic elements, as shown in Fig. 3.10 in §3.3, and summarize this chapter in §5.6.

5.2 Model Hamiltonian

Here, we recapitulate discussions of ref. 8 about how to dèrive the model Hamiltonian for discussing the properties in cubic symmetry on the basis of the j-j coupling scheme. As for f^1-states, we only consider the low-lying $j = 5/2$ multiplet, which splits into the Γ_7 doublet state and the Γ_8 quartet state due to the CEF effect in cubic symmetry. For convenience, we call the two sets of Kramers doublets in Γ_8 symmetry as Γ_{81}- and Γ_{82}-orbitals, and allot these f^1-states the pseudospin states as follow:

$$|f^1\Gamma_{7+}\rangle = \frac{1}{\sqrt{6}}|\frac{5}{2}\rangle - \sqrt{\frac{5}{6}}|-\frac{3}{2}\rangle \qquad \equiv |\uparrow,0,0\rangle, \tag{5.1}$$

$$|f^1\Gamma_{7-}\rangle = \frac{1}{\sqrt{6}}|-\frac{5}{2}\rangle - \sqrt{\frac{5}{6}}|+\frac{3}{2}\rangle \qquad \equiv |\downarrow,0,0\rangle, \tag{5.2}$$

$$|f^1\Gamma_{81+}\rangle = \sqrt{\frac{5}{6}}|+\frac{5}{2}\rangle + \frac{1}{\sqrt{6}}|-\frac{3}{2}\rangle \qquad \equiv |0,\uparrow,0\rangle, \tag{5.3}$$

$$|f^1\Gamma_{81-}\rangle = \sqrt{\frac{5}{6}}|-\frac{5}{2}\rangle + \frac{1}{\sqrt{6}}|+\frac{3}{2}\rangle \qquad \equiv |0,\downarrow,0\rangle, \tag{5.4}$$

$$|f^1\Gamma_{82+}\rangle = |-\frac{1}{2}\rangle \qquad \equiv |0,0,\uparrow\rangle, \tag{5.5}$$

$$|f^1\Gamma_{82-}\rangle = |+\frac{1}{2}\rangle \qquad \equiv |0,0,\downarrow\rangle. \tag{5.6}$$

For example, $|\uparrow,0,0\rangle$ represents the state in which the up-pseudospin occupies the Γ_7 orbital and the others are empty. It might be natural to define the pseudospin state in Γ_{82} as $|\Gamma_{82\sigma}\rangle \equiv |\sigma/2\rangle$. However, the definitions in eqs. (5.5) and (5.6) are suitable for the NRG method because the z-component of the total pseudospin becomes a conserved quantity, as discussed later.

As for f^2-states, we also restrict f^2-states within four low-lying states, Γ_1 singlet and Γ_4 triplet states in $J = 4$ multiplet. In order to discuss the Kondo effect of each f-electron in f^2-states, we rewrite the f^2-CEF states by using

the j-j coupling scheme.

$$|f^2\Gamma_1\rangle = \sqrt{\frac{5}{24}}\left(|4\rangle + |-4\rangle\right) + \sqrt{\frac{7}{12}}|0\rangle$$

$$= \frac{1}{\sqrt{6}}\left(2|\uparrow\downarrow,0,0\rangle + |0,\uparrow\downarrow,0\rangle - |0,0,\uparrow\downarrow\rangle\right), \tag{5.7}$$

$$|f^2\Gamma_4^-\rangle = \sqrt{\frac{1}{8}}|-3\rangle + \sqrt{\frac{7}{8}}|1\rangle \quad = \frac{1}{2}|\downarrow,\downarrow,0\rangle - \frac{\sqrt{3}}{2}|\uparrow,0,\downarrow\rangle, \tag{5.8}$$

$$|f^2\Gamma_4^0\rangle = \frac{1}{\sqrt{2}}\left(|4\rangle - |-4\rangle\right) \quad = \frac{1}{\sqrt{2}}\left(|\uparrow,\downarrow,0\rangle + |\downarrow,\uparrow,0\rangle\right), \tag{5.9}$$

$$|f^2\Gamma_4^+\rangle = \sqrt{\frac{1}{8}}|3\rangle + \sqrt{\frac{7}{8}}|-1\rangle \quad = \frac{1}{2}|\uparrow,\uparrow,0\rangle - \frac{\sqrt{3}}{2}|\downarrow,0,\uparrow\rangle. \tag{5.10}$$

We assume that the Γ_1 singlet state is the ground state and the Γ_4 triplet state is the first excited state with an excitation energy splitting η in the f^2-level scheme, and that the energy level of the Γ_7 doublet is always lower than that of the Γ_8 quartet in the f^1-level scheme. Figure 5.1 shows the schematic energy level scheme in each f-electron configuration.

Thus, the Hamiltonian is given by the three-orbital impurity extended Anderson model as

$$\mathcal{H} = \mathcal{H}_c + \mathcal{H}_f + \mathcal{H}_{\rm hyb}, \tag{5.11}$$

$$\mathcal{H}_c = \sum_{\mu=\Gamma_7,\Gamma_{81},\Gamma_{82}} \sum_{\vec{k},\sigma} \varepsilon_{\vec{k}} c^\dagger_{\mu\vec{k}\sigma} c_{\mu\vec{k}\sigma}, \tag{5.12}$$

$$\mathcal{H}_f = \sum_{\mu=\Gamma_7,\Gamma_{81},\Gamma_{82}} \sum_{\sigma} \varepsilon_f^{\Gamma_\mu} |f^1\Gamma_{\mu\sigma}\rangle\langle f^1\Gamma_{\mu\sigma}|$$
$$+ E_{\Gamma_1}|f^2\Gamma_1\rangle\langle f^2\Gamma_1| + \sum_{\alpha=0,\pm}(E_{\Gamma_1}+\eta)|f^2\Gamma_4^\alpha\rangle\langle f^2\Gamma_4^\alpha|, \tag{5.13}$$

$$\mathcal{H}_{\rm hyb} = \sum_{\mu=\Gamma_7,\Gamma_{81},\Gamma_{82}} \sum_{\vec{k}\sigma} \Big[V_\mu c^\dagger_{\mu\vec{k}\sigma} \Big\{ |f^0\rangle\langle f^1\Gamma_{\mu\sigma}|$$
$$+ |f^1\Gamma_\mu\rangle \left(\langle f^2\Gamma_1| + \sum_{\alpha=0,\pm}\langle f^2\Gamma_4^\alpha| \right) \Big\} + \text{h.c.} \Big], \tag{5.14}$$

where $c_{\mu\vec{k}\sigma}$ ($c^\dagger_{\mu\vec{k}\sigma}$) is the annihilation (creation) operator of the conduction electron with wave vector $\vec{k}$ hybridizing with the f-electron in the Γ_μ-orbital

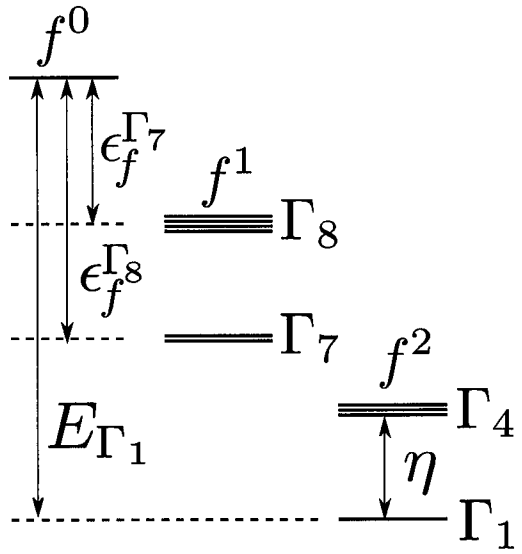

Figure 5.1: Energy level scheme of f-electron configurations due to the cubic CEF effect.

with strength V_μ. The Coulomb repulsion terms, such as the inter-orbital and the intra-orbital interactions, are implicitly included in the f^2-CEF energy levels, E_{Γ_1} and η.

To analyze properties of the system described by the Hamiltonian (5.11) on the basis of the Wilson NRG method [10], it is helpful for us that f^1- and f^2-states, eqs. (5.1)-(5.10), are expressed as the eigenstates of three conserved quantities: the total charge $Q^{\rm tot}$ relative to the half filling, the z-component of the total pseudospin $S_z^{\rm tot}$, and the total helicity $h^{\rm tot}$. Here, $h^{\rm tot}$ is a quantity similar to the angular momentum in C_{3v}, C_{4v} symmetry [8, 12] and defined as

$$h^{\rm tot} = \mathrm{mod}\left[\sum_{\mu=\Gamma_{81},\Gamma_{82}}\sum_{\sigma}\left(|f^1\Gamma_{\mu\sigma}\rangle\langle f^1\Gamma_{\mu\sigma}| + \sum_k c^\dagger_{\mu\sigma}c_{\mu\sigma}\right), 2\right]. \qquad (5.15)$$

In order to use $S_z^{\rm tot}$ as a conserved quantity, it is necessary to define the pseudospin states in Γ_{82}-orbital as $|\Gamma_{82\sigma}\rangle \equiv |1/2\bar{\sigma}\rangle$, and allot them fictitious $S_z^{\rm tot}$ as $\pm 3/2$. Table 5.1 shows the j-j coupling representation and conserved quantities of f^1- and f^2-states. We transform the conduction electron parts with a logarithmic discretization parameter, $\Lambda = 2.5$, into the one-dimensional semi-infinite chain model, and carry out the Wilson NRG method [10] by retaining up to 2500 states, confirming that there is no difference when retaining 3500

State	j-j coupling representation	$Q^{\rm tot}$	$h^{\rm tot}$	$2S_z^{\rm tot}$
$f^1\Gamma_{7\downarrow}$	$\|\downarrow,0,0\rangle$	-2	0	-1
$f^1\Gamma_{7\uparrow}$	$\|\uparrow,0,0\rangle$	-2	0	1
$f^1\Gamma_{81\downarrow}$	$\|0,\downarrow,0\rangle$	-2	1	-1
$f^1\Gamma_{81\uparrow}$	$\|0,\uparrow,0\rangle$	-2	1	1
$f^1\Gamma_{82\downarrow}$	$\|0,0,\downarrow\rangle$	-2	1	-3
$f^1\Gamma_{82\uparrow}$	$\|0,0,\uparrow\rangle$	-2	1	3
$f^2\Gamma_1$	$\frac{1}{\sqrt{6}}(2\|\uparrow\downarrow,0,0\rangle + \|0,\uparrow\downarrow,0\rangle - \|0,0,\uparrow\downarrow\rangle)$	-1	0	0
$f^2\Gamma_4^-$	$-\frac{1}{2}\|\downarrow,\downarrow,0\rangle + \frac{\sqrt{3}}{2}\|\uparrow,0,\downarrow\rangle$	-1	1	-2
$f^2\Gamma_4^0$	$\frac{1}{\sqrt{2}}(\|\uparrow,\downarrow,0\rangle + \|\downarrow,\uparrow,0\rangle)$	-1	1	0
$f^2\Gamma_4^+$	$\frac{1}{2}\|\uparrow,\uparrow,0\rangle - \frac{\sqrt{3}}{2}\|\downarrow,0,\uparrow\rangle$	-1	1	2

Table 5.1: The j-j coupling representation and conserved quantities of f^1- and f^2-states.

states. For simplicity, we set the density of state of conduction electrons of Γ_7 and Γ_8 symmetries to be constant with an extent from $-D$ to D measured from the Fermi level.

5.3 Ground State Phase Diagram

The ground state of the Hamiltonian (5.11) has already been analyzed by Hattori and Miyake [8], in particular for $V_7 = 0$. They concluded that there are two possible stable fixed points. One is the CEF singlet fixed point where the CEF singlet state is the ground state of the system, and the other is the triplet fixed point where the ground state is the triplet state. At the boundary between these two stable fixed points, there exists an unstable fixed point. However, it is natural to think that there exists a parameter region where the K-Y singlet state is the ground state of the system as hybridizations increase. To ascertain whether this idea is true, we investigate the ground state of the Hamiltonian (5.11) by varying V_7 and V_8 as control parameters with other parameters fixed as $E_{\Gamma_1} = -1.00$, $\eta = 0.02$, $\varepsilon_f^{\Gamma_7} = -0.50$, and $\varepsilon_f^{\Gamma_8} = -0.40$ in the unit of D. Throughout this chapter, we fix these parameters and measure all parameters in the unit of D.

Figure 5.2 shows the phase diagram of the ground state in the V_7-V_8 plane, which is determined by the low-energy spectrum obtained in the NRG calcula-

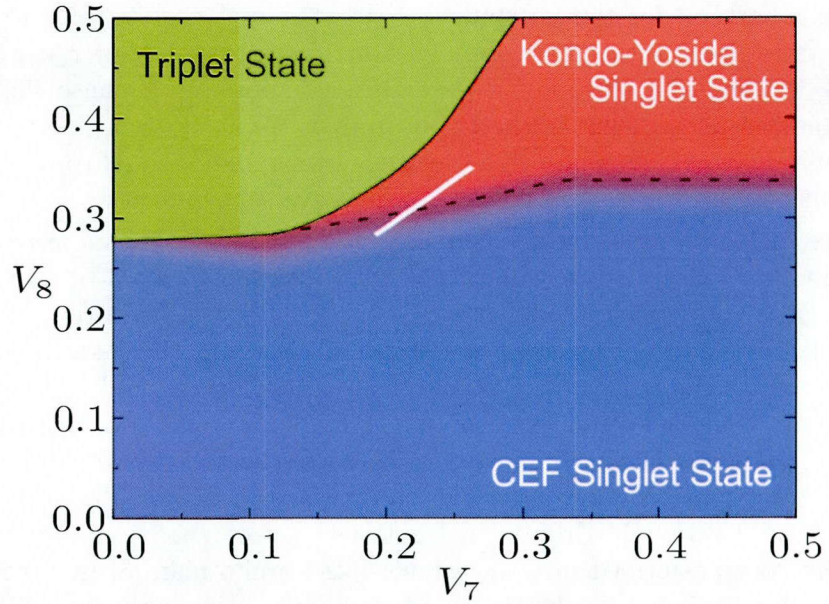

Figure 5.2: Schematic ground state phase diagram in V_7-V_8 plane for $E_{\Gamma_1} = -1.00$, $\eta = 0.02$, $\varepsilon_f^{\Gamma_7} = -0.50$, and $\varepsilon_f^{\Gamma_8} = -0.40$. The dotted line shows that two singlet states cross over smoothly. The white line shows the parameters along which we calculate the Sommerfeld coefficient as shown in Fig. 5.15.

tion. For $V_7 = 0$, the result is consistent with that in ref. 8, i.e., there are two possible ground states. One is the Γ_1 CEF singlet state where two f-electrons form the singlet state due to the cubic CEF effect. The other is the triplet state which is realized for $V_8 \geq 0.27$ because the level crossing between Γ_1 singlet and Γ_4 triplet states occurs due to the hybridization with conduction electrons of Γ_8 symmetry. At the boundary between these two stable fixed points, there exists an unstable fixed point where the non-Fermi liquid behavior appears in various physical quantities, which will be discussed later.

The level crossing between Γ_1 singlet and Γ_4 triplet states causes a remarkable change in the phase shift. In the NRG calculation, the phase shifts are underestimated because spectral functions do not reach the unitarity limit of $\pi\Gamma\rho_{m\sigma}(0) = 1$ where $\Gamma = \pi|V|^2\rho_0$ with $\rho_0 = 1/2D$, $\rho_{m\sigma}(\omega)$ being the single-particle spectral function for the orbital m and the spin σ component. However, the qualitative behavior of phase shifts is useful for understanding the properties of the system. Figure 5.3 shows the V_8-dependence of (a) the

phase shift in Γ_7-orbital for the up spin, $\delta_{7\uparrow}$, (b) that in Γ_8-orbitals for the up spin, $\delta_{8\uparrow}$, and (c) the total phase shift for the up spin, $\delta_\uparrow \equiv \delta_{7\uparrow} + \delta_{8\uparrow}$, for $V_7 = 0.2$, 0.3, 0.4, and 0.5. It is noted that $\delta_{8\uparrow}$ is composed of a phase shift in the Γ_{81}-orbital, $\delta_{81\uparrow}$, and that in the Γ_{82}-orbital, $\delta_{82\uparrow}$, i.e., $\delta_{8\uparrow} = \delta_{81\uparrow} + \delta_{82\uparrow}$, and $\delta_{81\uparrow}$ is equal to $\delta_{82\uparrow}$. The phase shifts for the down spin are equal to those for the up spin because the system holds the time-reversal symmetry.

In the case of $V_7 = 0$, $\delta_{8\uparrow}$ sharply increases at $V_8 = 0.35$ as V_8 increases, while $\delta_{7\uparrow}$ is almost equal to zero as shown in Fig. 5.3(a) and Fig. 5.3(b). This fact indicates that the triplet ground state is stabilized by the hybridization with the Γ_8-channel, and the effect of the hybridization with the Γ_7-channel is negligibly small at the triplet fixed point. Thus, the effective model at the triplet fixed point is given by the fact that the Γ_4 triplet state hybridizes with the conduction electrons of Γ_8 symmetry, which corresponds to the model in which an impurity spin 1 hybridizes with the quasispin 3/2, i.e., the multi-channel Kondo model with quadrupole interactions. In fact, the Hamiltonian, eq. (5.11), can be transformed into the Kondo-like Hamiltonian [8], and the non-Fermi liquid behavior occurs in various physical quantities in the low temperature region at the triplet fixed point [2, 8].

On the other hand, the increase of V_7 increases $\delta_{7\uparrow}$ for all values of V_8, as shown in Fig. 5.3(a). For $V_7 \geq 0.3$, the triplet state is not realized below $V_8 = 0.5$, and both $\delta_{7\uparrow}$ and $\delta_{8\uparrow}$ gradually increase as V_8 increases, which causes the gradual increase of δ, as shown in Fig. 5.3(c). Such a gradual change of phase shifts can be thought of as the signature of the ground state crossing over from the CEF singlet-like singlet state to the K-Y singlet-like singlet state as V_8 increases. In other words, the singlet state is the linear combination of the CEF singlet and the K-Y singlet states, and the weights of these singlet states change smoothly, although these two singlet states interchanges abruptly give rise to the unstable fixed point in tetragonal symmetry [3, 4, 5]. We can determine which singlet state gives a dominant contribution to the low-energy spectrum obtained in the NRG calculation if the parameter is far from the crossover region, and define two regions as shown in Fig. 5.2, i.e., the CEF singlet ground state region where the CEF singlet state gives a dominant contribution to the low energy spectrum, and the K-Y singlet ground state region where the K-Y singlet state gives a dominant contribution to the low energy spectrum. However, it is difficult to clearly distinguish the location of the crossover line at which the singlet state giving a dominant contribution to the low-energy spectrum interchanges between the CEF singlet state and the K-Y singlet state. In this sense, the dotted line in Fig. 5.2 has some ambiguity.

In particular, in the case of $V_7 = 0.5$, $\delta_{7\uparrow}$ gradually increases and reaches

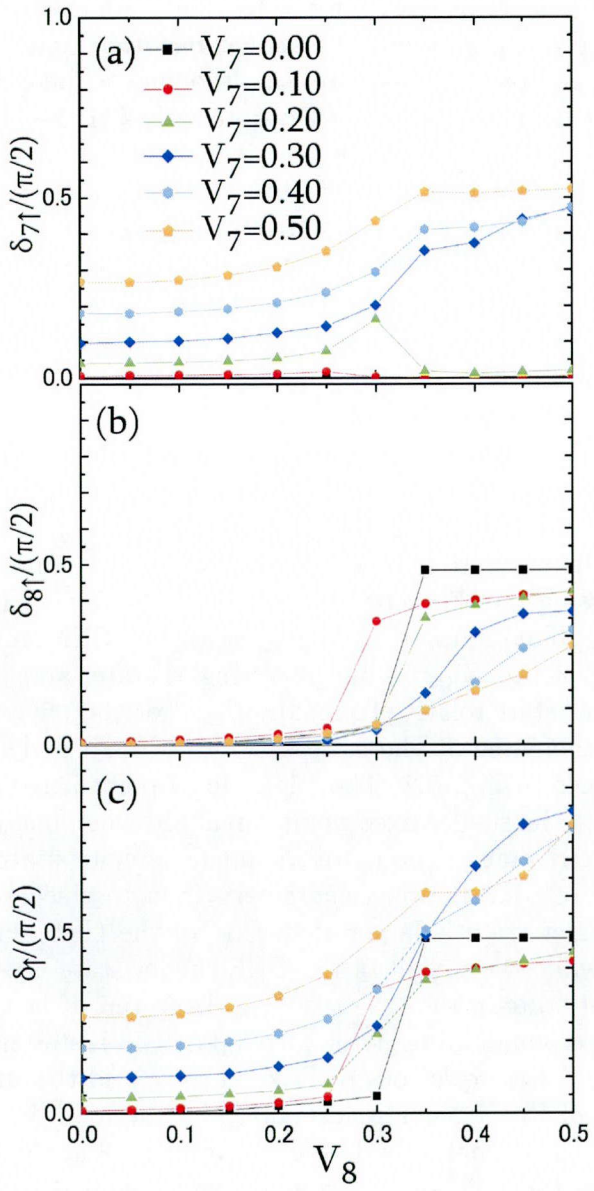

Figure 5.3: The V_8-dependence of (a) phase shift in Γ_7-orbital for up spin, $\delta_{7\uparrow}$, (b) that in Γ_8-orbital for up spin, $\delta_{8\uparrow}$, (c) the total phase shift for up spin, $\delta_\uparrow \equiv \delta_{7\uparrow} + \delta_{8\uparrow}$, for $V_7 = 0.2, 0.3, 0.4$, and 0.5. The phase shifts are underestimated because spectral functions do not reach the unitarity limit of $\pi\Gamma\rho(0) = 1$.

the constant value $\sim \pi/4$ as V_8 increases, while $\delta_{8\uparrow}$ is also gradually increasing. This fact may indicate that the K-Y singlet state can be formed in Γ_7 symmetry because $\delta_{7\uparrow}$ is not changed by an increase of V_8, although the ideal phase shift at the K-Y singlet fixed point $\delta = \pi/2$ is not obtained. On the other hand, the other K-Y singlet state may be about to form in Γ_8 symmetry because $\delta_{8\uparrow}$ increases as V_8 increases. It is notable that the K-Y singlet state in Γ_8 symmetry is different from that in Γ_7 symmetry, the so-called K-Y singlet state, because both Γ_{81}- and Γ_{82}-orbitals contribute to this singlet state in light of finite $\delta_{81\uparrow}$ and $\delta_{82\uparrow}$. Although the detailed form of this singlet state is unclear, we call this singlet state in Γ_8 symmetry as the K-Y singlet for the moment. The ideal total phase shift $\delta_\uparrow = \pi$ in the K-Y singlet ground state region may be composed of $\delta_{7\uparrow} = \pi/2$ and $\delta_{8\uparrow} = \pi/2$.

It is noted that for $V_7 \neq 0$, there always exists the K-Y singlet ground state region at the singlet fixed point near the boundary between the singlet fixed point and the triplet fixed point even though V_7 and V_8 are not so large. The reason why the K-Y singlet state is realized even for small V_7 and V_8 can be understood by considering the characteristic energy scales. The characteristic energy scales of each ground state are given by η for the CEF singlet state, the lower Kondo temperature $T_{\rm KL}$ for the K-Y singlet state, and the energy gain T_s in the Γ_4 triplet state relative to $\max(\eta, T_{\rm KL})$ for the triplet state. It is apparent that T_s is increased by the increase of V_8, while it is decreased by the increase of V_7 as seen in Fig. 5.2. The triplet fixed point is realized when $T_s > \max(T_{\rm KL}, \eta)$, while the singlet fixed point is realized when $\max(T_{\rm KL}, \eta) > T_s$. At the singlet fixed point region, the dominant singlet state can also be determined by the relation between characteristic energy scales, i.e., the weight of the K-Y singlet state is larger than that of the CEF singlet state in the case $\eta < T_{\rm KL}$, while the weight of the CEF singlet state is larger than that of the K-Y singlet state in the case $\eta > T_{\rm KL}$. However, at the boundary between the singlet fixed point and the triplet fixed point, Γ_4 is stabilized by the hybridization with conduction electrons of Γ_8 symmetry, and the energy level of Γ_4 approaches that of Γ_1, i.e., η is renormalized by the hybridization with conduction electron of Γ_8 symmetry, and becomes very small at the boundary. In the case of $V_7 = 0$, the K-Y singlet ground state region does not occur because the lower Kondo temperature (that of Γ_7-orbital) is exactly equal to zero, i.e., $0 = T_{\rm KL} < \max(\eta, T_s)$. However, for $V_7 \neq 0$, $T_{\rm KL}$ becomes finite, and there always exists the region satisfying the relation $T_{\rm KL} > \max(\eta, T_s)$, where the K-Y singlet ground state is realized because of the renormalization of η at the boundary between two fixed points.

Thus, the Hamiltonian eq. (5.11) has two fixed points, the triplet fixed

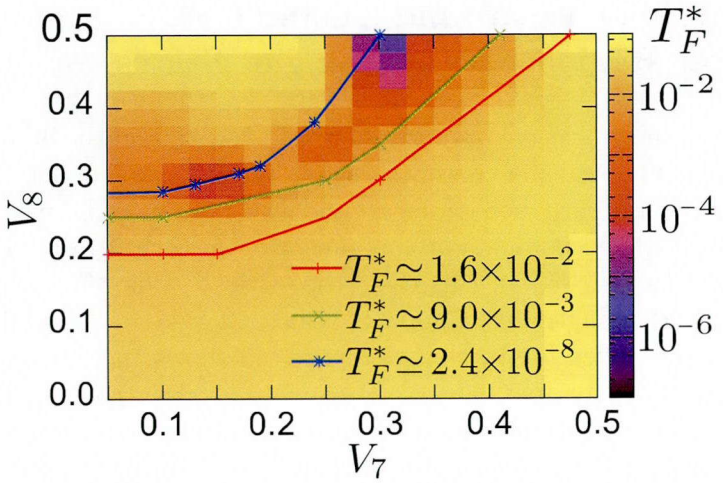

Figure 5.4: Characteristic temperature $T_{\rm F}^*$ for V_7-V_8 plane for $E_{\Gamma_1} = -1.00$, $\eta = 0.02$, $\varepsilon_f^{\Gamma_7} = -0.50$, and $\varepsilon_f^{\Gamma_8} = -0.40$. At the boundary between the triplet fixed point and the K-Y singlet fixed point, $T_{\rm F}^*$ is suppressed compared to the characteristic energy scale of each fixed point $\sim \eta = 0.02$.

point and the singlet fixed point, and the singlet state is a linear combination of two singlet states, the CEF singlet state and the K-Y singlet state. We estimate the characteristic temperature $T_{\rm F}^*$ as shown in Fig. 5.4, where $T_{\rm F}^*$ is defined as the temperature at which the temperature derivative of an entropy, $\partial S_{\rm imp}(T)/\partial(\log T)$, reaches a maximum value as $S_{\rm imp}(T)$ approaches zero as $T \to 0$. At the boundary between the triplet fixed point and the singlet fixed point, $T_{\rm F}^*$ is drastically suppressed, which indicates that there exists an unstable fixed point giving the non-Fermi liquid behaviors in various physical quantities, as will be discussed in the next section. On the other hand, around the crossover region between the K-Y singlet state and the CEF singlet state, $T_{\rm F}^*$ monotonically increases as V_8 increases, although $T_{\rm F}^*$ is remarkably suppressed at the boundary between the CEF singlet state and the K-Y singlet state in the case of tetragonal symmetry [3, 4, 5]. This fact also indicates that the K-Y singlet state and the CEF singlet state cross over smoothly in cubic symmetry.

5.4 Physical Behavior around Unstable Fixed Point and Crossover Region between Singlet States

It is interesting to see how physical properties are affected around the boundary between two fixed points and the crossover region between two singlet states. First, we discuss the physical behaviors around the boundary between the singlet and the triplet fixed points. For this purpose, we vary V_8 as a control parameter for fixed $V_7 = 0.25$. In this case, the critical value of V_8 is given as $V_{8c} \simeq 0.385$, i.e., the singlet fixed point is realized for $V_8 < V_{8c}$ while the triplet fixed point is realized for $V_8 > V_{8c}$. Figure 5.5 shows the entropy due to an impurity, $S_{\rm imp}(T)$, for five values of $V_8 = 0.32$, 0.36, 0.38, 0.40, and 0.50. The characteristic temperature for the present parameters are given as $T_{\rm F}^* \sim 5.85\times10^{-3}$ for $V_8 = 0.32$, $T_{\rm F}^* \sim 4.56\times10^{-5}$ for $V_8 = 0.36$, $T_{\rm F}^* \sim 1.22\times10^{-7}$ for $V_8 = 0.38$, $T_{\rm F}^* \sim 2.05 \times 10^{-2}$ for $V_8 = 0.40$, and $T_{\rm F}^* \sim 6.03 \times 10^{-2}$ for $V_8 = 0.50$. At both fixed points, the closer V_8 approaches V_{8c}, the more $T_{\rm F}^*$ is suppressed. At the triplet fixed point, $V_8 = 0.40$ and 0.50, $S_{\rm imp}(T)$ takes the value $S_{\rm imp}(T \to 0) \sim 0.75 k_{\rm B} \log 2$ as T decreases. When the number of states remaining in the NRG calculation increases up to 3500, $S_{\rm imp}(T \to 0)$ approaches a value of $k_{\rm B} \log 2$, which is consistent with the value obtained in ref. 8, although the meaning of this value is unclear. On the other hand, at the singlet fixed point, $V_8 < V_{8c}$, $S_{\rm imp}(T)$ merges into the same value of $0.75 k_{\rm B} \log 2$ and approaches zero around $T_{\rm F}^*$ as T decreases near the unstable fixed point, $V_8 = 0.38$ and 0.36, while it immediately approaches zero for $V_8 = 0.32$, away from the unstable fixed point.

We estimate the Sommerfeld coefficient $\gamma_{\rm imp}(T) \equiv C_{\rm imp}(T)/(k_{\rm B}^2 T)$, as shown in Fig. 5.6. At the singlet fixed point, as T decreases, it is a common feature that $\gamma_{\rm imp}(T)$ shows a logarithmic increase, and approaches the saturated value, i.e., recovers the Fermi liquid behavior, at $T < T_{\rm F}^*$. It is apparent that the saturated value of $\gamma_{\rm imp}(T \to 0)$ decreases as the deviation from V_{8c} increases at the singlet fixed point. On the other hand, at the triplet fixed point, $\gamma_{\rm imp}(T)$ takes the saturated value in the temperature range, $10^{-4} \lesssim T \lesssim 10^{-2}$, and increases logarithmically as T decreases. This logarithmic increase in the low temperature region is caused by the non-Fermi liquid fixed point due to the quadrupole interactions [2, 8]. Figure 5.7 shows the V_8-dependence of $\gamma_{\rm imp}(T)$ for various temperatures. At the singlet fixed point, the increase of $\gamma_{\rm imp}(T)$ stops at each $T_{\rm F}^* > 0$, while it stops increasing at $T \simeq 10^{-2}$ and again starts to increase at $T \simeq 10^{-6}$ at the triplet fixed point. At the unstable fixed point, the increase of $\gamma_{\rm imp}(T)$ does not stop down to $T \to 0$. As a result, $\gamma_{\rm imp}(T)$ takes a peak structure at the unstable fixed point in the low temperature region.

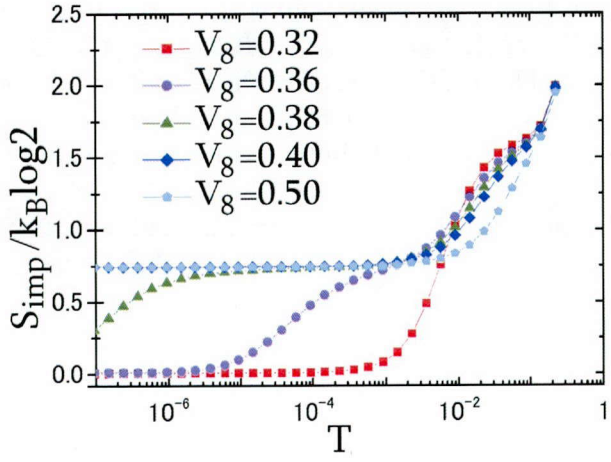

Figure 5.5: Temperature dependence of the entropy due to the impurity $S_{\rm imp}(T)$ for V_8=0.32, 0.36, 0.38, 0.40, and 0.50 with other parameters fixed as $E_{\Gamma_1} = -1.00$, $\eta = 0.02$, $\varepsilon_f^{\Gamma_7} = -0.50$, $\varepsilon_f^{\Gamma_8} = -0.40$, and $V_7 = 0.25$.

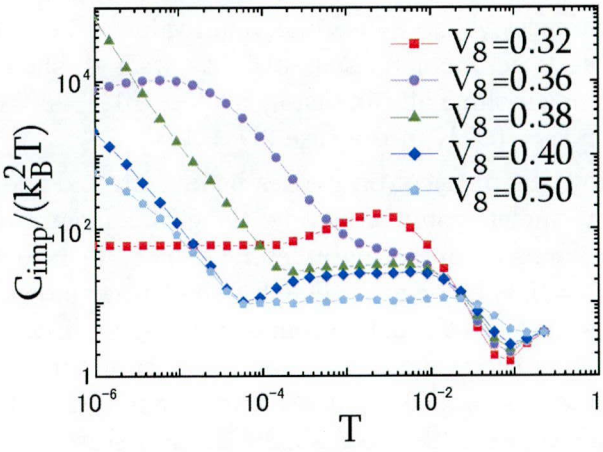

Figure 5.6: Temperature dependence of the Sommerfeld coefficient $\gamma_{\rm imp}(T) \equiv C_{\rm imp}(T)/T$ for V_8=0.34, 0.36, 0.38, 0.40, and 0.42. Other parameters are the same as those in Fig. 5.5.

In Fig. 5.13, the frequency dependence of the total scattering rate $1/\tau(\omega)$ at $T = 0$ is shown, where $1/\tau(\omega)$ is the sum of contributions from each orbital m and spin σ component $1/\tau_{m\sigma}(\omega) = 2\pi|V_m|^2\rho_{m\sigma}(\omega)$, $\rho_{m\sigma}(\omega)$ being the single-particle spectral function. The T-dependence of the resistivity can be inferred from $1/\tau(\omega)$. It is a common feature that there is peak at $\omega \sim 2 \times 10^{-2}$. At both fixed points, these peaks are contributed to by the hybridization with conduction electrons of Γ_8 symmetry as shown in Fig. 5.9, which shows the contribution from each channel μ, $1/\tau_\mu(\omega)$, to $1/\tau(\omega)$ for $V_8 = 0.32$ (the singlet fixed point), and $V_8 = 0.50$ (the triplet fixed point). At the singlet fixed point, $1/\tau(\omega)$ increases logarithmically and takes the saturated value at $\omega \sim T_{\rm F}^*$. As seen in Fig. 5.9 for $V_8 = 0.5$, such a behavior in low-ω region comes from $1/\tau_7$. On the other hand, at the triplet fixed point, after having the peak at $\omega \sim 10^{-1}$, $1/\tau(\omega)$ decreases as ω decreases. Figure. 5.9 shows that $1/\tau$ at the triplet fixed point is contributed to only from $1/\tau_8$, and $1/\tau_7$ does not contribute. These results indicate that the triplet fixed point disturbs the hybridization with conduction electrons of Γ_7 symmetry.

Figure 5.10 shows the V_8-dependence of $\chi_M^0 \equiv \lim_{\omega\to 0}{\rm Im}\ \chi_M(\omega)$, which infers the static susceptibility in the limit $T \to 0$. At the triplet fixed point, χ_M^0 takes values of the order of $O(10^4)$ because of the non-Fermi liquid fixed point due to the quadrupole interactions in the low temperature region. On the other hand, at the singlet fixed point, χ_M^0 increases drastically as the system approaches the unstable fixed point $V_8 \to V_{8c}$. It is noted that at an observable temperature range, we expect χ_M^0 to take a maximum value at $V_8 = 0.38 \simeq V_{8c}$ because the increase of static magnetic susceptibility start to show the non-Fermi liquid behavior (logarithmically increase) at $T \simeq 10^{-4}$ as T decreases, where $10^{-4}D$ corresponds to 0.5 K in the case 2D = 1eV.

Next, we discuss how the physical properties behave around the crossover region between the K-Y singlet ground state and the CEF singlet ground state regions. We also vary V_8 as a control parameter for fixed $V_7 = 0.5$. In this case, we ensure that $V_8 = 0.30$ belongs to the CEF singlet ground state region while $V_8 = 0.35$ belongs to the K-Y singlet ground state region, i.e., the ground state region crosses over in the range of $0.30 < V_8 < 0.35$. Figure 5.11 shows $S_{\rm imp}(T)$ for $V_8 = 0.2$, 0.3, 0.4, and 0.5. In tetragonal symmetry, there exists the unstable fixed point between the K-Y singlet ground state and the CEF singlet ground state regions, giving the residual entropy $0.5k_{\rm B}\log 2$ [3, 4, 5]. However, in cubic symmetry, we do not obtain parameters which show such a residual entropy between $V_8 = 0.30$ and $V_8 = 0.40$ in cubic symmetry. In the K-Y singlet ground state region, $V_8 > 0.40$, the temperature at which $S_{\rm imp}$ becomes to zero decreases with a decrease of $T_{\rm F}^*$. This is because the

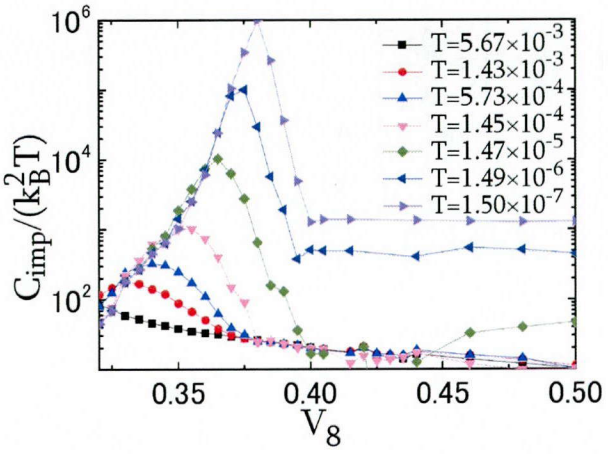

Figure 5.7: V_8-dependence of $\gamma_{\rm imp}(T)$ for various temperatures. The fixed point switch at $V_8 = V_{8c} \simeq 0.385$ from the K-Y singlet fixed point for $V_8 < V_{8c}$ to the triplet fixed point for $V_8 > V_{8c}$. Other parameters are the same as those in Fig. 5.5.

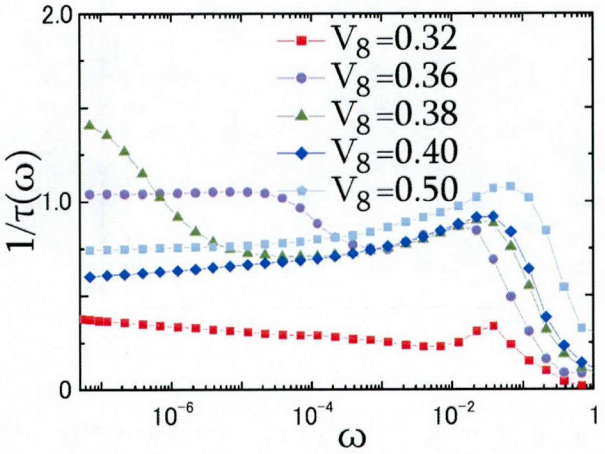

Figure 5.8: Frequency dependence of the scattering rate $1/\tau(\omega)$ for V_8=0.34, 0.36, 0.38, 0.40, and 0.42. Other parameters are the same as those in Fig. 5.5.

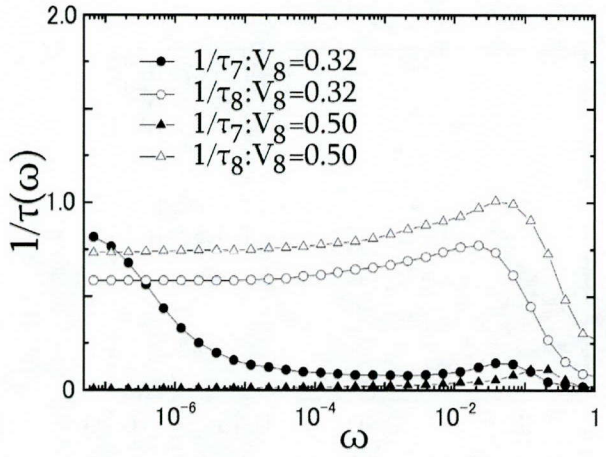

Figure 5.9: Contribution of each channel $1/\tau_7(\omega)$ (filled symbols) and $1/\tau_8(\omega)$ (open symbols) for V_8=0.32 (circles: the K-Y singlet fixed point) and 0.50 (triangles: the triplet fixed point). Other parameters are the same as those in Fig. 5.5.

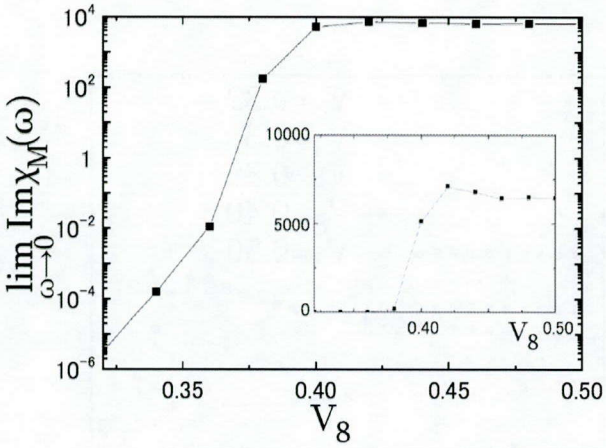

Figure 5.10: V_8-dependence of $\lim_{\omega\to 0}\mathrm{Im}\ \chi(\omega)$ on a logarithmic scale. Inset shows the same figure on normal scale. The fixed point switch at $V_8 = V_{8c} \simeq 0.385$ from the K-Y singlet fixed point for $V_8 < V_{8c}$ to the triplet fixed point for $V_8 > V_{8c}$. Other parameters are the same as those in Fig. 5.5.

boundary between the singlet fixed point and the triplet fixed point comes by as V_8 increases, as seen in Fig. 5.2.

Figure 5.12 shows the Sommerfeld coefficient $\gamma_{\rm imp}(T)$. As a common feature, $\gamma_{\rm imp}(T)$ shows the Schottky peak corresponding to the release of the entropy of the Γ_4 triplet state at $T \sim 10^{-2}$, and approaches a saturated value as T decreases. As V_8 increases, $\gamma_{\rm imp}(T \to 0)$ increases because $T_{\rm F}^*$ is suppressed due to the effect of competition between the singlet fixed point and the triplet fixed point.

In Fig. 5.13, the frequency dependence of the total scattering rate $1/\tau(\omega)$ at $T = 0$ is shown, and Fig. 5.13 shows the contribution from each channel μ, $1/\tau_\mu(\omega)$, to $1/\tau(\omega)$ for $V_8 = 0.20$ (the CEF singlet ground state region) and $V_8 = 0.50$ (the K-Y singlet ground state region). As in the previous case, it is a common feature that $1/\tau(\omega)$ shows the logarithmic increase at $0.1 \lesssim \omega < 1$ and takes a peak corresponding to the higher Kondo temperature of Γ_8 symmetry. It is clearly seen that contributions from both orbitals increase for all ω as V_8 increases, although there are no fundamental changes in the properties of the ground state, i.e., the singlet state is the linear combination of the CEF singlet state and the K-Y singlet state, and the weights of these single states are changed by the effect of hybridizations. This is why the residual scattering rate $1/\tau_0$ is not equal to zero even in the CEF singlet ground state region, and $1/\tau_0$ gradually increases as V_8 increases.

5.5 Discussion of Experiment on $U_{1-x}T_xBe_{13}$

It is interesting to note that $T_{\rm F}^*$ is affected by competition between the singlet fixed point and the triplet fixed point. Thus, we obtain the suppression of $T_{\rm F}^*$ if the system passes near the unstable fixed point in the singlet fixed point region. In Fig. 5.15, we show $\gamma_{\rm imp}(T)$ when we vary two parameters V_7 and V_8 simultaneously on the line from $V \equiv (V_7, V_8) = (0.26.0.35)$ to $(0.19, 0.28)$ for various temperatures, as shown in white line in Fig. 5.2. Here, the singlet fixed point is realized for all the parameters along this line. For all V, $\gamma_{\rm imp}(T)$ increases monotonically as T decreases. At $V^* = (0.23, 0.35)$, $\gamma_{\rm imp}$ continues to increase down to $T_{\rm F}^*(V^*) = 2.12 \times 10^{-7}$, while the increase of $\gamma_{\rm imp}(T)$ stops around each $T_{\rm F}^*(V) > T_{\rm F}^*(V^*)$ at $V \neq V^*$. Thus, $\gamma_{\rm imp}(T)$ has the enhanced part from the background part at $|V - V^*| > V^*$ due to competition between the singlet fixed point and the triplet fixed point, where the background part is approximately given by the inverse of $T_{\rm KL}$ or η.

Here, we take $V \equiv (V_7, V_8)$ as a control parameter. However, we can expect similar behavior of $\gamma_{\rm imp}(T)$ in the real system by the effect of the pres-

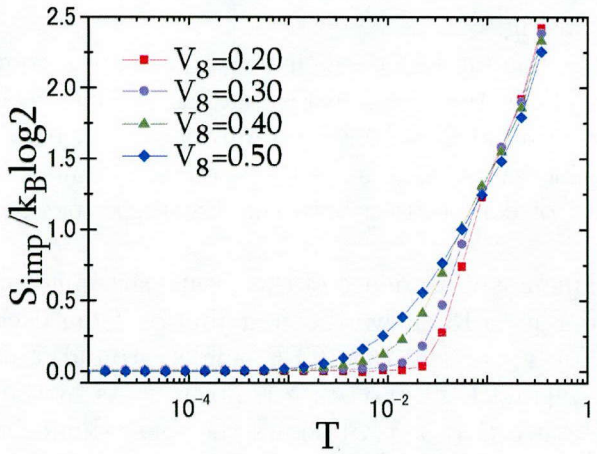

Figure 5.11: Temperature dependence of entropy due to the impurity $S_{\rm imp}(T)$ for V_8=0.2, 0.3, 0.4, and 0.5 with other parameters fixed as $E_{\Gamma_1} = -1.00$, $\eta = 0.02$, $\varepsilon_f^{\Gamma_7} = -0.50$, $\varepsilon_f^{\Gamma_8} = -0.40$, and $V_7 = 0.5$.

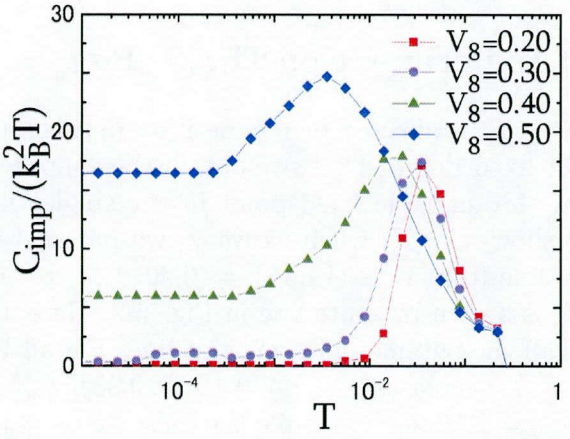

Figure 5.12: Temperature dependence of the Sommerfeld coefficient $\gamma_{\rm imp}(T) \equiv C_{\rm imp}(T)/T$ for V_8=0.2, 0.3, 0.4, and 0.5. Other parameters are the same as those in Fig. 5.11.

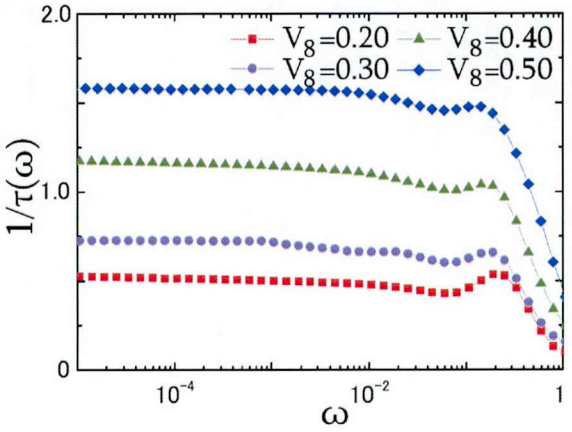

Figure 5.13: Frequency dependence of the scattering rate $1/\tau(\omega)$ for V_8=0.2, 0.3, 0.4, and 0.5. Other parameters are the same as those in Fig. 5.11.

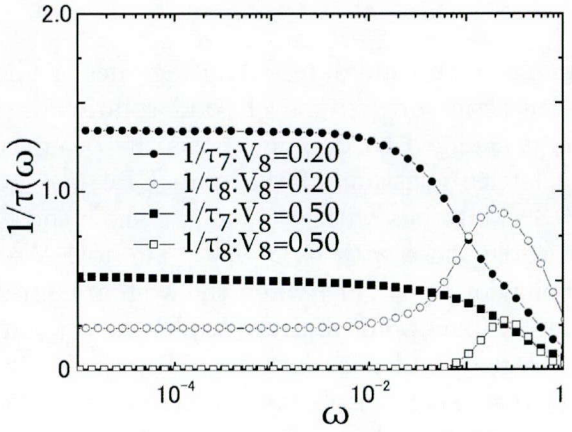

Figure 5.14: Contribution of each channel $1/\tau_7(\omega)$ (filled symbols) and $1/\tau_8(\omega)$ (open symbols) for V_8=0.20 (circles: the CEF singlet fixed point) and 0.50 (squares: the K-Y singlet fixed point). Other parameters are the same as those in Fig. 5.11.

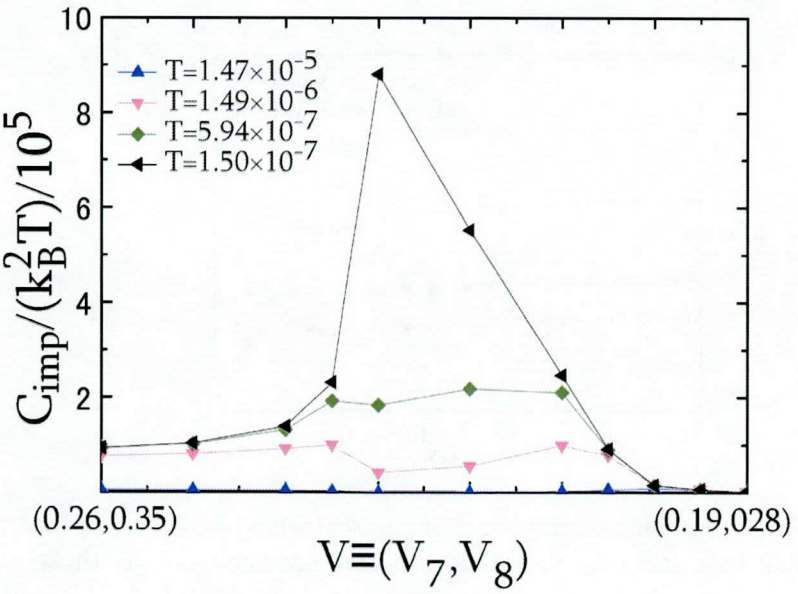

Figure 5.15: $V \equiv (V_7, V_8)$ dependence of the Sommerfeld coefficient where V varies on the line from $V = (0.12, 0.24)$ to $(0.36, 0.48)$ for various temperatures.

sure or the chemical doping. One candidate exhibiting such a phenomenon would be UBe_{13} because a series of systems of solid solution $U_{1-x}T_xBe_{13}$, whose lattice constant a_0 is changed by doping, shows the peak structure in $\lim_{T\to 0} C_{\rm imp}(T)/T$ at the lattice constant of the pure UBe_{13}, $a_{UBe_{13}}$ [13] as shown in Fig. 3.10 in §3.3. Materials with $a_0 < a_{UBe_{13}}$ show the Kondo-like upturn in the resistivity, while those with $a_0 > a_{UBe_{13}}$ do not. We can qualitatively reproduce the behavior of $\gamma_{\rm imp}(T)$ when the system comes near the boundary between the singlet fixed point and the triplet fixed point from the K-Y singlet ground state region, and goes into the CEF singlet fixed point, although we did not reproduce such an obvious change of the resistivity in our calculation. Because our treatment is restricted to the level of the impurity model, it is necessary to adopt the dynamical mean approach in order to discuss the lattice heavy fermion systems. However, the effect of competition between the singlet and the triplet fixed point possibly plays an important role in initiating such an anomalous phenomena. We leave it for the future study to determine whether the present model can reproduce a magnetically robust non-Fermi liquid behavior, $C_{\rm imp}(T)/T \sim -\log T$ up to 12 Tesla observed in

the pure UBe_{13} [14], as shown in Fig. 3.12.

5.6 Conclusion

We have investigated the properties of the f^2-configuration impurity system with the f^2-CEF level scheme of Γ_1-Γ_4 symmetry hybridizing with Γ_7 and Γ_8 conduction bands on the basis of the numerical renormalization group (NRG) method. When the strength of hybridizations between f-electrons and the Γ_7 and Γ_8 conduction bands, V_7 and V_8, are varied with a fixed CEF level scheme, there are two possible fixed points: one is the singlet fixed point, the other is the triplet fixed point because the Γ_4 first excited triplet state is stabilized due to the hybridization with conduction electrons with V_8 symmetry. The singlet state is the linear combination of the CEF singlet state and the K-Y single state, and the CEF singlet ground state region where the CEF singlet is the dominant component crosses smoothly over with the K-Y singlet ground state region where the K-Y singlet is the dominant component, although it has been shown that these two singlet state interchanges and their competition gives rise to an unstable fixed point in the case of tetragonal symmetry [2, 4, 5]. Moreover, the unstable fixed point is caused by competition between the singlet fixed point and the triplet fixed point, giving rise to the non-Fermi liquid behavior in various physical quantities such as the Sommerfeld coefficient, the resistivity, and the magnetic susceptibility. From these results, we have obtained a schematic phase diagram of the ground state, which has a parameter region reproducing the experimental result that the lattice constant of UBe_{13} gives the maximum Sommerfeld coefficient among a series of systems of solid solution $U_{1-x}T_xBe_{13}$. This result possibly provides us with the basis to understand the anomalous behaviors of UBe_{13}.

Bibliography of Chapter 5

[1] Y. Shimizu, O. Sakai, and Y. Kuramoto: Physica B **206-207** (1995) 135.

[2] A. Koga, G. Zaránd and D. L. Cox: Phys. Rev. Lett. **88** (1999) 2421.

[3] S. Yotsuhashi, K. Miyake, and H. Kusunose: J. Phys. Soc. Jpn. **71** (2002) 389.

[4] S. Nishiyama, H. Matsuura, and K. Miyake: J. Phys. Soc. Jpn. **79** (2010) 104711.

[5] S. Nishiyama and K. Miyake: J. Phys. Soc. Jpn. **80** (2011) 124706.

[6] R. Shiina and Y. Aoki: J. Phys. Soc. Jpn. **73** (2004) 541.

[7] J. Otsuki, H. Kusunose, and Y. Kuramoto: J. Phys. Soc. Jpn. **74** (2005) 389.

[8] K. Hattori and K. Miyake: J. Phys. Soc. Jpn **74** (2005) 2193.

[9] S. Hoshino, J. Otsuki, and Y. Kuramoto: J. Phys. Soc. Jpn. **78** (2009) 074719.

[10] K. G. Wilson: Rev. Mod. Phys. **47** (1975) 773.

[11] H. Harima and K. Takegahara: Physica B **312-313** (2002) 843.

[12] A. L. Moustakas and D. S. Fisher: Phys. Rev. B **55** (1997) 6832.

[13] J. S. Kim, B. Andraka, C. S. Jee, S. B. Roy, and G. R. Stewart: Phys. Rev. B **41** (1990) 11073.

[14] P. Gegenwart, C. Langhammer, R. Helfrich, N. Oeschler, M. Land, J. S. Kim, G. R. Stewart, and F. Steglich: Physica. C **408-410** (2004) 157-160.

Appendix A

Numerical Renormalization Group Method

We introduce Wilson's Numerical Renormalization Group (NRG) method for taking the single impurity Anderson model. At first, the NRG method was developed by K. G. Wilson for the Kondo model. Considering that the Kondo model is derived from the Anderson model by the second perturbation theory, it is easily understood that the Kondo model corresponds to the model that we restrict the charge degree of freedom of an impurity site to 1 (i.e., $n_{d\uparrow}+n_{d\downarrow}=1$). After the first application of the NRG method by K. G. Wilson, the NRG method was also applied to the Anderson model.

In our researches, we extend this NRG method for the Anderson model to multi-orbital cases with assuming that the density of state of the conduction electron is constant in the energy range from $-D$ to D. Here, for the single impurity Anderson model, we introduce the NRG method which is extended to the case where the density of state of conduction bands moderately changes at around Fermi energy.

A.1 Transformation of Hamiltonian

In our researches, targets are heavy fermion systems. Heavy fermion systems commonly have f-electrons which have the relatively well-localized character compared to other electrons. This character allows us to treat the f-electron as the localized electron in the Anderson model. Actually, the Anderson model is often used to discuss the properties of dilute heavy fermion systems, and gives an important insight for heavy fermion systems. Thus, in this section,

we take the localized electron as the f-electron in the Anderson model.

$$\mathcal{H} = \mathcal{H}_c + \mathcal{H}_{\rm hyb} + \mathcal{H}_f, \tag{A.1.1}$$

$$\mathcal{H}_c = \sum_{\vec{k}\sigma} \varepsilon_{\vec{k}} c^\dagger_{\vec{k}\sigma} c_{\vec{k}\sigma}, \tag{A.1.2}$$

$$\mathcal{H}_{\rm hyb} = \sum_{\vec{k}\sigma} \left[V_{\vec{k}} f^\dagger_\sigma c_{\vec{k}\sigma} + {\rm h.c.} \right], \tag{A.1.3}$$

$$\mathcal{H}_f = \sum_\sigma \varepsilon_f f^\dagger_\sigma f_\sigma + U n_{f\uparrow} n_{f\downarrow}, \tag{A.1.4}$$

where $f_\sigma (f^\dagger_\sigma)$ and $c_{\vec{k}\sigma} (c^\dagger_{\vec{k}\sigma})$ are annihilation (creation) operators of the f-electron with the energy ε_f and the conduction electrons with the kinetic energy $\varepsilon_{\vec{k}}$ which hybridize with the f-electron with the strength $V_{\vec{k}}$. Here, each annihilation and creation operator obeys the following anti-commutation rules:

$$\{c^\dagger_{\vec{k}\sigma}, c_{\vec{k}'\sigma'}\} = \delta_{\vec{k},\vec{k}'} \delta_{\sigma,\sigma'}, \tag{A.1.5}$$

$$\{c_{\vec{k}\sigma}, c_{\vec{k}'\sigma'}\} = 0, \tag{A.1.6}$$

$$\{f^\dagger_\sigma, f_{\sigma'}\} = \delta_{\sigma,\sigma'}, \tag{A.1.7}$$

$$\{f_\sigma, f_{\sigma'}\} = 0. \tag{A.1.8}$$

A.1.1 Mapping on Semi-Infinite Chain Form

First, we transform the Hamiltonian eq. (A.1.1) into a semi-infinite chain form by rewriting the wave-functions written by the plane wave to one written by the spherical wave. Here, we skip the subscript about spin for the simplicity. The operator of conduction electrons can be written in the plane wave and the spherical wave representations as follow.

$$\varphi(\vec{r}) = \frac{1}{\sqrt{\Omega}} \sum_{\vec{k}} e^{i\vec{k}\cdot\vec{r}} c_{\vec{k}} = \sum_{klm} \psi_l(kr) Y_{lm}(\Omega_{\vec{r}}) c_{klm}, \tag{A.1.9}$$

$$\psi_l(kr) = \sqrt{\frac{2k^2}{R}} j_l(kr), \tag{A.1.10}$$

where $\Omega \equiv 4\pi R^3/3$ is the volume of the system, $\psi_l(kr)$ the radial wave function normalized within the sphere with the radius R, $j_l(kr)$ the spherical Bessel function of l-th kind, and $Y_{lm}(\Omega_{\vec{r}})$ the spherical surface harmonics. The plane wave is represented by the spherical wave as following.

$$e^{i\vec{k}\cdot\vec{r}} = \sum_{lm} 4\pi i^l j_l(kr) Y^*_{lm}(\Omega_{\vec{k}}) Y_{lm}(\Omega_{\vec{r}}). \tag{A.1.11}$$

Substituting eq. (A.1.11) into eq. (A.1.9), and using the orthonormal condition of the radial wave function and the spherical surface harmonics, we obtain the relation between the plane wave and the spherical wave representations.

$$c_{\vec{k}} = \frac{\sqrt{6\pi}}{kR} \sum_{lm} i^{-l} Y_{lm}(\Omega_{\vec{k}}) c_{klm}, \tag{A.1.12}$$

$$c_{klm} = \frac{kR}{\sqrt{6\pi}} \int \mathrm{d}\Omega_{\vec{k}} i^{l} Y^{*}_{lm}(\Omega_{\vec{k}}) c_{\vec{k}}. \tag{A.1.13}$$

The hybridization $V_{\vec{k}}$ is also written both in the plane wave and the spherical wave representations as

$$\frac{1}{\sqrt{\Omega}} \sum_{\vec{k}} e^{i\vec{k}\cdot\vec{r}} V_{\vec{k}} = \sum_{klm} \psi_l(kr) Y_{lm}(\Omega_{\vec{r}}) V_{klm}. \tag{A.1.14}$$

Substituting eq. (A.1.11) into eq. (A.1.14), we also obtain the following relations about the hybridization $V_{\vec{k}}$.

$$V_{\vec{k}} = \sqrt{4\pi} \sum_{lm} i^{-l} Y_{lm}(\Omega_{\vec{k}}) V_{klm}, \tag{A.1.15}$$

$$V_{klm} = \frac{1}{\sqrt{4\pi}} \int \mathrm{d}\Omega_{\vec{k}} i^{l} Y^{*}_{lm}(\Omega_{\vec{k}}) V_{\vec{k}}. \tag{A.1.16}$$

Using eqs. (A.1.12), (A.1.13), (A.1.15) and (A.1.16), we derive the semi-infinite chain form from the Hamiltonian eq. (A.1.1). Substituting eqs. (A.1.12) and (A.1.15) into eq. (A.1.3), the hybridization term is transformed as following.

$$\begin{aligned}
\sum_{\vec{k}} V_{\vec{k}} c^{\dagger}_{\vec{k}} &= \frac{\Omega}{(2\pi)^3} \int \mathrm{d}\vec{k} V_{\vec{k}} c^{\dagger}_{\vec{k}} \\
&= \sqrt{\frac{\Omega k_{\mathrm{F}}^3}{(2\pi)^3}} \sqrt{4\pi} \int \mathrm{d}k k \sum_{lm} \left(\sqrt{\frac{k_{\mathrm{F}} R}{\pi}} c^{\dagger}_{klm} \right) V_{klm} \\
&= \sqrt{\frac{\Omega k_{\mathrm{F}}^3}{(2\pi)^3}} \sqrt{4\pi} \int \mathrm{d}q q \sum_{lm} c^{\dagger}_{qlm} V_{klm},
\end{aligned} \tag{A.1.17}$$

where $q \equiv k/k_{\mathrm{F}}$ and $c^{\dagger}_{qlm} \equiv \sqrt{\frac{k_{\mathrm{F}} R}{\pi}} c^{\dagger}_{klm}$. Here, c_{qlm} also obey the following anti-commutation rule.

$$\{c^{\dagger}_{qlm}, c^{\dagger}_{q'l'm'}\} = 0, \tag{A.1.18}$$

$$\{c^{\dagger}_{qlm}, c_{q'l'm'}\} = \delta_{q,q'} \delta_{l,l'} \delta_{m,m'}. \tag{A.1.19}$$

In the same manner, the kinetic energy term of conduction electrons, eq. (A.1.2) is transformed as following.

$$\sum_{\vec{k}} \varepsilon_{\vec{k}} c^{\dagger}_{\vec{k}\sigma} c_{\vec{k}\sigma} = \int \mathrm{d}q \sum_{lm} \varepsilon(k_{\mathrm{F}} q) c^{\dagger}_{qlm} c_{qlm}. \tag{A.1.20}$$

Here, we assume that the conduction band extends from $-D$ to D in the energy range. We measure these two terms in a unit of D.

$$\bar{\mathcal{H}}_c \equiv \mathcal{H}_c/D = \int_{-D}^{D} \mathrm{d}\varepsilon_q \frac{\varepsilon_q}{D} \left(\frac{\mathrm{d}q}{\mathrm{d}\varepsilon}\right) c^{\dagger}_{qlm} c_{qlm}, \tag{A.1.21}$$

$$\bar{\mathcal{H}}_{\mathrm{hyb}} \equiv \mathcal{H}_{\mathrm{hyb}}/D = \sqrt{\frac{4\pi\Omega k_{\mathrm{F}}^3}{(2\pi)^3}} \int \mathrm{d}\varepsilon_q q \frac{\mathrm{d}q}{\mathrm{d}\varepsilon_q} \left[\frac{V_{qlm}}{D} c^{\dagger}_{qlm} f + h.c.\right] \tag{A.1.22}$$

In general, l and m-components of conduction electrons couple with the impurity site as seen in eq. (A.1.22). Here, we drop off the conduction electrons with $l, m \neq 0$ component from eqs. (A.1.21) and (A.1.22). Of course, this procedure is an approximation, although it is the exact transformation in the case that V_{qlm} is constant and the hybridization occurs only at the impurity site, i.e., $V(r) = V_0 \delta(\vec{r} - \vec{r}_{\mathrm{imp}})$ where $\vec{r}_{\mathrm{imp}}$ is the positional vector of the f-electron. There are two reasons to do such a procedure: (i) the direct hybridization occurs at the most localized space around the impurity, (i.e., $l = m = 0$ component), and (ii) the s-wave scattering mostly affects the lowest-lying energy waves of the system.

Using the new integration variable $\varepsilon \equiv \varepsilon_q/D$, eqs. (A.1.21) and (A.1.22) are rewritten as

$$\bar{\mathcal{H}}_c = \int_{-1}^{1} \mathrm{d}\varepsilon \varepsilon c^{\dagger}_{\varepsilon} c_{\varepsilon}, \tag{A.1.23}$$

$$\bar{\mathcal{H}}_{\mathrm{hyb}} = \int_{-1}^{1} \mathrm{d}\varepsilon \left[\sqrt{\frac{\bar{\Delta}(\varepsilon)}{\pi}} c^{\dagger}_{\varepsilon} f + \mathrm{h.c.}\right], \tag{A.1.24}$$

where $\Delta(\varepsilon)$ and c_{ε} are defined as follow.

$$\bar{\Delta}(\varepsilon) = \pi \frac{4\pi\Omega k_F^3}{(2\pi)^3} \frac{\mathrm{d}q}{\mathrm{d}\varepsilon} q^2 \left[\frac{|V_{q00}|^2}{D}\right] = \pi\rho(\varepsilon) \left[\frac{|V_{q00}|}{D}\right]^2, \tag{A.1.25}$$

$$c_{\varepsilon} = \frac{V^*_{q00}}{|V_{q00}|} \sqrt{\frac{\mathrm{d}q}{\mathrm{d}\varepsilon}} c_{q00}. \tag{A.1.26}$$

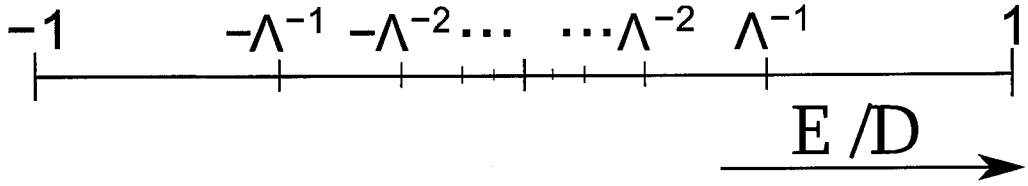

Figure A.1: The logarithmic discretization of the conduction electron. The original point shows the Fermi energy.

It is noted that c_ε obeys the anti-commutation rules yet.

We also measure the impurity term, eq. (A.1.4) in a unit of D, and complete the transformation. Here, we write the transformed semi-infinite chain model by taking account of the spin.

$$\bar{\mathcal{H}}_c = \sum_\sigma \int_{-1}^{1} \mathrm{d}\varepsilon \varepsilon c^\dagger_{\varepsilon\sigma} c_{\varepsilon\sigma}, \tag{A.1.27}$$

$$\bar{\mathcal{H}}_{\mathrm{hyb}} = \sum_\sigma \int_{-1}^{1} \mathrm{d}\varepsilon \left[\sqrt{\frac{\bar{\Delta}(\varepsilon)}{\pi}} c^\dagger_{\varepsilon\sigma} f_\sigma + \mathrm{h.c.} \right], \tag{A.1.28}$$

$$\bar{\mathcal{H}}_f = \mathcal{H}_f/D = \sum_\sigma \bar{\varepsilon}_f f^\dagger_\sigma f_\sigma + \bar{U} n_{f\uparrow} n_{f\downarrow}, \tag{A.1.29}$$

where $\bar{\varepsilon_f} \equiv \varepsilon_f/D$ and $\bar{U} \equiv U/D$.

A.1.2 Logarithmic Discretization

Nest, we rewrite the continuum conduction bands into the discrete form, which is suitable for carrying out the numerical calculation. If we discretize conduction bands at regular intervals, it needs an immense amount of time to carry out the calculation in a good accuracy. Therefore, we discretize the conduction bands logarithmically with the discretization parameter Λ as shown in Fig. A.1, by taking into consideration that the dominant contribution comes from the vicinity of the Fermi energy at the low temperature region.

Now, we introduce a complete set of the orthonormal function $\{\varphi^\pm_n(\varepsilon)\}$ for the intervals of conduction bands, $[\Lambda^{-n-1}, \Lambda^{-n}]$ and $[-\Lambda^{-n}, -\Lambda^{-n-1}]$ as follows.

$$c_\sigma(\varepsilon) = \sum_{n=0}^{\infty} \left[\varphi^+_n(\varepsilon) a_{n\sigma} + \varphi^-_n(\varepsilon) b_{n\sigma} \right], \tag{A.1.30}$$

where n is the index of interval. Here, $\varphi_n^{\pm}(\varepsilon)$ is defined as that having the same ε-dependence with $\bar{\Delta}(\varepsilon)$ as following.

$$\varphi_{n0}^{+}(\varepsilon) = \begin{cases} \frac{1}{F_n^{+}}\sqrt{\frac{\bar{\Delta}(\varepsilon)}{\pi}} & \text{for} \quad \Lambda^{-n-1} < \varepsilon \leq \Lambda^{-n}, \\ 0 & \text{for} \quad \text{othewise}, \end{cases} \tag{A.1.31}$$

$$\varphi_{n0}^{-}(\varepsilon) = \begin{cases} \frac{1}{F_n^{-}}\sqrt{\frac{\bar{\Delta}(\varepsilon)}{\pi}} & \text{for} \quad -\Lambda^{-n} \leq \varepsilon < \Lambda^{-n-1}, \\ 0 & \text{for} \quad \text{othewise}, \end{cases} \tag{A.1.32}$$

where $F_n^{\pm}$ is the normalization factor defined as follow with using the $\int^{+n} \equiv \int_{\Lambda^{-n-1}}^{\Lambda^{-n}}$ and $\int^{-n} \equiv \int_{-\Lambda^{-n}}^{-\Lambda^{-n-1}}$:

$$\left(F_n^{\pm}\right)^2 = \frac{1}{\pi}\int^{\pm n} \mathrm{d}\varepsilon \bar{\Delta}(\varepsilon). \tag{A.1.33}$$

Substituting eq. (A.1.30) into eqs. (A.1.28) and (A.1.29), we obtain following expressions.

$$\bar{\mathcal{H}}_{\mathrm{c}} = \sum_{\sigma}\sum_{n=0}^{\infty}\left[\xi_n^{+} a_{n\sigma}^{\dagger} a_{n\sigma} + \xi_n^{-} b_{n\sigma}^{\dagger} b_{n\sigma}\right], \tag{A.1.34}$$

$$\bar{\mathcal{H}}_{\mathrm{hyb}} = \sum_{\sigma}\sum_{n=0}^{\infty}\left[(F_n^{+} a_{n\sigma}^{\dagger} + F_n^{-} b_{n\sigma}^{\dagger}) f_{\sigma} + h.c.\right], \tag{A.1.35}$$

$$\xi_n^{\pm} = \frac{1}{\pi F_n^{\pm 2}}\int^{\pm n} \mathrm{d}\varepsilon\varepsilon\bar{\Delta}(\varepsilon) = \frac{\int^{\pm n}\mathrm{d}\varepsilon\varepsilon\bar{\Delta}(\varepsilon)}{\int^{\pm n}\mathrm{d}\varepsilon\bar{\Delta}(\varepsilon)}. \tag{A.1.36}$$

It is impossible to carry out the diagonalization of the conduction electron term, eq. (A.1.34), because we need a lot of basis functions in order to represent the conduction electron states. For this situation, K. G. Wilson suggested rewriting the conduction electron term, eq. (A.1.34) into the one-dimensional semi-infinite chain model with using the following orthogonal transformation.

$$a_{n\sigma} = \sum_{n=0}^{\infty} u_{mn} f_{n\sigma}, \tag{A.1.37}$$

$$b_{n\sigma} = \sum_{n=0}^{\infty} v_{mn} f_{n\sigma}, \tag{A.1.38}$$

$$f_{n\sigma} = \sum_{m=0}^{\infty}\left[u_{nm} a_{m\sigma} + v_{nm} b_{m\sigma}\right]. \tag{A.1.39}$$

Using eqs. (A.1.37) and (A.1.38), eqs. (A.1.34) and (A.1.35) are written as

$$\bar{\mathcal{H}}_{\rm c} = \sum_{\sigma}\sum_{n=0}^{\infty}\left[\varepsilon_n f_{n\sigma}^{\dagger} f_{n\sigma} + t_n(f_{n\sigma}^{\dagger} f_{n+1\sigma} + f_{n+1\sigma}^{\dagger} f_{n\sigma})\right], \tag{A.1.40}$$

$$\bar{\mathcal{H}}_{\rm hyb} = \sum_{\sigma} v\left[f_{\sigma}^{\dagger} f_{0\sigma} + f_{0\sigma}^{\dagger} f_{\sigma}\right], \tag{A.1.41}$$

$$f_{0\sigma} = \frac{1}{v}\sum_{m}\left[F_m^{+} a_{m\sigma} + F_m^{-} b_{m\sigma}\right], \tag{A.1.42}$$

$$v^2 = \sum_{n=0}^{\infty}\left[F_n^{+2} + F_n^{-2}\right] = \frac{1}{\pi}\int_{-1}^{1} {\rm d}\varepsilon \bar{\Delta}(\varepsilon). \tag{A.1.43}$$

New operator $f_{n\sigma}$ obeys the anti-commutation rule and u_{nm}, v_{nm} are normalized as follow.

$$\{f_{n\sigma}, f_{n'\sigma'}^{\dagger}\} = \delta_{n,n'}\delta_{\sigma,\sigma'}, \tag{A.1.44}$$

$$\{f_{n\sigma}, f_{n'\sigma'}\} = 0, \tag{A.1.45}$$

$$\sum_{m=0}^{\infty}\left[u_{nm}u_{n'm} + v_{nm}v_{n'm}\right] = \delta_{n,n'}, \tag{A.1.46}$$

$$\sum_{n=0}^{\infty} u_{nm}u_{nm'} = \delta_{mm'}, \tag{A.1.47}$$

$$\sum_{n=0}^{\infty} u_{nm}u_{nm'} = \delta_{mm'}. \tag{A.1.48}$$

Here, we avoid deriving the process of this transformation. Instead of this procedure, we derive the coefficient of the orthogonal transformation, i.e., u_{nm} and v_{nm} in eq. (A.1.39) by assuming that we already know that the one-dimensional semi-finite chain form can be mapped on the form represented by eqs. (A.1.40) and (A.1.41). It is easy to obtain u_{0m} and v_{0m} by using eqs. (A.1.42) and (A.1.43).

$$u_{0m} = \frac{F_m^{+}}{v}, \tag{A.1.49}$$

$$v_{0m} = \frac{F_m^{-}}{v}. \tag{A.1.50}$$

In order to obtain u_{1m} and v_{1m}, we subtract the term multiplied by $f_{0\sigma}$ from eq. (A.1.40).

$$\left[\varepsilon_0 f_{0\sigma}^{\dagger} + t_0 f_{1\sigma}^{\dagger}\right] f_{0\sigma}. \tag{A.1.51}$$

On the other hand, the original form, eq. (A.1.34), is rewritten by substituting eqs. (A.1.37) and (A.1.38).

$$\sum_{m=0}^{\infty} \left[\xi_m^+ u_{0m} a_{m\sigma}^\dagger + \xi_m^- v_{0m} b_{m\sigma}^\dagger\right] f_{0\sigma}. \tag{A.1.52}$$

Comparing the coefficient of $f_{0\sigma}$ in eqs. (A.1.51) and (A.1.52), we obtain

$$t_0 f_{1\sigma} = \sum_{m=0}^{\infty} \left[(\xi_m^+ - \varepsilon_0) u_{0m} a_{m\sigma}^\dagger + (\xi_m^- - \varepsilon_0) v_{0m} b_{m\sigma}^\dagger\right] \tag{A.1.53}$$

$$\Leftrightarrow \quad u_{1m} = \frac{1}{t_0}(\xi_m^+ - \varepsilon_0) u_{0m}, \tag{A.1.54}$$

$$v_{1m} = \frac{1}{t_0}(\xi_m^- - \varepsilon_0) v_{0m}. \tag{A.1.55}$$

Adding two equations which are obtained by multiplying both side of each eq. (A.1.54) by u_{0m} and eq. (A.1.55) by v_{0m}, and summing about m, we derive ε_0 as

$$\varepsilon_0 = \sum_{m=0}^{\infty} \left[\xi_m^+ u_{0m}^2 + \xi_m^- v_{0m}^2\right] = \frac{1}{\pi v^2} \int_{-1}^{1} d\varepsilon \varepsilon \Delta(\varepsilon). \tag{A.1.56}$$

On the other hand, t_0 can be derived by substituting eqs. (A.1.54) and (A.1.55) into (A.1.46), and taking $n = n'$.

$$\begin{aligned} t_0^2 &= \sum_{m=0}^{\infty} \left[(\xi_m^+ - \varepsilon_0)^2 u_{0m}^2 + (\xi_m^- - \varepsilon_0)^2 v_{0m}^2\right] \\ &= \frac{1}{v^2} \sum_{m=0}^{\infty} \left[\left\{F_m^+(\xi_m^+ - \varepsilon_0)\right\}^2 + \left\{F_m^-(\xi_m^- - \varepsilon_0)\right\}^2\right]. \end{aligned} \tag{A.1.57}$$

In the same way, we can derive t_n and ε_n for $n \geq 1$ sequentially.

$$\varepsilon_n = \sum_{m=0}^{\infty} (\xi_m^+ u_{nm}^2 + \xi_m^- v_{nm}^2), \tag{A.1.58}$$

$$t_n^2 = \sum_{m=0}^{\infty} \left[\xi_m^{+2} u_{nm}^2 + \xi_m^{-2} v_{nm}^2\right] - t_{n-1}^2 - \varepsilon_n^2, \tag{A.1.59}$$

$$u_{n+1m} = \frac{1}{t_n}\left[(\xi_m^+ - \varepsilon_n) u_{nm} - t_{n-1} u_{n-1m}\right], \tag{A.1.60}$$

$$v_{n+1m} = \frac{1}{t_n}\left[(\xi_m^- - \varepsilon_n) v_{nm} - t_{n-1} v_{n-1m}\right]. \tag{A.1.61}$$

When we consider the ε-dependent density of state of conduction electron such as $La_xSr_{1-x}Cu_2O_4$ which does not have density of state at around Fermi energy, we calculate $u_{nm}, v_{nm}, t_n, \varepsilon_n$ numerically by using the recurrence formula noted above. For large n, it is necessary to apply the Gram-Schmidt orthogonalization for u_{nm} and v_{nm} because n_{nm} and v_{nm} do not obey the orthogonal condition at $n \sim 20 - 30$ due to the numerical error.

Up to here, we carried out the transformation as we can apply for the general problem. However, the formula become simple if we take the following simplifications.

[1] The hybridization between the f-electron and conduction electrons is independent on ε (i.e., $V(\varepsilon) = \text{const}$).

[2] The conduction bands hold the particle-hole symmetry.

[3] The density of state of the conduction band is independent on ε (i.e., $\rho(\varepsilon) = \text{const}$).

Using 1., we obtain $\varepsilon_0 = 0$ because the integrated function in eq. (A.1.56) is odd function about ε. With condition 2, $\bar{\Delta}(\varepsilon) = \bar{\Delta}(-\varepsilon)$ because the hybridization is symmetric about ε, giving $\varepsilon_n = 0$ for all n. With using these assumptions, the Anderson model can be mapped onto the following one-dimensional semi-infinite chain Hamiltonian.

$$\bar{\mathcal{H}} = \bar{\mathcal{H}}_c + \bar{\mathcal{H}}_{\text{hyb}} + \bar{\mathcal{H}}_f, \tag{A.1.62}$$

$$\bar{\mathcal{H}}_c = \sum_\sigma \sum_{n=0}^{\infty} t_n (f^\dagger_{n\sigma} f_{n+1\sigma} + f^\dagger_{n+1\sigma} f_{n\sigma}), \tag{A.1.63}$$

$$\bar{\mathcal{H}}_{\text{hyb}} = \sum_\sigma v \left[f^\dagger_{-1\sigma} f_{0\sigma} + f^\dagger_{0\sigma} f_{-1\sigma} \right], \tag{A.1.64}$$

$$\bar{\mathcal{H}}_f = \sum_\sigma \bar{\varepsilon}_f f^\dagger_{-1\sigma} f_{-1\sigma} + U f^\dagger_{-1\uparrow} f^\dagger_{-1\downarrow} f_{-1\downarrow} f_{-1\uparrow}. \tag{A.1.65}$$

Moreover, within these assumption, the analytical expressions of $t_n, f_{n\sigma}$ are

derived by K. G. Wilson.

$$t_n = \frac{1+\Lambda^{-1}}{2}\frac{1-\Lambda^{-n-1}}{\sqrt{(1-\Lambda^{-2n-1})(1-\Lambda^{-2n-3})}}\Lambda^{-n/2}, \quad \text{(A.1.66)}$$

$$\to \frac{1+\Lambda^{-1}}{2}\Lambda^{-n/2} \qquad \text{for } n \to \infty, \quad \text{(A.1.67)}$$

$$f_{0\sigma} = \left(\frac{1-\Lambda^{-1}}{2}\right)^{1/2}\sum_{m=0}^{\infty}\Lambda^{-m/2}(a_{m\sigma}+b_{m\sigma}), \quad \text{(A.1.68)}$$

$$f_{1\sigma} = \left(\frac{1-\Lambda^{-3}}{2}\right)^{1/2}\sum_{m=0}^{\infty}\Lambda^{-3m/2}(a_{m\sigma}-b_{m\sigma}), \quad \text{(A.1.69)}$$

$$\vdots$$

Figure. A.2 shows the diagramatic representation of the Hamiltonian (A.1.62) in which there are the impurity site written by f-electron state hybridizing with the conduction electron site 0, and the conduction band is represented by the one-dimensional chain having only the nearest-neighbor hopping t_n. Here, $f^{(\dagger)}_{-1\sigma}$ represents the creation operator of the f-electron.

The one-dimensional infinite-chain model can be mapped on the real space as shown in Fig. A.3. The conduction site 0 is superposition of waves from various energy scale, then site 0 indicates the most localized conduction electron with an extent k_{F}^{-1} from the impurity site. As n increases, the energy range taken into the conduction site becomes narrow, which corresponds to consider the further conduction electron in the real space. Moreover, the hopping t_n decreases exponentially as n increases, which indicate that the contribution of conduction electrons gradually decreases as the distance from the impurity site increases.

A.2 Renormalization Group Method and Sequentially-Diagonalization

The Renormalization group (RG) transformation $\mathcal{R}$ means the projection from the Hamiltonian written by a certain set of parameters K to that written by a different set of parameters K'.

$$\mathcal{R}\mathcal{H}(K) = \mathcal{H}(K'). \quad \text{(A.2.1)}$$

P. W. Anderson and his coworkers carried out this RG transformation for the Kondo model, which is called as the poorman's scaling theory. They eliminated

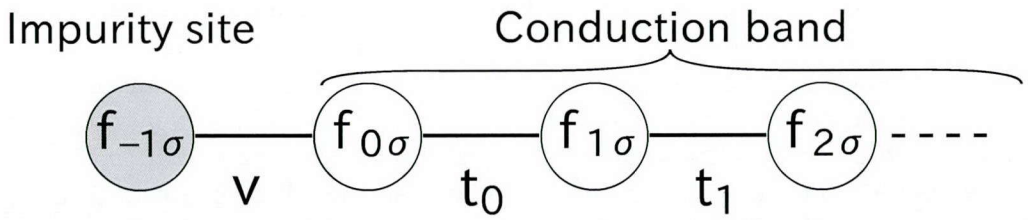

Figure A.2: The diagrammatic representation of the Hamiltonian (A.1.62). The original point indicates the impurity site hybridizing with the conduction site written as $f_{0\sigma}$. The conduction electron sites line up one-dimensionally and there are only nearest neighbor hopping.

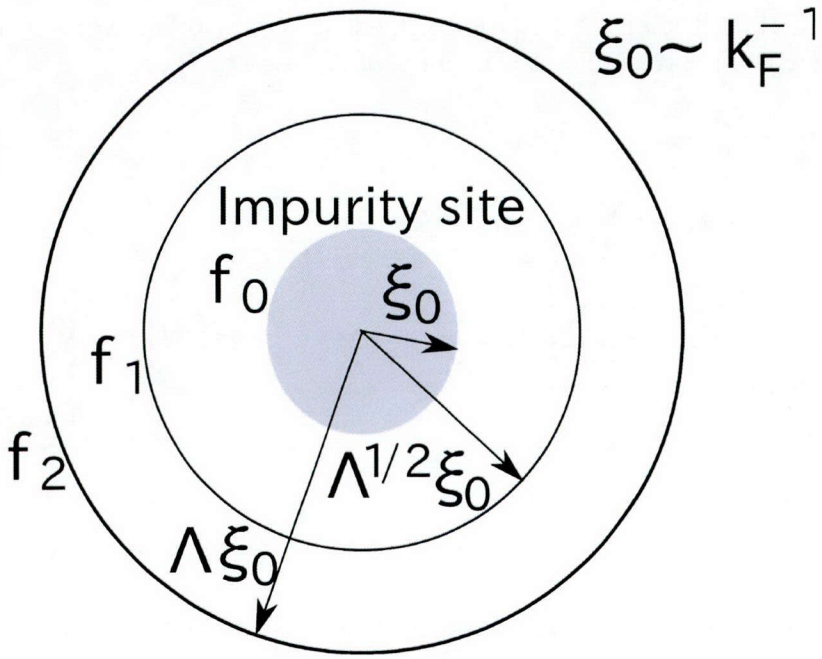

Figure A.3: The mapping of the one-dimensional infinite-chain model on the real space.

the degree of the freedom of conduction electrons with high energy perturbatively, and derive the scaling equation for the coupling constants between the localized moment and conduction electrons. With this procedure, the original model is renormalized into an effective model through the renormalization of the coupling constants as noted in the Introduction. This scaling equation indicates that there are two fixed points: one is the weak coupling fixed point where the coupling between the localized moment and conduction electron is lost, the other is the strong coupling limit where the coupling constants increases infinitely as the band width of the conduction electron is reduced.

The NRG method takes the idea of this RG transformation. Since the NRG follows the change of the energy spectrum of the many-bode system by the RG transformation, it can avoid breaking down of the RG transformation, which occur in the poorman's scaling theory due to the increase of coupling constants.

In order to apply the NRG method, we transform the one-dimensional infinite chain Hamiltonian into the form which is suitable for the RG transformation. Here, we prepare the Hamiltonian $\mathcal{H}_N$ in which the summation about n in the Hamiltonian (A.1.62) is stopped at N. In other words, the Hamiltonian (A.1.62) corresponds to the limit of $N \to \infty$ of $\mathcal{H}_N$.

$$\bar{\mathcal{H}} = \lim_{N\to\infty} \frac{1+\Lambda^{-1}}{2} \Lambda^{-(N-1)/2} \mathcal{H}_N, \tag{A.2.2}$$

$$\mathcal{H}_N = \Lambda^{(N-1)/2} \left[\tilde{\mathcal{H}}_f + \tilde{v} \sum_\sigma (f^\dagger_{-1\sigma} f_{0\sigma} + f^\dagger_{0\sigma} f_{-1\sigma}) + \sum_\sigma \sum_{n=0}^{N-1} \Lambda^{-n/2} \tilde{t}_n (f^\dagger_{n\sigma} f_{n+1\sigma} + f^\dagger_{n+1\sigma} f_{n\sigma}) \right], \tag{A.2.3}$$

$$\tilde{\mathcal{H}}_f = \frac{2}{1+\Lambda^{-1}} \bar{\mathcal{H}}_f. \tag{A.2.4}$$

$$\tilde{v} = \frac{2}{1+\Lambda^{-1}} v, \tag{A.2.5}$$

$$\tilde{t}_n = \frac{2}{1+\Lambda^{-1}} \Lambda^{n/2} t_n. \tag{A.2.6}$$

In this definition, $\mathcal{H}_N$ obeys the following recurrence formula with using the RG transformation $\mathcal{R}$.

$$\begin{aligned} \mathcal{H}_{N+1} &= \mathcal{R}(\mathcal{H}_N) \\ &= \Lambda^{1/2} \mathcal{H}_N + \sum_\sigma \tilde{t}_N (f^\dagger_{N\sigma} f_{N+1\sigma} + f^\dagger_{N+1\sigma} f_{N\sigma}). \end{aligned} \tag{A.2.7}$$

In the NRG method, we are interested in the lowest-lying energy spectrum at each energy scale. For the purpose of comparing the energy spectrum at each energy scale, we introduce the factors, $\Lambda^{(N-1)/2}$ in eq. (A.2.3) and $\frac{1+\Lambda^{-1}}{2}$ in eq. (A.2.2), in order to make t_n converge with 1 in the limit of $N \to \infty$. In order to consider $\bar{H}_f$ and $\bar{H}_{\rm hyb}$ with the same recurrence formula, eq. (A.2.7), we define the first term and the first hopping term of the recurrence formula as follow.

$$\mathcal{H}_{-1} = \Lambda^{-1}\tilde{\mathcal{H}}_f, \tag{A.2.8}$$

$$\tilde{t}_{-1} = \tilde{v}. \tag{A.2.9}$$

Using the relation (A.2.7), the NRG method is carried out as following. (This procedure is called the successive diagonalization.)

[1] Obtain the eigenvalue and eigenvector of $\mathcal{H}_N$ by means of the numerical diagonalization.

[2] Calculate matrix elements of $\mathcal{H}_{N+1}$ with using the recurrence formula, eq. (A.2.7) from the eigenvalue and eigenvector obtained from $\mathcal{H}_N$.

[3] Obtain the eigenvalue and eigenvector of $\mathcal{H}_{N+1}$ by means of the numerical diagonalization.

[4] Iterate the calculation from procedure 2.

Fig. A.4 is a view showing the successive diagonalization at $N = 1$ and $N = 2$ steps. In the NRG calculation, we first obtain the exact solution of the impurity site, and take in the effect of the conduction electrons perturbatively from the most spatially localized conduction electrons. The energy scale of the conduction term added in N-th step is smaller than that in $(N + 1)$-th step by $\Lambda^{-1/2}$. When the system reaches at the fixed point, we obtain the same energy spectrum through the successive diagonalization if we take the energy of the ground state as zero. (Strictly speaking, as shown in the next section, we obtain the same energy spectrum by two times of the successive diagonalization because the spectrum in the even step is different from that in the odd step.)

Through the successive diagonalization, the number of state increases exponentially with N even when we consider symmetries of the model so that the full matrix takes a block-diagonal form with smaller submatrices. In order to avoid this problem, we keep the eigenstates from the ground state to the Ntr-th excited state, and discard the other high energy eigenstates. Here,

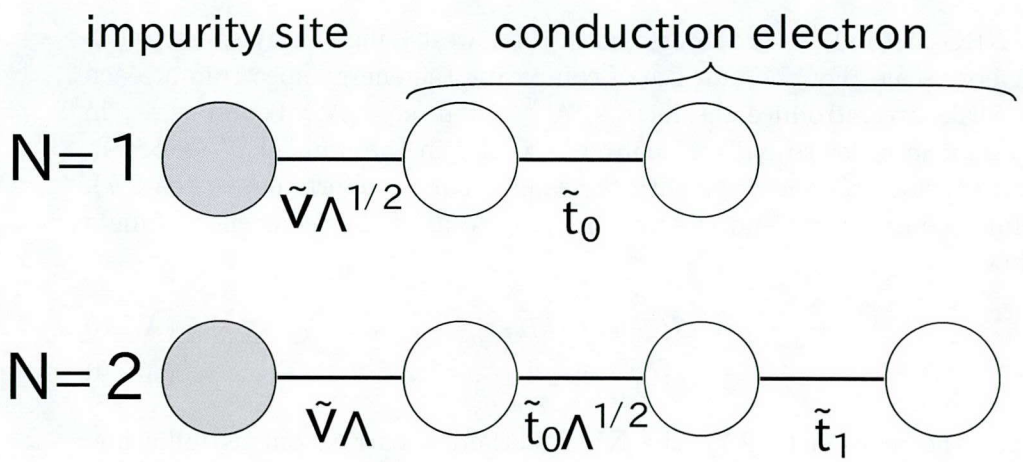

Figure A.4: A view showing the successive diagonalization at $N = 1$ and $N = 2$ steps. The last hopping term is always of the order of 1.

we should not discard the eigenstates automatically in order not to break the symmetry of the system. Therefore, we promise to keep (or discard) all states which have the same energy with $N_{\rm tr}$-th state. Suitable value for the parameter $N_{\rm tr}$ depends on the model: for the single impurity Anderson model, $N_{\rm tr} \sim 500$ is sufficient to obtain the result with a good accuracy. This approximation, called "truncation", is valid because the discarded high energy states hardly affect the lowest-lying energy spectrum.

As mentioned above, the NRG method is the numerical technique that we investigate the low energy spectrum at zero temperature by taking the effect of the conduction electrons perturbatively and discarding the negligible high energy states. As shown in the following section, the NRG method allows us to obtain the temperature dependence of various physical quantities when we consider the result at a certain energy scale as that at the corresponding temperature. The detail calculation of the physical quantities is mentioned below.

A.3 Numerical Treatment

In this section, we introduce the key of the NRG calculation, how we calculate the matrix elements of $\mathcal{H}_{N+1}$ from the eigenvalue and eigenvector of $\mathcal{H}_N$ in eq. (A.2.7).

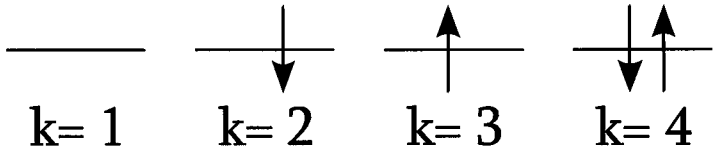

Figure A.5: Four possible spin state in each conduction shell and their index k.

Here, we take the single impurity Anderson model as an example. In this case, the total charge Q and the z-component of total spin S_z are the conservative quantities.

$$Q = \sum_{n=-1}^{N} \left[f_{n\uparrow}^{\dagger} f_{n\uparrow} + f_{n\downarrow}^{\dagger} f_{n\downarrow} \right] - (N+2), \tag{A.3.1}$$

$$2S_z = \sum_{n=-1}^{N} \left[f_{n\uparrow}^{\dagger} f_{n\uparrow} - f_{n\downarrow}^{\dagger} f_{n\downarrow} \right], \tag{A.3.2}$$

where Q is represented by the deviation from the half-filling. It is noted that we do not take the total spin S as the conservative quantity although K. G. Wilson did so in the original NRG method. This is because we often discuss the effect of the magnetic field which gives the matrix element between states with different S.

With these quantities, we carry out the diagonalization of $\mathcal{H}_{N+1}$ with use of the block-diagonalization, i.e., we split full matrix of $\mathcal{H}_{N+1}$ into small submatrices in which all the states have the same Q and S_z.

We write the eigenvalue and eigenvector of the N-th step Hamiltonian H_N as $E_N(Q, S_z, r_N)$ and $\{|Q, S_z, r_N\rangle_N\}$,

$$\mathcal{H}_N |Q, S_z, r_N\rangle_N = E_N(Q, S_z, r_N) |Q, S_z, r_N\rangle_N, \tag{A.3.3}$$

$${}_N\langle Q, S_z, r_N | Q', S_z', r_N' \rangle_N = \delta_{Q,Q'} \delta_{S_z,S_z'} \delta_{r_N,r_N'}, \tag{A.3.4}$$

where r_N is the index to distinguish the states with same Q and S_z.

Now, we consider to add the $(N+1)$-th "conduction shell" (the conduction electron site written by $f_{N+1\sigma}$) to the well-known system H_N. For example, $f_{N+1\uparrow}^{\dagger}$ means that we add the up-spin conduction electron in $(N+1)$-th conduction shell. Fig. A.5 shows the four possible states in each conduction shell where we allot the index k for each state. We construct a basis for H_{N+1}, $|Q, 2S_z, \alpha_{N+1}, k_{N+1} r_N\rangle\rangle_{N+1}$, by the direct product between the eigenstate of

index	state at $(N+1)$-th shell	δQ^k	δS_z^k
1	$X_1 \equiv \|0\rangle$	-1	0
2	$X_2 \equiv f^\dagger_{N+1\downarrow}\|0\rangle$	0	-1
3	$X_3 \equiv f^\dagger_{N+1\uparrow}\|0\rangle$	0	1
4	$X_4 \equiv f^\dagger_{N+1\uparrow} f^\dagger_{N+1\downarrow}\|0\rangle$	1	0

Table A.1: The amounts of change of conservative quantities when the $(N+1)$-th conduction shell is added to H_N. $|0\rangle$ indicates the vacuum state.

H_N, $\{|Q, 2S_z, r_N\rangle_N\}$, and states for the added conduction shell, $\hat{X}_k$.

$$\begin{aligned}\hat{X}_k \otimes |Q, 2S_z, r_N\rangle_N &= |Q+\delta Q^k, 2S_z + 2\delta S_z^k, \alpha_{N+1}, k_{N+1}; r_N\rangle\rangle_{N+1} \\ &\equiv |Q, 2S_z, \alpha_{N+1}, k_{N+1} r_N\rangle\rangle_{N+1}, \end{aligned} \tag{A.3.5}$$

where k_{N+1} is the index for the spin state at the $(N+1)$-th conduction shell. We call such defined basis $|Q, 2S_z, \alpha_{N+1}, k_{N+1}, r_N\rangle\rangle_{N+1}$ of $\mathcal{H}_{N+1}$ as trial state. The quantities δQ^k and δS_z^k are amounts of changes of the total charge Q and the z-component of the total spin S_z when the $(N+1)$-th conduction shell is added, which are given in table A.1.

For a eigenstate of $\mathcal{H}_N$ $|Q, 2S_z, r_N(i)\rangle_N$, we make four trial states.

$$1|Q, 2S_z, r_N(i)\rangle_N = |Q-1, 2S_z, \alpha_{N+1}, 1; r_N\rangle\rangle_{N+1} \equiv |1\rangle\rangle_{N+1}, \tag{A.3.6}$$

$$f^\dagger_{N+1\downarrow}|Q, 2S_z, r_N\rangle_N = |Q, 2S_z - 1, \alpha_{N+1}, 2; r_N\rangle\rangle_{N+1} \equiv |2\rangle\rangle_{N+1}, \tag{A.3.7}$$

$$f^\dagger_{N+1\uparrow}|Q, 2S_z, r_N\rangle_N = |Q, 2S_z + 1, \alpha_{N+1}, 3; r_N\rangle\rangle_{N+1} \equiv |3\rangle\rangle_{N+1}, \tag{A.3.8}$$

$$f^\dagger_{N+1\uparrow} f^\dagger_{N+1\downarrow}|Q, 2S_z, r_N\rangle_N = |Q+1, 2S_z, \alpha_{N+1}, 4; r_N\rangle\rangle_{N+1} \equiv |4\rangle\rangle_{N+1}. \tag{A.3.9}$$

We consider the matrix element for H_{N+1} from two basis, $|k_{N+1}(i)\rangle\rangle_{N+1}$ and $|k_{N+1}(j)\rangle\rangle_{N+1}$ which are are constructed of two of eigenstates of $\mathcal{H}_N$, $|Q, S_z, r_N(i)\rangle_N$ and $|Q, S_z, r_N(j)\rangle_N$. For the case of $k_{N+1}(i) = k_{N+1}(j)$, we obtain the diagonal term from the first term in eq. (A.2.7) as $\Lambda^{1/2} E(Q, 2S_z, r_N)\delta_{i,j}$. On the other hand, the second term in eq. (A.2.7) give the off-diagonal term, and non-zero term are obtained for the following cases.

[1] $f^{\dagger}_{N\downarrow} f_{N+1\downarrow}$

$$\begin{aligned} f^{\dagger}_{N\downarrow} f_{N+1\downarrow}|2\rangle\rangle_{N+1} &= f^{\dagger}_{N\downarrow} f_{N+1\downarrow} f^{\dagger}_{N+1\downarrow}|Q, 2S_z, r_N\rangle_N \\ &= f^{\dagger}_{N\downarrow}|Q, 2S_z, r_N\rangle_N \\ &= f^{\dagger}_{N\downarrow}|1\rangle\rangle_{N+1}, \qquad \text{(A.3.10)} \\ f^{\dagger}_{N\downarrow} f_{N+1\downarrow}|4\rangle\rangle_{N+1} &= f^{\dagger}_{N\downarrow} f_{N+1\downarrow} f^{\dagger}_{N+1\uparrow} f^{\dagger}_{N+1\downarrow}|Q, 2S_z, r_N\rangle_N \\ &= -f^{\dagger}_{N\downarrow} f^{\dagger}_{N+1\uparrow}|Q, 2S_z, r_N\rangle_N \\ &= -f^{\dagger}_{N\downarrow}|3\rangle\rangle_{N+1}, \qquad \text{(A.3.11)} \end{aligned}$$

[2] $f^{\dagger}_{N\uparrow} f_{N+1\uparrow}$

$$\begin{aligned} f^{\dagger}_{N\uparrow} f_{N+1\uparrow}|3\rangle\rangle_{N+1} &= f^{\dagger}_{N\uparrow} f_{N+1\uparrow} f^{\dagger}_{N+1\uparrow}|Q, 2S_z, r_N\rangle_N \\ &= f^{\dagger}_{N\uparrow}|Q, 2S_z, r_N\rangle_N \\ &= f^{\dagger}_{N\uparrow}|1\rangle\rangle_{N+1}, \qquad \text{(A.3.12)} \\ f^{\dagger}_{N\uparrow} f_{N+1\uparrow}|4\rangle\rangle_{N+1} &= f^{\dagger}_{N\uparrow} f_{N+1\uparrow} f^{\dagger}_{N+1\uparrow} f^{\dagger}_{N+1\downarrow}|Q, 2S_z, r_N\rangle_N \\ &= f^{\dagger}_{N\uparrow} f^{\dagger}_{N+1\downarrow}|Q, 2S_z, r_N\rangle_N \\ &= f^{\dagger}_{N\uparrow}|2\rangle\rangle_{N+1}, \qquad \text{(A.3.13)} \end{aligned}$$

[3] $f^{\dagger}_{N+1\downarrow} f_{N\downarrow}$

$$\begin{aligned} {}_{N+1}\langle\langle 2| f^{\dagger}_{N+1\downarrow} f_{N\downarrow} &= {}_N\langle Q, 2S_z, r_N| f_{N+1\downarrow} f^{\dagger}_{N+1\downarrow} f_{N\downarrow} \\ &= {}_N\langle Q, 2S_z r_N| f_{N\downarrow} \\ &= {}_{N+1}\langle\langle 1| f_{N\downarrow}, \qquad \text{(A.3.14)} \\ {}_{N+1}\langle\langle 4| f^{\dagger}_{N+1\downarrow} f_{N\downarrow} &= {}_N\langle Q, 2S_z, r_N| f_{N+1\downarrow} f_{N+1\uparrow} f^{\dagger}_{N+1\downarrow} f_{N\downarrow} \\ &= -\,{}_{N+1}\langle Q, 2S_z r_N| f_{N+1\uparrow} f_{N\downarrow} \\ &= -\,{}_{N+1}\langle\langle 3| f_{N\downarrow}, \qquad \text{(A.3.15)} \end{aligned}$$

[4] $f^{\dagger}_{N+1\uparrow} f_{N\uparrow}$

$$\begin{aligned} {}_{N+1}\langle\langle 3| f^{\dagger}_{N+1\uparrow} f_{N\uparrow} &= {}_N\langle Q, 2S_z, r_N| f_{N+1\uparrow} f^{\dagger}_{N+1\uparrow} f_{N\uparrow} \\ &= {}_N\langle Q, 2S_z r_N| f_{N\uparrow} \\ &= {}_{N+1}\langle\langle 1| f_{N\uparrow}, \qquad \text{(A.3.16)} \\ {}_{N+1}\langle\langle 4| f^{\dagger}_{N+1\uparrow} f_{N\uparrow} &= {}_N\langle Q, 2S_z, r_N| f_{N+1\downarrow} f_{N+1\uparrow} f^{\dagger}_{N+1\uparrow} f_{N\uparrow} \\ &= {}_N\langle Q, 2S_z r_N| f_{N+1\downarrow} f_{N\uparrow} \\ &= {}_{N+1}\langle\langle 3| f_{N\uparrow}. \qquad \text{(A.3.17)} \end{aligned}$$

As a result, for $|k_{N+1}(i)\rangle\rangle_{N+1}(k_{N+1}(i)=1\sim 4)$ and $|k_{N+1}(j)\rangle\rangle_{N+1}(k_{N+1}(j)=1\sim 4)$, the 4×4 matrix elements are obtained as follow.

$$\mathcal{H}_{N+1}=\begin{pmatrix} \Lambda^{1/2}E_N\delta_{i,j} & \tilde{t}_N A & \tilde{t}_N B & 0 \\ \tilde{t}_N\tilde{A} & \Lambda^{1/2}E_N\delta_{i,j} & 0 & \tilde{t}_N C \\ \tilde{t}_N\tilde{B} & 0 & \Lambda^{1/2}E_N\delta_{i,j} & -\tilde{t}_N D \\ 0 & \tilde{t}_N\tilde{C} & -\tilde{t}_N\tilde{D} & \Lambda^{1/2}E_N\delta_{i,j} \end{pmatrix}, \quad \text{(A.3.18)}$$

where

$$\begin{aligned} A &\equiv {}_{N+1}\langle\langle 1(i)|f^\dagger_{N\downarrow}|1(j)\rangle\rangle_{N+1}, & \tilde{A} &\equiv {}_{N+1}\langle\langle 1(i)|f_{N\downarrow}|1(j)\rangle\rangle_{N+1}, \\ B &\equiv {}_{N+1}\langle\langle 1(i)|f^\dagger_{N\uparrow}|1(j)\rangle\rangle_{N+1}, & \tilde{B} &\equiv {}_{N+1}\langle\langle 1(i)|f_{N\uparrow}|1(j)\rangle\rangle_{N+1}, \\ C &\equiv {}_{N+1}\langle\langle 2(i)|f^\dagger_{N\uparrow}|2(j)\rangle\rangle_{N+1}, & \tilde{C} &\equiv {}_{N+1}\langle\langle 2(i)|f_{N\uparrow}|2(j)\rangle\rangle_{N+1}, \\ D &\equiv {}_{N+1}\langle\langle 3(i)|f^\dagger_{N\downarrow}|3(j)\rangle\rangle_{N+1}, & \tilde{D} &\equiv {}_{N+1}\langle\langle 3(i)|f_{N\downarrow}|3(j)\rangle\rangle_{N+1}. \end{aligned}$$

Here, the eigenstate of H_N, $\{|r_N\rangle_N\}$, is written by the linear combination of the trial states of $\mathcal{H}_N$.

$$|Q,2S_z,r_N\rangle_N=\sum_{\alpha_N}U_{r_N,\alpha_N}|Q,2S_z,\alpha_N,k_N;r_{N-1}\rangle\rangle_{N+1}. \quad \text{(A.3.19)}$$

Using eq. (A.3.19), we calculate $A\sim D$ and $\tilde{A}\sim\tilde{D}$, for example, A is calculated as follows.

$$\begin{aligned} A &= {}_N\langle Q(i),2S_z(i),r_N(i)|f^\dagger_{N\downarrow}|Q(j),2S_z(j)r_N(j)\rangle_N \\ &= \sum_{\alpha_N(i),\alpha_N(j)} U_{r_N(i),\alpha_N(i)}U_{r_N(j),\alpha_N(j)} \\ &\quad\times {}_{N+1}\langle\langle Q(i),2S_z(i),\alpha_N(i);k_N(i)|f^\dagger_{N\downarrow}|Q(j),2S_z(j),\alpha_N(j);k_N(j)\rangle\rangle_{N+1} \\ &= \sum_{\alpha_N(i),\alpha_N(j)} U_{r_N(i),\alpha_N(i)}U_{r_N(j),\alpha_N(j)} \\ &\quad\times\Big\{\delta_{k_N(i),2}\delta_{k_N(j),1}\,{}_N\langle Q(i)-1,2S_z(i)+1,r_{N-1}|f_{N\downarrow}f^\dagger_{N\downarrow}|Q(j),2S_z(j),r_{N-1}(j)\rangle_N \\ &\qquad +\delta_{k_N(i),4}\delta_{k_N(j),3}\,{}_N\langle Q(i)-2,2S_z(i),r_{N-1}|f_{N\downarrow}f_{N\uparrow}f^\dagger_{N\downarrow}f^\dagger_{N\uparrow} \\ &\qquad\qquad \times|Q(j)-1,2S_z(j)-1,r_{N-1}(j)\rangle_N\Big\} \\ &= \delta_{Q(i)-1,Q(j)}\delta_{2S_z(i)+1,2S_z(j)}\sum_{\alpha_N(i)}\sum_{\alpha_N(j)} U_{r_N(i),\alpha_N(i)}U_{r_N(j),\alpha_N(j)} \\ &\qquad\times\delta_{r_{N-1}(i),r_{N-1}(j)}\left\{\delta_{k_N(i),2}\delta_{k_N(j),1}-\delta_{k_N(i),4}\delta_{k_N(j),3}\right\}. \end{aligned} \quad \text{(A.3.20)}$$

In the same way, the other terms can be calculated as follow.

$$\mathcal{H}_{N+1} = \begin{pmatrix} \Lambda^{1/2}E_N\delta_{i,j} & \tilde{t}_N\langle i|f^\dagger_{N\downarrow}|j\rangle & \tilde{t}_N\langle i|f^\dagger_{N\uparrow}|j\rangle & 0 \\ \tilde{t}_N\langle i|f_{N\downarrow}|j\rangle & \Lambda^{1/2}E_N\delta_{i,j} & 0 & -\tilde{t}_N\langle i|f^\dagger_{N\uparrow}|j\rangle \\ \tilde{t}_N\langle i|f_{N\uparrow}|j\rangle & 0 & \Lambda^{1/2}E_N\delta_{i,j} & \tilde{t}_N\langle i|f^\dagger_{N\downarrow}|j\rangle \\ 0 & -\tilde{t}_N\langle i|f_{N\uparrow}|j\rangle & \tilde{t}_N\langle i|f_{N\downarrow}|j\rangle & \Lambda^{1/2}E_N\delta_{i,j} \end{pmatrix}, \tag{A.3.21}$$

$$\begin{aligned}
\langle i|f^\dagger_{N\uparrow}|j\rangle &\equiv \delta_{Q(i)-1,Q(j)}\delta_{2S_z(i)-1,2S_z(j)} \sum_{\alpha_N(i)}\sum_{\alpha_N(j)} U_{r_N(i),\alpha_N(i)}U_{r_N(j),\alpha_N(j)} \\
&\quad \times\delta_{r_{N-1}(i),r_{N-1}(j)}\left[\delta_{k_N(i),3}\delta_{k_N(j),1}+\delta_{k_N(i),4}\delta_{k_N(j),2}\right], \qquad \text{(A.3.22)} \\
\langle i|f^\dagger_{N\downarrow}|j\rangle &\equiv \delta_{Q(i)-1,Q(j)}\delta_{2S_z(i)+1,2S_z(j)} \sum_{\alpha_N(i)}\sum_{\alpha_N(j)} U_{r_N(i),\alpha_N(i)}U_{r_N(j),\alpha_N(j)} \\
&\quad \times\delta_{r_{N-1}(i),r_{N-1}(j)}\left[\delta_{k_N(i),2}\delta_{k_N(j),1}-\delta_{k_N(i),4}\delta_{k_N(j),3}\right], \qquad \text{(A.3.23)} \\
\langle i|f_{N\uparrow}|j\rangle &= \langle j|f^\dagger_{N\uparrow}|i\rangle \\
&\equiv \delta_{Q(i)+1,Q(j)}\delta_{2S_z(i)+1,2S_z(j)} \sum_{\alpha_N(i)}\sum_{\alpha_N(j)} U_{r_N(i),\alpha_N(i)}U_{r_N(j),\alpha_N(j)} \\
&\quad \times\delta_{r_{N-1}(i),r_{N-1}(j)}\left[\delta_{k_N(i),1}\delta_{k_N(j),3}+\delta_{k_N(i),2}\delta_{k_N(j),4}\right], \qquad \text{(A.3.24)} \\
\langle i|f_{N\downarrow}|j\rangle &= \langle j|f^\dagger_{N\downarrow}|i\rangle \\
&\equiv \delta_{Q(i)+1,Q(j)}\delta_{2S_z(i)-1,2S_z(j)} \sum_{\alpha_N(i)}\sum_{\alpha_N(j)} U_{r_N(i),\alpha_N(i)}U_{r_N(j),\alpha_N(j)} \\
&\quad \times\delta_{r_{N-1}(i),r_{N-1}(j)}\left[\delta_{k_N(i),1}\delta_{k_N(j),2}-\delta_{k_N(i),3}\delta_{k_N(j),4}\right]. \qquad \text{(A.3.25)}
\end{aligned}$$

All the matrix elements of $\mathcal{H}_{N+1}$ are calculated by carrying out the way above for all combination of (i,j) and $k(i) = 1 \sim 4$. The eigenvectors and eigenvalues of H_{N+1} are obtained by the numerical diagonalization.

A.4 Analysis by Numerical Renormalization Group Method

In this section, we consider the result obtained from the NRG method and their physical interpretation for the free electron model and the Anderson model.

A.4.1 Free Electron Model

The free electron model is given by the following Hamiltonian corresponding to model that the Hamiltonian eq. (A.2.3) loses the impurity site indicated by

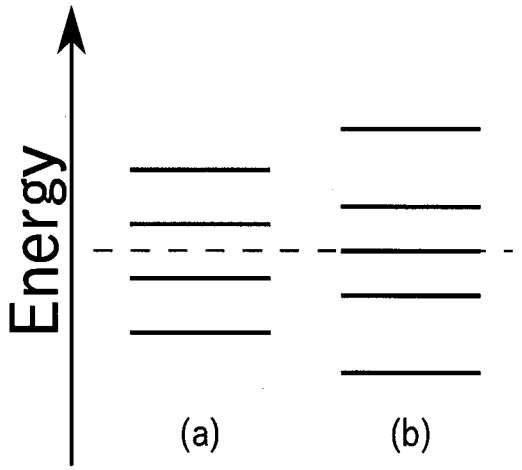

Figure A.6: The energy level of the free electron model when the conduction band holds the particle-hole symmetry for (a) odd N and (b) even N step cases. The dotted line indicate the Fermi energy.

$f_{-1\sigma}$.

$$\mathcal{H}_N = \sum_{\sigma}\sum_{n=0}^{N-1} \Lambda^{-n/2}\tilde{t}_n(f^{\dagger}_{n\sigma}f_{n+1\sigma} + f^{\dagger}_{n+1\sigma}f_{n+1\sigma}). \tag{A.4.1}$$

The Hamiltonian (A.4.1) corresponds to the one-dimensional Hubbard model with hopping term $\tilde{t}_N$ because there are no interaction between particles. Therefore, we can easily diagonalize the Hamiltonian (A.4.1) as

$$\mathcal{H}_N = \sum_{\sigma}\sum_{l=1}^{N+1} \eta_l g^{\dagger}_l g_l, \tag{A.4.2}$$

by using the following unitary transformation:

$$g_{l\sigma} = \sum_n U_{nl} f_{n\sigma}. \tag{A.4.3}$$

In this case, we obtain the energy spectrum η_l shown in Fig. A.6 for even and odd N, which is symmetric about the Fermi energy. Such symmetric energy spectrum originates at the fact that the Hamiltonian holds the particle-hole symmetry because the Hamiltonian is invariant for the following transformation.

$$f_{n\sigma} \to (-1)^n f^{\dagger}_{n\sigma}, f^{\dagger}_{n\sigma} \to (-1)^n f_{n\sigma}. \tag{A.4.4}$$

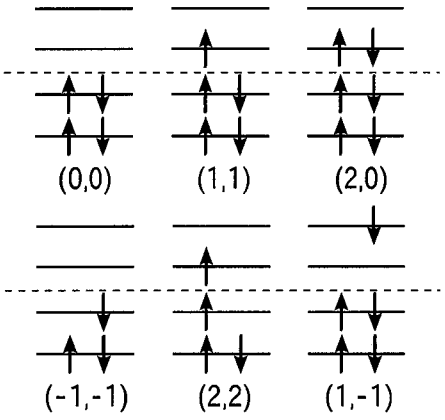

Figure A.7: The example of how the electrons occupy the states in the case of odd N for each $(Q, 2S_z)$. The lines show the energy spectrum and the dotted line shows the Fermi energy.

number	Q	$2S_z$	Energy/D(N =49)
1	0	0	0.00000000000
2,3	-1	±1	0.74856304802
4,5	1	±1	0.74856304802
6,7	-2	0	1.49371216384
8,9	0	±2	1.49371171781
10,11	2	0	1.49371171781
12,13	-1	± 1	2.24056802360
14,15	1	± 1	2.24056802360
16,17	-1	±1	2.49320678938
18,19	1	±1	2.49320678938
20	0	0	2.49320678938
21	-2	±-2	3.24006264766
22-24	-2	0	3.24006264766
25,26	0	2	3.24006264766
27,28	0	-2	3.24006264766
29-32	0	0	3.24006264766

In the ground state of the Hamiltonian (A.4.1), all the states with negative energy are occupied with two spins.

For the negative $g_{l\sigma}$, by defining the creation operator of the hole state as $h_{l\sigma} \equiv i(\sigma_y)_{\sigma\sigma'} g^\dagger_{i\sigma'}$, we obtain the positive excitation energy for the hole state because of the relation $g^\dagger_{l\sigma} g_{l\sigma} = 1 - h^\dagger_{l\sigma} h_{l\sigma}$. Using such a transformation for eq. (A.4.2), we obtain more clear form for Fig. A.6.

$$\begin{aligned}\mathcal{H}_N &= \sum_\sigma \sum_{l=1}^{N+1} \eta_l g^\dagger_{l\sigma} g_{l\sigma} \\ &= \begin{cases} \sum_\sigma \sum_{l=1}^{(N+1)/2} \eta_{lo} (g^\dagger_{l\sigma} g_{l\sigma} + h^\dagger_{l\sigma} h_{l\sigma}) & N : \text{odd}, \\ \sum_\sigma \sum_{l=1}^{N/2} \eta_{le} (g^\dagger_{l\sigma} g_{l\sigma} + h^\dagger_{l\sigma} h_{l\sigma}) + \eta_{0e} g^\dagger_{0\sigma} g_{0\sigma} & N : \text{even}. \end{cases} \end{aligned} \tag{A.4.5}$$

Here, we neglect the constant term because it gives only the energy shift to the system. The eigenvalue for even and odd N can be approximated as $\eta_{le} \sim \Lambda^{(m+1)/2}, \eta_{lo} \sim \Lambda^{l-1}$ for large l. This fact originate at that we define g_l and h_l in the similar forms with a_{l0} in eq. (A.1.49 and b_{l0} in eq. (A.1.50).

Figures A.7 and A.8 show the lowest-lying energy spectrum obtained by the NRG method for even and odd N. For example, in the case of odd N,

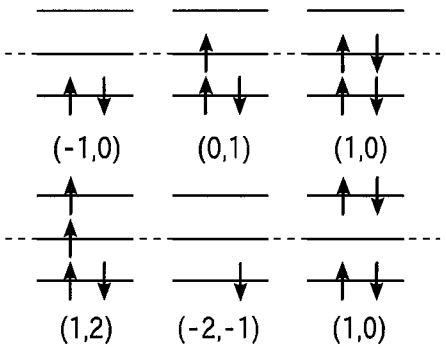

Figure A.8: The example of how the electron occupy the states in the case of even N for each $(Q, 2S_z)$. The lines show the energy spectrum and the dotted line shows the Fermi energy.

number	Q	$2S_z$	Energy/D(N =50)
1	-1	0	0.00000000000
2	1	0	0.00000000000
3,4	0	±1	0.00000070524
5,6	-2	±1	1.52048391659
7,8	-1	±2	1.52048321113
9	-1	0	1.52048391659
10,11	0	±1	1.52048321113
12,13	1	±2	1.52048321113
14	1	0	1.52048391659
15,16	2	±1	1.52048391659
21	-3	0	3.04096712862
22,23	-2	±2	3.04096712862
24,25	-1	±1	3.04096712862
26,27,28	-1	0	3.04096712862

there are only one state for the ground state where electrons are occupied as in the case of $(Q, 2S_z) = (0, 0)$ of Fig. A.7. In this case, the first excited state has quartet degeneracy as seen in the cases of $(1, 1)$ and $(-1, -1)$ which corresponds to the excitation of a electron or a hole. On the other hand, in the case of even N, the ground state has the quartet degeneracy because one of the eigenvalue is the same with the Fermi energy. Therefore, there are 16 states in the first excited states. The higher excited states can be considered in this way, which is consistent with the result obtained by the NRG calculation for the Hamiltonian (A.4.1).

As a final topic in this section, we consider the inverse transformation of eq. (A.4.3) in preparation for the discussion of the effective Hamiltonian around the fixed point mentioned below. In the case of odd N, $f_{0\sigma}$ and $f_{1\sigma}$ are written as

$$f_{0\sigma} = \Lambda^{-(N-1)/4} \sum_{l=1}^{(N+1)/2} \alpha_{0l} \left(g_{l\sigma} + \bar{\sigma} h_{l\sigma}^{\dagger} \right), \tag{A.4.6}$$

$$f_{1\sigma} = \Lambda^{-3(N-1)/4} \sum_{l=1}^{(N+1)/2} \alpha_{1l} \left(g_{l\sigma} - \bar{\sigma} h_{l\sigma}^{\dagger} \right). \tag{A.4.7}$$

For higher $n \geq 2$, $f_{n\sigma}(n \geq 2)$ is composed of a lot of term such as the term being proportional to $\Lambda^{-(N-1)/4}$, term depending on $f_{0\sigma}$, and so on. On the

basis of the numerical calculation, we can calculate α_{0l} and α_{1l}: for example, in the case of $\Lambda = 2.5$, we obtain as follow.

$$\alpha_{01} = 0.699, \quad \alpha_{02} = 0.873, \quad \cdots, \alpha_{0l} = 0.5477(2.5)^{(l-1)/2}. \tag{A.4.8}$$

$$\alpha_{11} = 0.652, \quad \alpha_{02} = 2.718, \quad \cdots, \alpha_{0l} = 0.3059(2.5)^{3(l-1)/2}, \tag{A.4.9}$$

For the general Λ, the analytic formulas are derived as follow.

$$\alpha_{0l} = \sqrt{\frac{1-\Lambda^{-1}}{2}}\Lambda^{(l-1)/2}, \tag{A.4.10}$$

$$\alpha_{1l} = \sqrt{\frac{1-\Lambda^{-3}}{2}}\Lambda^{3(l-1)/2}. \tag{A.4.11}$$

A.4.2 Anderson Model

In this subsection, we show the result of the NRG calculation for the Anderson model and the physical consideration for results. We again show the Anderson model in the transformed form into the one-dimensional chain model, eq. (A.4.1).

$$\mathcal{H}_N = \Lambda^{(N-1)/2}\left[\tilde{\mathcal{H}}_f + \tilde{v}\sum_\sigma (f^\dagger_{-1\sigma}f_{0\sigma} + f^\dagger_{0\sigma}f_{-1\sigma}) + \sum_\sigma\sum_{n=0}^{N-1}\Lambda^{-n/2}\tilde{t}_n(f^\dagger_{n\sigma}f_{n+1\sigma} + f^\dagger_{n+1\sigma}f_{n\sigma})\right], \tag{A.4.12}$$

$$\tilde{\mathcal{H}}_f = \frac{2}{1+\Lambda^{-1}}\bar{\mathcal{H}}_f, \tag{A.4.13}$$

$$\tilde{v} = \frac{2}{1+\Lambda^{-1}}v, \tag{A.4.14}$$

$$\tilde{t}_n = \frac{2}{1+\Lambda^{-1}}\Lambda^{n/2}t_n. \tag{A.4.15}$$

Figures. A.9 and A.10 show the N-dependence of the lowest-lying energy spectrum of the Anderson model calculated by the NRG method. In both even and odd N cases, the lowest-lying energy spectrum changes drastically up to about $N \sim 20$, while those for $N > 20$ are almost independent on N. This converged lowest-lying energy spectrum of odd N corresponds to that of the free electron model of even N, and vice versa. This result means that the impurity site f_{-1} and the most localized conduction site f_0 form

the singlet state as shown in Fig. A.11, and these site does not contribute to the lowest-lying energy spectrum. In other words, the coupling constant between f_{-1} and f_0 sites are antiferromagnetic. For small N, the coupling constant is small N (in a high temperature region). On the other hand, as N increases, i.e., the energy scale of the system decreases, the coupling constant increases and approaches to the strong coupling limit (strong coupling fixed point) where the Kondo-Yosida singlet forms. When the system is near this fixed point, the coupling constant is very large and large amount of the energy is necessary to break the Kondo-Yosida singlet state. Therefore, these two sites do not contribute to the lowest-lying energy spectrum at around this fixed point, and there appears the lowest-lying energy spectrum due to the remaining conduction sites, i.e., that of the free electron model with $N-1$ sites. In such a reason, the lowest-lying energy spectrum is same with that of the free electron model with $N-1$ site. Of course, the conservative quantities and degeneracy is also same.

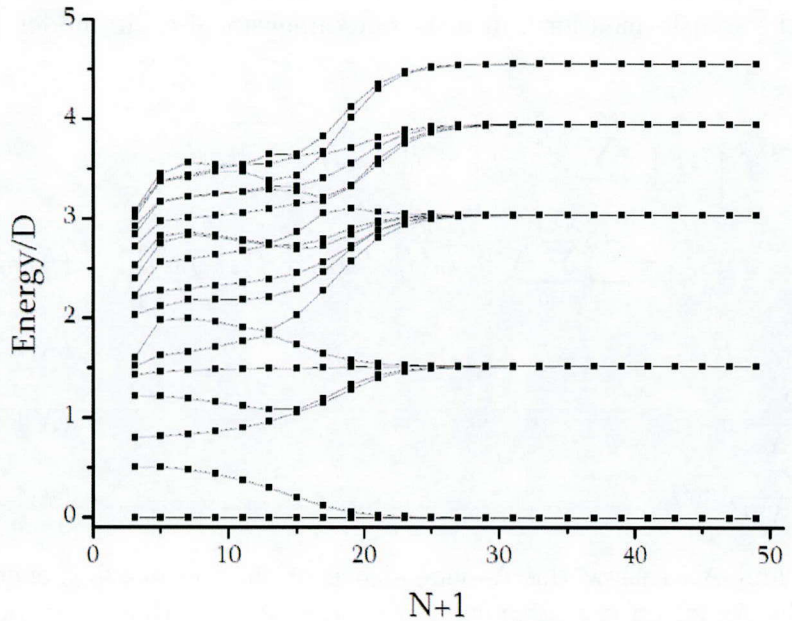

Figure A.9: The change of the lowest-lying energy spectrum of the Anderson model for $\Lambda = 2.5, \bar{\varepsilon}_f = -0.4, \bar{U} = 0.8, \bar{v} = 0.2$ for even N. We keep 1000 states in each truncation process.

A.5 Calculation of Thermodynamic Quantities

The NRG method allows us to calculate various thermodynamic quantities because we obtain the lowest-lying energy spectrum and their conservative quantities. In this section, we introduce the way to calculate the entropy, the susceptibility and the specific heat, and show results for the Anderson model.

In the NRG method, the hopping term t_N decays in the form of $\Lambda^{-(N-1)/2}$ as N increases, and high energy states are discarded by the truncation procedure. Therefore, at each step in the NRG calculation, we obtain the energy spectrum of the order of $\Lambda^{-(N-1)/2}$. From this viewpoint, we define an inverse temperature $\beta_N = (k_{\mathrm{B}} T_N)^{-1}$ as

$$\frac{1+\Lambda^{-1}}{2}\Lambda^{-(N-1)/2}\beta_N \equiv \bar{\beta}, \tag{A.5.1}$$

and we consider the thermodynamic quantities obtained from the energy spectrum at N-th step as that at this temperature. It is noted that $\bar{\beta}$ is the

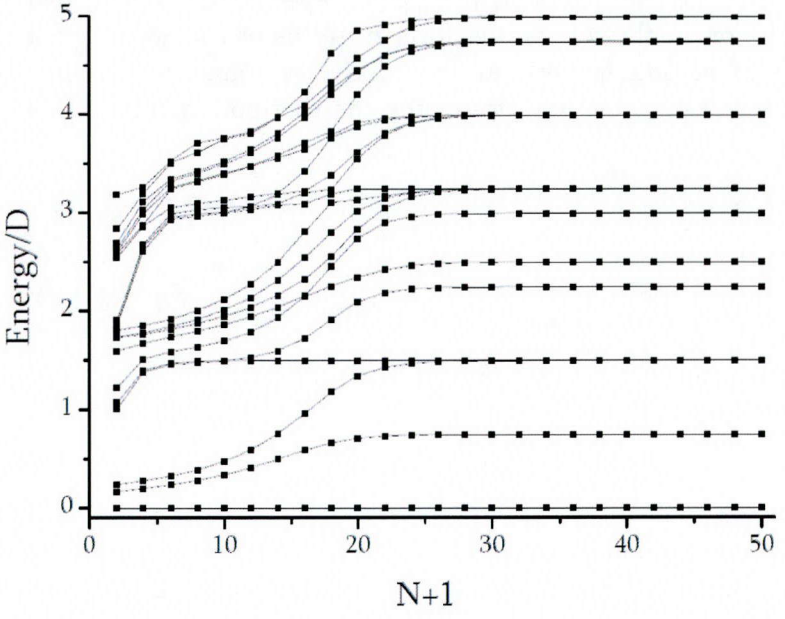

Figure A.10: The change of the lowest-lying energy spectrum of the Anderson model for $\Lambda = 2.5, \bar{\varepsilon}_f = -0.4, \bar{U} = 0.8, \bar{v} = 0.2$ for odd N. We keep 1000 states in each truncation process.

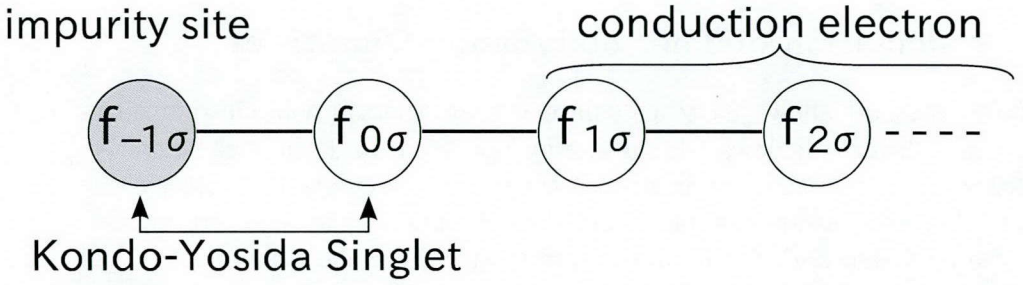

Figure A.11: Diagram in the strong coupling limit. The most localized conduction electron and the impurity site form the Kondo-Yosida singlet state.

quantity of the order of 1, and we often take it as $0.5 \sim 1$, although the adequate $\bar{\beta}$ depends on the discretization parameter Λ and the remaining state in the truncation procedure $N_{\rm tr}$.

The simple form of the entropy contributed from the impurity site, $S_{\rm imp}$ is the first derivative of the free energy, $S_{\rm imp} = -\frac{\partial F_{\rm imp}}{\partial T}$. We should avoid the numerical calculation in the differential form in terms of the accuracy of the numerical calculation, and we evaluate the derivative analytically. For the Hamiltonian in the N-th step, $\mathcal{H}_N$, we define the thermodynamic average as following.

$$\langle \cdots \rangle_N \equiv \frac{1}{Z^{(N)}} \sum_{QS_z} \sum_{r_N} e^{-\beta E_N(Q,2S_z,r_N)} \, {}_N\langle Q, S_z, r_N| \cdots |Q, S_z, r_N\rangle_N, \quad \text{(A.5.2)}$$

$$Z_N = \sum_{Q,S_z} \sum_{r_N} e^{-\beta E_N(Q,2S_z,r_N)}. \quad \text{(A.5.3)}$$

Using the distribution function, eq. (A.5.3), the entropy for $N-th$ step, S_N, is calculated as follows.

$$S_N/k_{\rm B} = \beta \langle \mathcal{H}_N \rangle + \ln Z_N. \quad \text{(A.5.4)}$$

However, the entropy defined by eq. (A.5.4) include the contribution from both impurity site and conduction electrons. In order to see the entropy due to the impurity site, we subtract the contribution from the conduction electrons.

$$S_{N\rm imp}(T_N)/k_{\rm B} = S_N/k_{\rm B} - S_{N\rm cb}/k_{\rm B}, \quad \text{(A.5.5)}$$

$$\mathcal{H}_{N\rm cb} = \sum_{\sigma} \sum_{n=0}^{N} t_n (f^\dagger_{n\sigma} f_{n+1\sigma} + f^\dagger_{n+1\sigma} f_{n\sigma}). \quad \text{(A.5.6)}$$

On the other hand, the standard definition of the magnetic susceptibility is

$$\chi(T) = \int_0^\beta \langle S_z[\tau] S_z \rangle \mathrm{d}\tau - \beta \langle S_z \rangle^2, \tag{A.5.7}$$

where τ is the imaginary time ($0 < \tau < \beta$), S_z the z-component of the impurity spin operator. Here, we focus on the static magnetic susceptibility. In this case, S_z does not depend on time, and S_z is commute with the Hamiltonian, which make the eq. (A.5.7) be simple form as

$$\chi(T_N) = \beta(\langle S_z^2 \rangle - \langle S_z \rangle^2). \tag{A.5.8}$$

We also subtract the contribution due to the conduction electron from eq. (A.5.8) as in the case of the entropy.

In the same manner with the entropy, the specific heat is written as follows.

$$C_{N\mathrm{imp}}(T_N)/k_\mathrm{B} = C_N/k_\mathrm{B} - C_{N\mathrm{cb}}/k_\mathrm{B}, \tag{A.5.9}$$

$$C_N/k_\mathrm{B} = \beta^2 \left(\langle \mathcal{H}_N^2 \rangle - \langle \mathcal{H}_N \rangle^2 \right). \tag{A.5.10}$$

Since we obtain the lowest-lying energy spectrum with good accuracy, we can evaluate the specific heat with good accuracy by using eq. (A.5.10) assuming that the distribution function and the thermodynamic average is calculated properly. However, the amount such as $\langle \mathcal{H}_N \rangle$ and $\langle \mathcal{H}_N^2 \rangle$ do not take account of the information of the higher energy state. The contribution from these high energy state affects the average of the square of the energy compared to the average of the energy, i.e., the numerical error appears in the specific heat easily compared to the entropy. Therefore, the specific heat is obtained by the differentiation of the entropy.

$$C_{N\mathrm{imp}}(T_N) = T \left(\frac{\partial S_{N\mathrm{imp}}}{\partial T} \right). \tag{A.5.11}$$

As noted above, in the NRG method, the energy spectrum obtained in even N step is different from that obtained in odd N step, which gives the wavy lines for the temperature dependence of the physical quantities. This in turn means that we should calculate the thermodynamic quantities for either even or odd N only, and lose half of the temperature values. However, we can use all information by averaging the thermodynamic quantities obtained at odd and even steps.

$$O(T_N) \simeq \frac{1}{2} \left(O(N) + O(N-1) + \frac{O(N+1) - O(N-1)}{T_{N+1} - T_{N-1}} (T_N - T_{N-1}) \right), \tag{A.5.12}$$

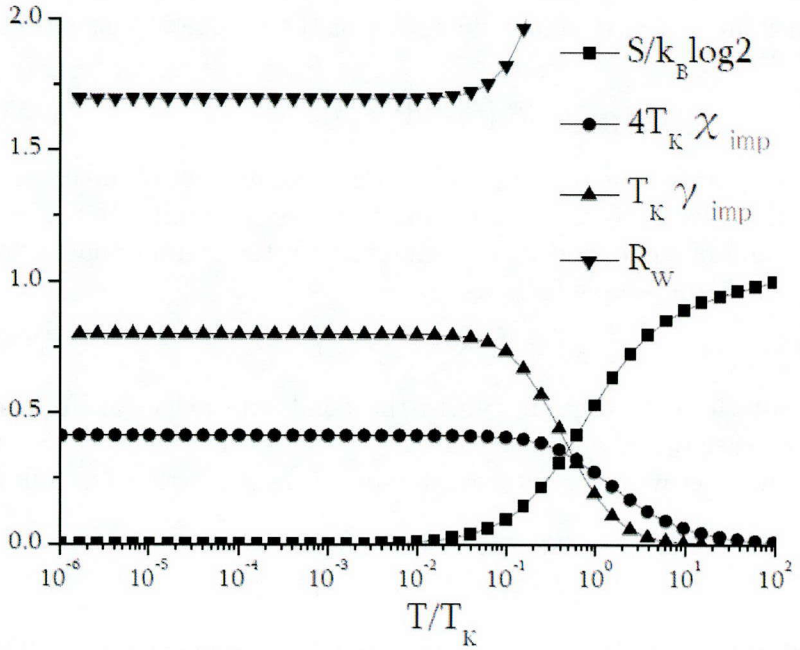

Figure A.12: The temperature dependence of various thermodynamic quantities due to the impurity site in the unit of the Kondo temperature $T_{\rm K}$ in the Anderson model for $\Lambda = 2.5, \bar{\varepsilon}_f = -0.4, \bar{U} = 0.8, \bar{v} = 0.2$. We keep up to 1000 state in each truncation procedure.

where $O(T_N)$ means the any thermodynamic quantities for a given N. With this averaging procedure, we obtain smooth line and use the all information obtained in the NRG method.

Moreover, with use of these physical quantities mentioned above, we can also calculate the Sommerfeld coefficient $\gamma_{\rm imp}(T) = C_{\rm imp}/T$, Wilson ratio $R_{\rm W} = 4\pi^2\chi_{\rm imp}(T)/[3\gamma_{\rm imp}(T)]$, and the Kondo temperature $T_{\rm K}$ by the definition of the Wilson, $4T_{\rm K}\chi_{\rm imp}(0) = 0.413$.

Fig. A.12 shows the temperature dependence of the entropy $S_{\rm imp}(T)$, the magnetic susceptibility $\chi_{\rm imp}(T)$, the Sommerfeld coefficient $\gamma_{\rm imp}(T) = C_{\rm imp}/T$ and the Wilson ratio $R_{\rm W} = 4\pi^2\chi_{\rm imp}(T)/[3\gamma_{\rm imp}(T)]$ in a unit of the Kondo temperature $T_{\rm K}$ by the NRG method. Here, we take $g\mu_{\rm B}$=1, and Kondo temperature is determined by the definition of the Wilson. In the region $T > T_{\rm K}$ (corresponding to smaller N-th steps), the impurity site is occupied with one electron with up or down spin, which is behaves as the localized moment.

Hence, the entropy is equal to $\sim k_{\rm B}\log 2$ which represent the spin 1/2 degree of freedom, and the magnetic susceptibility obeys the Curie-Weiss law,

$$\chi = \frac{Ng^2\mu_B^2 S(S+1)}{3k_{\rm B}T}. \tag{A.5.13}$$

On the other hand, as the temperature decreases (as N increases) the Kondo-Yosida singlet state start to form and the energy spectrum changes drastically at $T \sim T_{\rm K}$. As the temperature decreases more i.e., in the region $T \ll T_{\rm K}$ (strong coupling limit), the entropy and the magnetic susceptibility cross over to zero, and $R_{\rm W}$ approaches 2. This result indicates that the system can be described on the basis of the local Fermi liquid. It is noted that $\gamma_{\rm imp}(T)$ start to increase at around $T_{\rm K}$ as T decreases, which indicates that the effective mass of the electron increases because of the relation $\gamma \propto m^*$.

A.6 Analysis around Strong Coupling Fixed Point

Now, we consider the situation that the system goes to a fixed point $\mathcal{H}^*$. Since we obtain the different energy spectrum at even and odd steps in the NRG calculation, the system H_N obeys the following relation at the fixed point,

$$\mathcal{H}_{N+2} = \mathcal{L}\mathcal{H}_N = \mathcal{H}^* \tag{A.6.1}$$

where $\mathcal{L}$ is the renormalization group transformation. In the Anderson model with $V \neq 0$, the system surely approaches to the strong coupling limit in the limit of large N, i.e.,

$$\mathcal{H}^* = \lim_{N\to\infty} \mathcal{H}_N. \tag{A.6.2}$$

However, there certainly remains the deviation from the strong coupling limit $\mathcal{H}^*$ in the NRG calculation even if we take large enough N. We define this deviation from $\mathcal{H}^*$ in the N-th step in the NRG calculation as $\delta\mathcal{H}_N$.

$$\delta\mathcal{H}_N = \mathcal{H}_N - \mathcal{H}^*, \tag{A.6.3}$$

$$\delta\mathcal{H}_N = \sum_m \omega_m \Lambda^{(N-1)/2}\hat{O}_m, \tag{A.6.4}$$

where $\hat{O}_m$ are the eigenoperators determined by the kind of the fixed point, and ω_m the coefficients. We previously subtract the factor $\Lambda^{(N-1)/2}$ which is the contributions from the $\mathcal{L}$ giving the multiplication by $\sqrt{\Lambda}$ in each step.

For $\mathcal{L}$, $\delta\mathcal{H}_N$ is transformed as

$$\begin{aligned}\delta\mathcal{H}_{N+2} &\equiv \mathcal{H}_{N+2} - \mathcal{H}^* = \mathcal{L}\left[\mathcal{H}_* + \delta\mathcal{H}_N\right] - \mathcal{H}^* \\ &= \mathcal{L}\delta\mathcal{H}_N = \mathcal{L}\sum_m \omega_m \Lambda^{(N-1)/2}\hat{O}_m = \sum_m \omega_m \Lambda^{(N-1)/2}\left(\mathcal{L}\hat{O}_m\right) \\ &= \sum_m \omega_m \Lambda^{(N-1)/2}\left(\Lambda\lambda_m\hat{O}_m\right), \end{aligned} \tag{A.6.5}$$

where λ_m is the eigenvalue of $\hat{O}_m$.

For the increase of N, the amount of the contribution from each $\hat{O}_m$ is classified into the following three cases according to the eigenvalue of $\mathcal{L}$, $\Lambda\lambda_m$.

[1] $\Lambda\lambda_m > 1$: relevant operator

[2] $\Lambda\lambda_m = 1$: marginal operator

[3] $\Lambda\lambda_m < 1$: irrelevant operator

If $\delta\mathcal{H}_N$ include one relevant operator for the fixed point, that fixed point is unstable because the deviation from $\mathcal{H}^*$ increases by the renormalization procedure. On the other hand, if $\delta\mathcal{H}_N$ include only irrelevant operator for the fixed point, that fixed point is stable because the deviation from $\mathcal{H}^*$ decreases by renormalization procedure once the system approaches to that fixed point. As for the marginal operator, it is necessary to analyze those operators for each fixed point. It is noted that eigenoperators $\hat{O}_m$ should have the same symmetry with each fixed point in order not to break the symmetry of each fixed point.

With consideration above circumstance, we determine the effective Hamiltonian of the Anderson model at the strong coupling fixed point. The conservative quantities require the operator which conserve the total charge Q and z-component of the total spin S_z. The terms composed of $f_{0\sigma}$ and $f_{1\sigma}$ decay in the form less than $\Lambda^{-N/4}$ as seen in eqs. (A.4.6) and (A.4.7), while we neglect the term composed of $f_{n\sigma}$ with $n \geq 2$ because $f_{n\sigma}$ decays in the form less than $\sim \Lambda^{-7N/4}$ which decreases drastically for $N \gg 1$. Thus, we assume that $\hat{O}_m$ is composed of f_{-1}, f_0, and obtain the following candidates for $\hat{O}_m$.

$$\hat{O}_1 = f^\dagger_{0\sigma} f_{1\sigma} + f^\dagger_{1\sigma} f_{0\sigma}, \tag{A.6.6}$$

$$\hat{O}_2 = (f^\dagger_{0\sigma} f_{0\sigma} - 1)^2, \tag{A.6.7}$$

$$\hat{O}_3 = (f^\dagger_{0\sigma}\vec{\sigma}_{\sigma\sigma'} f_{0\sigma})(f^\dagger_{-1\mu}\vec{\sigma}_{\mu\mu'} f_{-1\mu}), \tag{A.6.8}$$

$$\hat{O}_4 = (f^\dagger_{-1\mu} f_{-1\mu} - 1)(f^\dagger_{0\sigma} f_{0\sigma} - 1), \tag{A.6.9}$$

where subscripts of spin σ and μ implicitly indicate that we take the summation of spins. The eigenvalue for $\mathcal{L}$ of $\hat{O}_m$ are Λ^{-1} for $\hat{O}_1$ and $\hat{O}_2$, and 1 for $\hat{O}_3$ and $\hat{O}_4$ Since the fluctuation of the f-electron is suppressed at around the strong coupling limit, $\hat{O}_3$ is approximated as $O_3 \propto (f^\dagger_{0\sigma}\vec{\sigma}_{\sigma\sigma'}f_{0\sigma'})$ which breaks the particle-hole symmetry, and it can be negligible. Although $\hat{O}_4$ is the marginal operator, it can be negligible because the localized spin is "frozen" by the conduction electron by forming the Kondo-Yosida singlet state at around the strong coupling limit, and $\hat{O}_4$ gives the constant term which is subtracted by $\mathcal{L}$. Thus, the effective Hamiltonian is composed of $\hat{O}_1$ and $\hat{O}_2$.

$$\mathcal{H}_N = \Lambda^{(N-1)/2}\left(\omega_1\hat{O}_1 + \omega_2\hat{O}_2\right). \tag{A.6.10}$$

In order to verify the validity of the effective Hamiltonian, eq. (A.6.10), we rewrite $\hat{O}_1$ and $\hat{O}_2$ with g and h. Here, we only discuss the case of even N because the discussion for odd N is almost the same. By using eqs. (A.4.6) and (A.4.7), these two operators are written as

$$\begin{aligned}\hat{O}_1 &= f^\dagger_{0\sigma}f_{1\sigma} + f^\dagger_{1\sigma}f_{0\sigma} \\ &= \Lambda^{-(N-1)}\sum_{i=1}^{(N+1)/2}\sum_{j=1}^{(N+1)/2}\Big[(\alpha_{0i}\alpha_{1j} + \alpha_{1i}\alpha_{0j})\left(g^\dagger_{i\sigma}g_{j\sigma} + h^\dagger_{i\bar{\sigma}}h_{j\bar{\sigma}}\right) \\ &\qquad + \bar{\sigma}\,(\alpha_{0i}\alpha_{1j} - \alpha_{1i}\alpha_{0j})\left(g_{i\sigma}h_{j\bar{\sigma}} - g^\dagger_{i\sigma}h^\dagger_{j\bar{\sigma}}\right)\Big] + \text{const.}\end{aligned} \tag{A.6.11}$$

$$\begin{aligned}\hat{O}_2 &= \left(f^\dagger_{0\sigma}f_{0\sigma} - 1\right)^2 \\ &= \Lambda^{-(N-1)}\sum_{ijkl}\alpha_{0i}\alpha_{0j}\alpha_{0k}\alpha_{0l}\Big[-g^\dagger_{i\sigma}g^\dagger_{k\mu}g_{j\sigma}g_{l\mu} - h^\dagger_{i\sigma}h^\dagger_{k\mu}h_{j\sigma}h_{l\mu} \\ &\quad - \bar{\sigma}\bar{\mu}\left(g^\dagger_{i\sigma}g^\dagger_{k\mu}h^\dagger_{j\bar{\sigma}}h^\dagger_{l\bar{\mu}} + g_{i\sigma}g_{k\mu}h_{j\bar{\sigma}}h_{l\bar{\mu}}\right) + 2g^\dagger_{i\sigma}h^\dagger_{k\bar{\mu}}g_{j\sigma}h_{l\bar{\mu}} - 2\bar{\sigma}\bar{\mu}g^\dagger_{i\sigma}h^\dagger_{j\bar{\sigma}}g_{k\mu}h_{l\bar{\mu}} \\ &\quad + 2\bar{\sigma}g^\dagger_{i\mu}g_{k\sigma}g_{j\mu}h_{l\bar{\sigma}} - 2\bar{\mu}h^\dagger_{i\bar{\sigma}}g_{k\mu}h_{j\sigma}h_{l\bar{\mu}} + 2\bar{\mu}\bar{\mu}g^\dagger_{i\sigma}g^\dagger_{k\mu}h^\dagger_{l\mu}g_{j\bar{\sigma}} - 2\bar{\sigma}g^\dagger_{i\sigma}h_{j\bar{\sigma}}h^\dagger_{k\bar{\mu}}h_{l\bar{\mu}}\Big].\end{aligned} \tag{A.6.12}$$

Here, in the calculation of $\hat{O}_1$, we use the relation $\Lambda^{-(N-1)/2}\sum_i \alpha^2_{0i} = 1$, which is derived from the result that the transformation from f to g, h is the Unitary transformation. The constant term appeared in eq. (A.6.11) can be negligible because the renormalization group transformation $\mathcal{L}$ subtract the constant term.

i	state	Q	2 S	E($\mathcal{H}^*$)	$\langle i\|\delta\mathcal{H}^*\|i\rangle$
1	$g^\dagger_{1\sigma}\|0\rangle$	1	1	ε_1	$2\alpha_{01}\alpha_{11}\tilde{\omega}_1$
2	$g^\dagger_{2\sigma}\|0\rangle$	1	1	ε_2	$2\alpha_{02}\alpha_{12}\tilde{\omega}_1$
3	$g^\dagger_{1\uparrow}g^\dagger_{1\downarrow}h^\dagger_{1\sigma}\|0\rangle$	1	1	$3\varepsilon_1$	$6\alpha_{02}\alpha_{12}\tilde{\omega}_1$
4	$g^\dagger_{1\uparrow}g^\dagger_{1\downarrow}\|0\rangle$	2	0	$2\varepsilon_2$	$4\alpha_{02}\alpha_{12}\tilde{\omega}_1 + 2\alpha^4_{01}\tilde{\omega}_2$
5	$g^\dagger_{1\sigma}g^\dagger_{2\bar{\sigma}}\|0\rangle$	2	0	$\varepsilon_1+\varepsilon_2$	$2\left(\alpha_{01}\alpha_{11}+\alpha_{02}\alpha_{12}\right)\tilde{\omega}_1 + 4\alpha^2_{01}\alpha^2_{02}\tilde{\omega}_2$
6	$g^\dagger_{1\sigma}g^\dagger_{2\sigma}\|0\rangle$	2	2	$\varepsilon_1+\varepsilon_2$	$2\left(\alpha_{01}\alpha_{11}+\alpha_{02}\alpha_{12}\right)\tilde{\omega}_1$
7	$g^\dagger_{1\sigma}h^\dagger_{1\bar{\sigma}}\|0\rangle$	0	0	$2\varepsilon_1$	$4\alpha_{01}\alpha_{11}\tilde{\omega}_1 + 2\alpha^4_{01}\tilde{\omega}_2$
8	$g^\dagger_{1\sigma}h^\dagger_{1\sigma}\|0\rangle$	0	2	$2\varepsilon_1$	$4\alpha_{01}\alpha_{11}\tilde{\omega}_1 - 2\alpha^4_{01}\tilde{\omega}_2$
9	$g^\dagger_{1\uparrow}g^\dagger_{1\downarrow}h^\dagger_{1\uparrow}h^\dagger_{1\downarrow}\|0\rangle$	0	0	$4\varepsilon_1$	$8\alpha_{01}\alpha_{11}\tilde{\omega}_1$
10	$g^\dagger_{1\sigma}h^\dagger_{2\bar{\sigma}}\|0\rangle$	0	0	$\varepsilon_1+\varepsilon_2$	$2\left(\alpha_{01}\alpha_{11}+\alpha_{02}\alpha_{12}\right)\tilde{\omega}_1$

Table A.2: The corrections of energy by $\delta\mathcal{H}_N$ for each state. σ is spin, ε_i is the eigenvalues at the strong coupling fixed point, and $\tilde{\omega}_i \equiv \Lambda^{-(N-1)/2}\omega_i$.

Using eqs. (A.6.11) and (A.6.12), $\delta\mathcal{H}_N$ is represented as

$$\delta\mathcal{H}_N = \mathcal{H}_N - \mathcal{H}^* = \Lambda^{-(N-1)/2}\sum_{m=1}^{2}\omega_m\Lambda^{(N-1)}O_m. \tag{A.6.13}$$

On the supposition that eq. (A.6.13) is the perturbation term for $\mathcal{H}^*$, and we neglect contributions from the second order perturbations of $\hat{O}_1$ and $\hat{O}_2$ because the second order perturbation (of the order of $\sim \Lambda^{-(N-1)}$) is well smaller than the first order perturbation (of the order of $\sim \Lambda^{-(N-1)/2}$) in the strong coupling limit. The eigenvalue of $\mathcal{H}_N$ of a state indicated by a quantum number i, E_{Ni}, is composed of only two terms: the energy at the strong coupling fixed point and the correction by the first order perturbation of $\delta\mathcal{H}_N$.

$$E_{Ni} = E^*_i + \langle i|\delta\mathcal{H}_N|i\rangle, \tag{A.6.14}$$

Table. A.2 shows corrections of energy by $\delta\mathcal{H}_N$ for each state at around the strong couling fixed point. Two coefficients, ω_1 and ω_2 are determined by using two energies obtained by the numerical calculation. ω_1 and ω_2 thus obtained allow us to calculate the energy of the other states, and we discuss the validity of the effective Hamiltonian by comparing the calculated energies and that obtained in the NRG calculation. Here, we use the eigenvalue of the energy for large enough N obtained by the NRG calculation as substitution for energy spectrum at the strong coupling fixed point.

i	Q	2 S	E($\mathcal{H}^*$)	$E(\mathcal{H}^*) - E(\mathcal{H}_N)$	$\langle i\|\delta\mathcal{H}^*\|i\rangle$	error(%)
1	1	1	0.7468558561068	3.04521E-6	input	–
2	1	1	2.4932063321570	1.58616E-5	1.58616E-5	99.998
3	1	1	2.2405584325482	9.13577E-6	9.13563E-6	100.001
4	2	0	1.4937107577209	9.54493E-7	input	–
5	2	0	3.2400593087319	2.87953E-6	2.87962E-6	99.997
6	2	2	3.2400432813117	1.89070E-5	1.89070E-5	99.999
7	0	0	1.4937107577210	9.54493E-7	9.54493E-7	100.000
8	0	2	1.4937004858712	1.12263E-5	1.12263E-5	100.000
9	0	0	2.9874112430055	1.21814E-5	1.21808E-5	100.005
10	0	0	3.2400432813116	1.89070E-5	1.89070E-5	99.999
$\tilde{\omega}_1 = 3.34332E-6 \times \Lambda^{-(N-1)/2}$						
$\tilde{\omega}_2 = -1.07738E-5 \times \Lambda^{-(N-1)/2}$						

Table A.3: The validity of the effective Hamiltonian, eq. (A.6.13) at $N = 50$ of the Anderson model for $\Lambda = 2.5, \bar{\varepsilon}_f = -0.4, \bar{U} = 0.4, \bar{v} = 0.8$. We keep states up to 1000 state in the truncation process, and the value at $N = 100$ as substitutes of $\mathcal{H}^*$.

Table A.3 shows the result of the comparison between energies obtained in the NRG calculation and that calculated by the effective Hamiltonian. Here, we obtain $\tilde{\omega}_1 \equiv \Lambda^{-(N-1)/2}\omega_1$ and $\tilde{\omega}_2 \equiv \Lambda^{-(N-1)/2}\omega_2$ from states indicated as i="1" and "4". The eigenvalue of the effective Hamiltonian are in an excellent agreement with that obtain in the NRG calculation, which indicates that the effective Hamiltonian describes the deviation from the strong coupling fixed point well.

Acknowledgements

I would like to express my hearty gratitude to Professor. K. Miyake for teaching me many interesting phenomena of heavy fermion systems, which leads my attention to these materials, and giving me a lot of fruitful proposals. With these patient guidance of his for over six years, I managed to accomplish my studies.

I would also like to appreciate a lot of helpful advice and discussions with Drs. H. Kohno, A. Tsurura, S. Watanabe. I acknowledge gratefully Drs. Y. Yoshioka and Y. Fuseya who gave me a lot of advice, not only for the scientific difficulties but also for my personal problems. I should express my acknowledgement to Ms. E. Hazama and I. Uchida for administrative assistance, my personal problems such as a job-hunting and so on.

I am indebted very much to Drs. H. Matsuura, S. Yotsuhashi, H. Kusunose and K. Hattori for their essential advice on the Wilson numerical renormalization group method which is absolutely necessary to my researches in Miyake Laboratory. I am also grateful to the members of Miyake Laboratory for their interesting discussions and powerful encouragements.

I would like to express my gratitude to Professor Chandra. M. Varma for discussing and supporting my new research and his kind hospitality when I stayed in University of California, Riverside.

I also gratefully appreciate the financial support of Global-COE program (G10) from the Japan Society for the Promotion of Science, which made it possible to complete my thesis.

Finally, I would like to express great acknowledgement to my parents and my friends for their encouragements and supports for years.

Research Achievements

Paper

[1] "Effect of Magnetic Impurity Scattering on Superconducting Transition in Low Dimensions: Effect of Long-Time-Tail Of Magnetization Diffusion"
S. Nishiyama and K. Miyake: J. Phys. Soc. Jpn. **78** (2009) 074709-1-6.

[2] "Magnetically Robust Non-Fermi Liquid Behavior in Heavy Fermion Systems with f^2-Configuration: Competition between Crystalline-Electric-Field and Kondo-Yosida Singlets"
S. Nishiyama, H. Matsuura and K. Miyake: J. Phys. Soc. Jpn. **79** (2010) 104711-1-7.

[3] "Magnetically Robust Non-Fermi Liquid Behavior due to the Competition between Crystalline-Electric-Field Singlet and Kondo-Yosida Singlet in f^2-Based Heavy Fermion Systems"
S. Nishiyama, H. Matsuura and K. Miyake: J. Phys.: Conf. Ser. **273** (2011) 012047-1-4.

[4] "Magnetic Field Effect on Crossover Temperature from Non-Fermi Liquid to Fermi Liquid Behavior in f^2-Impurity Systems with Crystalline-Electric-Field Singlet State Competing with Kondo-Yosida Singlet Stat"
S. Nishiyama and K. Miyake: J. Phys. Soc. Jpn. **80** (2011) 124706-1-8; Addendum, S. Nishiyama and K. Miyake: J. Phys. Soc. Jpn. **81** (2012) 037001-1.

[5] "Effect of Competition between Inter-Site and Kondo-Yosida Singlet States on Charge Transfer Susceptibility in Heavy Fermion System"

S. Nishiyama and K. Miyake: J. Phys. Soc. Jpn., submitted.

Conference Presentation

[1] "Effect of Long-Time-tail due to Magnetic Impurity Scattering on Superconducting Transition Temperature in Low Dimensions"
S. Nishiyama and K. Miyake: The Physical Society of Japan, Spring Meeting, Rikkyo University, 2009/3/28 (Poster)

[2] "Magnetically Robust Non-Fermi Liquid Behaviors due to Competition between Kondo-Yosida Singlet and Crystalline-Electric-Field Singlet states in f^2-Configuration Systems"
S. Nishiyama, H. Matsuura and K. Miyake: The Physical Society of Japan, Autumn Meeting, Osaka Prefecture University, 2010/3/23 (Oral)

[3] "Competition between Crystalline-Electric Field Effect and Kondo Effect in f^2-based Heavy Electron systems: Magnetic Field Effect on Local Non-Fermi Liquid-like Behavior"
S. Nishiyama, H. Matsuura and K. Miyake: International Conference on Core Research and Engineering Science of Advanced Materials, Osaka University, 2010/6/2 (Poster)

[4] "Magnetically Robust Non-Fermi Liquid Behavior due to the Competition between Crystalline-Electric Field-Singlet and Kondo-Yosida Singlet in f^2-Based Heavy Fermion Systems"
S. Nishiyama, H. Matsuura and K. Miyake: International Conference on Strongly Correlated Electron Systems 2010, Santa Fe, USA, 2010/7/1 (Poster)

[5] "Effect of Magnetic Field on the Competition between Kondo-Yosida Singlet and f^2-Crystalline-Electric-Field Singlet States: Temperature dependence of Resistivity"
S. Nishiyama and K. Miyake: The Physical Society of Japan, Spring Meeting, Niigata University, 2011/3/27 (Poster)

[6] "Scaling Property of Non-Fermi Liquid Behavior in $Th_{1-x}U_xRu_2Si_2$: Analysis on Numerical Renormalization Group"
S. Nishiyama and K. Miyake: International Conference on Strongly Correlated Electron Systems 2011, Cambridge, UK, 2011/8/31 (Poster)

[7] "Anomaly in Charge Transfer Susceptibility between f- and Conduction Electron in Two Impurity Anderson Model"
S. Nishiyama and K. Miyake: The Physical Society of Japan, Autumn Meeting, Yokohama National University, 2012/9/20 (Oral)